# Two-Dimensional Momentum Space Density of Electrons in Layer-Like Electronic Systems

## 金属中の電子の2次元運動量空間密度と電子放出量の比較

Ryoji Kato

Min Min Aye Kyi

アウン ミンミン キン

# Three Dimensional Momentum Space Density of Electrons in Metals and Their Electronic Structure

# 金属中の電子の３次元運動量空間密度と電子的性質の関連

1999 March

1999年3月

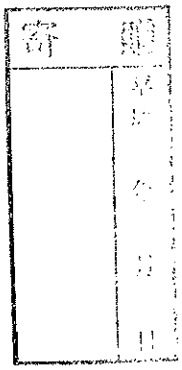

Alaa Salah Abdul Hamid

アブドル ハミドアラ-サラ-

# Acknowledgment

*I have no adequate way of expressing my sincere gratitude, heartfelt thanks and appreciation to the academic advisor of this study; Prof. Dr. Shoichiro Tanigawa of Institute of material science; University of Tsukuba, who was of great help and persistent encouragement through my Doctoral program.*

*Many thanks and appreciation are due to Prof. M. Matsumoto for his help during the Hf work, and also special thanks to Dr. A. Uedono for his help during my study in the Laboratory.*

*I would like also to extend my thanks and appreciation to the Japanese language teaching staff of the University of Tsukuba for their sincere help when undertaking Japanese language course.*

*The financial support provided by Ministry of Education, Cultural and Science (MONBUSHO) of Japan is greatly acknowledged. It was a great opportunity not only for academic perspective, but also to learn and get to know about the specific great culture and people of this nice country.*

*I feel in dept to my parents for not giving them enough time when they were in need. I thank them from my deep heart and hope to compensate them for that in future*

*Finally, thanks to my God, and I hope that work to be written in my good deeds.*

# List of symbols

**2D-ACAR** two dimensional angular correlation of positron annihilation radiation.

**ρ(P)** electron density in the momentum space.

**HMC's** High Momentum Components.

$|\nabla n(k)|$ differentiation of the electron density in the wave vector space.

$n(k)$ electron density in the wave vector space.

$n(k)\%$ normalized electron density in the wave vector space.

$P_F$ Fermi momentum.

$B(r)$ auto correlation function of the wave function in the real space.

$k_B = 0.63372 \cdot 10^{-5}$ Ryd /K the Boltzmann constant.

$G_{III}$ nearest neighbor reciprocal lattice points.

# List of Figures

# Table of contents

## CHAPTER IV

## Results and Discussions

# Abstract

Our goal in the present work is to study the momentum space density and Fermi surface on certain materials of interest using 2D-ACAR experiment. These materials are the divalent HCP structure metals Mg, Zn and Cd, the HCP structure metals of group IIIA Sc and Y, the HCP structure metals of group IVA Ti, Zr and Hf, FCC structure metals of group VIII Rh and Ir, the non-cuprate layered proveskite superconductor $Sr_2RuO_4$, and the layered dichalcogenides of group VB $NbSe_2$. The measurements have been carried out using two experimental set-ups. In the first, a pair of 128 detectors has been used to construct the data covering 20 mrad × 20 mrad. In the second, a pair of 256 detectors has been used to construct the data covering 30 mrad × 30 mrad. From the measured 2D-ACAR spectra the three dimensional electron density in the momentum space $\rho(P)$ has been reconstructed using the reconstruction technique based on Fourier transform. Some observations have been noticed from the reconstructed spectra. Firstly, the divalent HCP structure metals show distortions in upper part of their spectra. Those distortions have been observed and discussed in terms of Kahana-like enhancement and many body effects. Secondly, the metals of groups IIIA and IVA show Breaks in their spectra. Those breaks have been studied and interpreted in terms of the electronic configurations of the examined metals. Thirdly, the high momentum components (HMC's) have been observed in the spectra of the used elements. They are attributed to the Umklapp process. Fourthly, the effect of the strong signal d-like in the Fermi surface features in the elements of groups IIIA, IVA and VIII has been observed and discussed. Finally, in Ir spectra broadening has been observed and discussed in terms of its high absorption of $\gamma$-rays.

The electron density in the wave vector space $n(k)$ has been constructed, restricted within first Brillouin zone, using Locks, Crisp and West (LCW) folding procedure. Then, Fermi surfaces of the metals under investigations have been constructed. Moreover, the least square fitting method has been applied in the experimental results with respect to the theoretical ones to estimate the band's occupation. The results of Fermi surface for each group of materials will discuss below.

Fermi surfaces of divalent HCP structure metals have been compared with the

free electron model and with that obtained from band structure calculation using linear muffin tin orbital (LMTO) and augmented plane wave method (APW) methods. They show agreement with that obtained from the free electron model. The absence of some sheets from the Fermi surface of Mg, Zn and Cd has been interpreted in terms of the experimental resolution.

Fermi surfaces of the metals of group IIIA have been compared with the free electron model and with the band structure calculation using cellular and APW methods. And the Fermi surfaces of the metals of group IVA have been compared with the free electron model, and the band structures calculation using APW and linear combination of atomic orbital (LCAO) methods. The Fermi surfaces of Sc, Y, Ti and Zr show agreement with that obtained from APW method, while the Fermi surface of Hf shows agreement with that obtained from relativistic RAPW method.

Fermi surfaces of Rh and Ir have been compared with the RAPW and LCAO methods. These Fermi surfaces show good agreement with the band structure calculation using RAPW method.

Fermi surface of $Sr_2RuO_4$ has been obtained and compared with that calculated using the local-density approximation (LDA) method. The present results show good agreement with the band structure calculation.

Fermi surface of $NbSe_2$ has been compared with the band structure calculation using APW method. The difference of the dimension of the hole surface around Γ-A axis in the Fermi surface of $NbSe_2$ has been explained in terms of the non uniformity of the positron wave function. The deviations of the Fermi surface dimensions from that obtained by the band structure calculation have been explained in terms of the present experimental resolution.

As regards, while the divalent HCP structure metals show good agreement with the free electron model, deviation from it obtains for the other elements.

# CHAPTER I

# General Introduction

## I.1 Historical Introduction

During the past few years, a rapid progress has been made in the experimental methods, which are available for obtaining information about the momentum space density and Fermi surface of metals and compounds. Amongst the spectroscopies of the electronic structure of solids, positron annihilation has proven to be a useful probe in establishing this information, where resolution in k-space is essential [1.1.1]. As early as 1942, it was realized that a measurement of the deviation from the collinear angle between the emitted two photons, in the annihilation of a positron-electron pair, could provide information about the momentum distribution of electrons in the solids [1.1.2]. In 1958, Berko and Plaskett [1.1.3] have applied these measurements successfully to account for the shapes of the angular correlation curve in metals. Consequently, following this work Berko et al (1977) [1.1.4], Manual et al (1979) [1.1.5] and West et al (1981) [1.1.6] have designed an apparatus for the measurement of angular correlation of annihilation radiation in two dimensions (2D-ACAR). It became well known that the angular correlation of annihilation photon pairs is corresponded to a 2D projection of the momentum space density of the electrons sampled by the injection of positrons. Thus, contained information about both the occupied regions of k-space, i.e. the Fermi surface and the electronic wave functions. The boundless increased resolution in momentum space resulting from the measurements of the two transverse resolutions in momentum components opened up an entirely new overabundance of problems, which could be addressed by positron technique. Nowadays, there are many 2D-ACAR machines have been built and a consequent deluge of richly structure spectra has prompted further refinements in the 2D-ACAR measurement technique, in the processing and imaging of the data, and in its analysis. However, concurrent with these experimental developments together with the instrumental sophistication, the complexity of the systems investigated has grown from pure metals, semiconductors, to half metallic ferromagnetic, and high TC superconductors, etc. Amongst those, transition metals have shown explicitly interest. Since the electronic properties of these metals are dominated by their d-electrons. These d-

electrons are tightly bounded compared to the s-p states of similar energy and from band with strong atomic character to their wave functions. Those metals have been recognized, to be best described, with the tight-binding approximation for the d-bands, as a starting point, in contrast to the free-electron approximation for, say, the alkali metals. However, one objection has been that the d-states are not true bound states, but only resonance which decay into plane wave outside the atom in question (see section I.2). The appropriateness of the tight binding for d-electrons has continually been emphasized by Friedel [1.1.7], who with his collaborators have shown that many of the properties of transition metals follow naturally from this point of view. However, In contrast with the simple metals, there have been relatively small amount of 2D-ACAR experimental work performed on the momentum space density and Fermi surface of transition metals because of the difficulties in obtaining sufficient pure samples.

## I.2 Critique of the band structure calculation methods

There have been a large number of band structure calculation methods performed in the last three decades, and these have had an important effect on our understanding of the electronic structure, of crystals. Some of these methods can be expected to give meaningful results in a wide variety of applications, but there is no method can describe as the best method to use for all crystals. It is important to know the applications for which these methods are most studies, and in this respect there are certain general guidelines that can be established. The descriptions of the commonly used methods in the energy band calculations can be found in several texts see e.g. Jones [1.2.1], Ziman [1.2.2], Callaway [1.2.3], Slater [1,2,4], Harrison [1,2,5], Loucks [1.2.6], and Papaconstantopoulos [1.2.7]. These include the tight binding method, cellular method, orthogonalized plane wave method (OPW), Pseudo-potential method, Green function method, Augmented plane wave method (APW), linear combination of atomic orbital method (LCAO). The most practical applications of the tight binding method have been for core states and the more localized itinerant electrons such as those identified with d-band in transition elements. The pseudo-potential method in a common use is based on the OPW method. Pseudo-potential method has been most practical for calculating nearly free electron NFE energy bands. These include the alkali metals, the alkali-earth metals Al, C, Si and most of the metals, Semi-metals and semi-conductors with complete filled d-shell. However, the applications of the pseudo-potential method based on OPW method have been limited primarily to NEF crystal. That is because this method required the electrons in the crystal to be separated into two categories, core electrons and itinerant electrons. In the most particular form of the method all the atomic functions which don't overlap on neighboring lattice sites are included in the core. The OPW basis function is constructed by orthogonalized plane wave to these core states. For crystal containing no d-electrons, it is easy to separate the core and itinerant electrons. The inner atomic states are well separated in energy from the outer ones and there is very little overlap between these functions on the neighbor lattice sites. In crystals containing transition elements the electrons are not as easily separated into core and itinerant

electrons. The energies of the d-like states are comparable with those of the outer s- and p-states, and there is considerable overlapping between these states. These electrons, on the other hand, don't tend to be uniformly distributed outside the core but retain more of their original atomic character. However, this method is essentially plane wave outside the core and therefore, not good for describing this functions. The augmented plane wave method (APW) was originally developed to overcome difficulties inherent in the cellular method. In the later, it is difficult to satisfy the periodic boundary conditions for all point on the boundary of the unit cell. In APW method these boundary conditions are identically satisfied for all points on the boundary of the unit cell. The APW method is based on the so-called muffin-tin model of the crystal potential. The unit cell is divided two regions by non-overlapping spheres centered on each lattice site. Inside the sphere the potential is assumed to be spherically symmetric, and outside the sphere is relatively small fraction of the unit cell volume, and muffin-tin approximation is considerably good. While, as mentioned above, in OPW method the electrons in transition metals are not easily separated into core and itinerant electrons, APW method does not require this separation. Finally, one of the main advantages of APW method has been its applicability to both nearly free electron crystals and those containing transition method [1.2.8].

So far, we have considered the historical introduction of the 2D-ACAR experiment and the band structure calculation methods. We now turn our attention to the aim of the present work.

## I.3 Aim of the work

In the present work, 2D-ACAR spectra were measured for 7 projection angles for HCP structure samples and for 10 inclination angles for FCC and BCT structure samples in successive 5° step by rotating the samples around their Z-axis. From the obtained data, the electron density in the momentum space has been obtained using the reconstruction technique based on Fourier transform. Moreover, LCW folding procedure was used to construct the momentum space density n(k) in the wave vector space. The obtained results in the wave vector space depict Fermi surface, restricted within the first Brillouin zone. Consequently, the obtained Fermi surface was compared with some other publications for the samples under investigation. Furthermore, the normalized momentum density n(k)% for each sample is obtained and it was compared with the band structure calculations of some theoretical work. In this regard, the statistical analysis using least square fitting (SALS) method has been used to compare the band's occupations of the experimental with respect to the theoretical ones. Agreements and variations between the present work and the others have been obtained. These variations have been interpreted for each sample in view of the obtained results.

The motivation of undertaking and the aims of considering the present work are:

1. To check the applicability of the new 512 detectors system 2D-ACAR experimental set up, in measuring angular correlation of the annihilation radiation spectra.
2. To measure the 2D-ACAR spectra, then calculate the momentum space density and Fermi surfaces for the following materials:
   - the divalent HCP structure metals Mg, Zn and Cd,
   - the HCP structure metals of group IIIA Sc and Y,
   - the HCP structure metals of group IVA Ti, Zr and Hf,
   - the FCC structure metals of group VIII Rh and Ir,
   - the non-cuprate proveskite superconductor $Sr_2RuO_4$ and
   - the layered dichalcogenides of group VB $NbSe_2$.
3. To check the validity of the present 2D-ACAR experiment in measuring the high

material density (e.g. Ir).

4. To compare the measured Fermi surfaces for each metal with the other in the same group on one hand, and with the other publications on the other.

The present thesis is divided into four chapters. Next chapter of the current work is dealing with the theoretical considerations, started from 2D-ACAR spectra, electron density in momentum space and in wave vector space passing through reconstruction technique and LCW folding procedures. Chapter III describes the present experimental work, measuring programs, analysis programs and the error estimations. Chapter IV contains the experimental results and discussion. Finally, the last parts of the present thesis are the conclusions then the references.

# Chapter II

# Theoretical Considerations

## II.1 2D-ACAR spectra $N(P_y,P_z)$

When a high energetic positron emits from a radioactive source and it enters into a solid, it is rapidly slowed down in a few Pico-seconds by atomic ionization, excitation, positron electron collision and positron phonon interaction, until it reaches thermal equilibrium with the surrounding crystal. The mean implantation range varying from 10 to 100 μm sureties that the positron reaches the bulk of the sample materials. After reaching the thermal equilibrium, the positron becomes in the de-localized Bloch state in its own conduction band. Then it annihilates with an electron from the surrounding medium dominantly two 0.511 MeV γ-rays. The thermal motion of that positron obeys Boltzmann distribution as

$$f_+(E_+,T) = (\pi m^* k_B T)^{-3/2} \exp[-E_+ / k_B T] \qquad (2.1.1)$$

where $E_+$ denotes the positron kinetic energy, $m^*$ its effective mass and $k_B$ (=0.6337×10$^{-5}$ Ryd /K) is the Boltzmann constant. With $E_+ = P^2/m^*$, it is clear that,

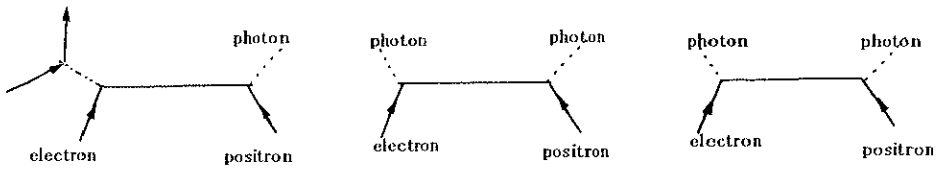


Figure 2.1.1 positron electron annihilation process yields one, two or three γ−rays

depending on temperature and effective mass, a positron displays a small motion that will broaden the momentum resolution function in an angular-correlation experiment (see subsection III.3).

The conservation of energy and momentum in the annihilation of positron-electron pair dictate the emission of one or more γ-rays, see Figure 2.1.1. The ratio of the cross sections for the two γ-rays $\sigma_{2\gamma}$ to the three γ-rays $\sigma_{3\gamma}$ is given as $\sigma_{2\gamma}/\sigma_{3\gamma}$=1114; taking into consideration the statistical weight of the triplet vs. singlet state this ratio becomes 1114/3 =371 [2.1.1]. Generally, Most positrons in condensed matter annihilate with the emission of two 0.511 MeV γ-rays. In the Laboratory frame the momentum of the electron–positron pair results in a small deviation from collinearity by a few Milli-radians (mrad). Figure 2.1.2 represents the observable characteristics of the two photons in the center of mass frame. $P_y$ and $P_z$

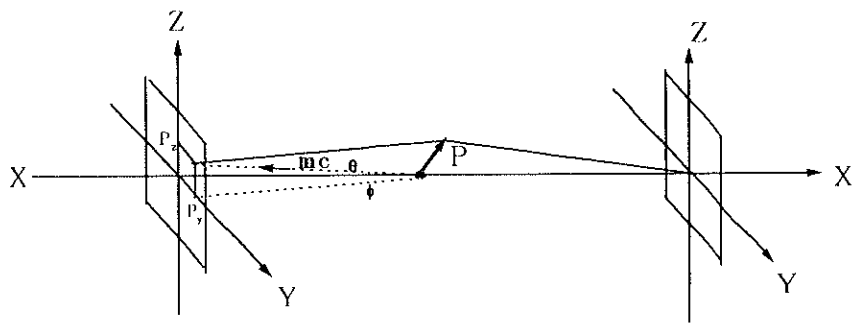


Figure 2.1.2 The geometry of the 2D-ACAR experiment.

are the momentum components in *Y*- and *Z*-directions, respectively. These components can be represented as

$$P_y = mc \sin\phi \approx mc\,\phi \qquad (2.1.2)$$

$$P_Z = mc \sin\theta \approx mc\,\theta \qquad (2.1.3)$$

This shows a good approximation, since the magnitude of the photon momenta in *mc* within one percent. The angular correlation between the photons, measured in

2D-ACAR experiment, is essentially the two dimensional projection of the momentum density distribution [2.1.1] of the photon pair ρ(P)

$$N(P_y, P_z) = const \cdot \int_{-\infty}^{+\infty} \rho(P)\, dP_x \qquad (2.1.4)$$

The conservation of the momentum in annihilation process can be represented as in the following equation

$$P = P_{e^-} + P_{e^+} = P_{\gamma_1} + P_{\gamma_2} \qquad (2.1.5)$$

Where $P_e^-$ and $P_e^+$ are the momenta of electron and positron, respectively, and $P_{\gamma 1}$ and $P_{\gamma 2}$ are the momenta of the two γ-rays. However, the momentum of positron in its ground state is negligible with respect to the momentum of electron. Therefore, the total angular momentum is considered to be that of the electrons.

$$P_{e^+} \cong 0$$
$$P = P_{e^-} \qquad (2.1.6)$$

## II.2 Electron density in the momentum space ρ(P)

The electron density in the momentum space ρ(P) was investigated under the two tentative assumptions [2.2.1]. First is, the Coulomb interaction between the electrons is treated separately from the interaction leading to the annihilation process. Second is, neglecting the possibilities that the annihilation of an electron from a specific state is accompanied by the transition of another electron to this state, i.e., the wave functions of the other electrons are not allowed to change in the annihilation process. Under these approximations, the annihilation probability of a specific electron and a positron into a pair of photons, over the entire occupied electron states, with total momentum P can be represented as the following expression

$$\rho(P) = const \cdot \sum_{n,k}^{Occ} \left| \int_{v} \exp[-iP.r]\varphi_{n,k}(r)\varphi_{+}(r)dr \right|^2 \qquad (2.2.1)$$

where $\varphi_{+}(r)$ and $\varphi_{n,k}(r)$ are the positron wave function and the electron wave function in $n$ band and $k$ wave vector, respectively. $v$ is the crystal volume and the summation is taken over all the occupied states. In the above equation we have ignored all the possible correlation effects. This equation forms the starting point for independent particles model (IPM).

The reconstruction technique based on Fourier transform [2.2.2] is represented as

$$FT_2[\rho(r)] = const \cdot \int \rho(P) \exp(-iP \cdot r)dP \Big|_{x=0}$$

$$= const.B(r) \Big|_{x=0} \qquad (2.2.2)$$

where, $B(r)$ is the auto correlation function of the wave function in the real space. It is expressed as

$$B(r) = (\frac{1}{2\pi})^{3/2} \int \rho(P) e^{-iP \cdot r} dP \qquad (2.2.3)$$

**For the simple non-interacting electron gas *B(r)* is given as**

$$B(r) = \frac{3}{(P_F . r)^2} [\frac{\sin(P_F \cdot r)}{P_F \cdot r} - \cos(P_F \cdot r)] \qquad (2.2.4)$$

**where, $P_F$ is the Fermi momentum. In this regard, the zeros of *B(r)* don't shifted by the resolution of the experimental set up. Since the resolution function that convolutes 2D-ACAR spectra becomes pouch function in Fourier space, thus damping the oscillation without shifting the zeros. Therefore, it becomes possible to determine Fermi momentum even for poor resolution.**

**Figure 2.1.3 shows schematic representation of different procedures of the reconstruction technique in the present work. For enough 2D-ACAR projections measured along different various directions, one can make 2D Fourier transform for each projection then interpolate the auto correlation function *B(r)*. Then the inverse Fourier transform yields the full reconstructed three dimensional electron density in the momentum space ρ(P). This means that 2D Fourier transform of 2D-ACAR results are proportional to the Fourier transform of ρ(P) evaluated in the plane going through the origin, and with a normal parallel to $P_x$, the integration direction for obtaining *N(Py, Pz)*.**

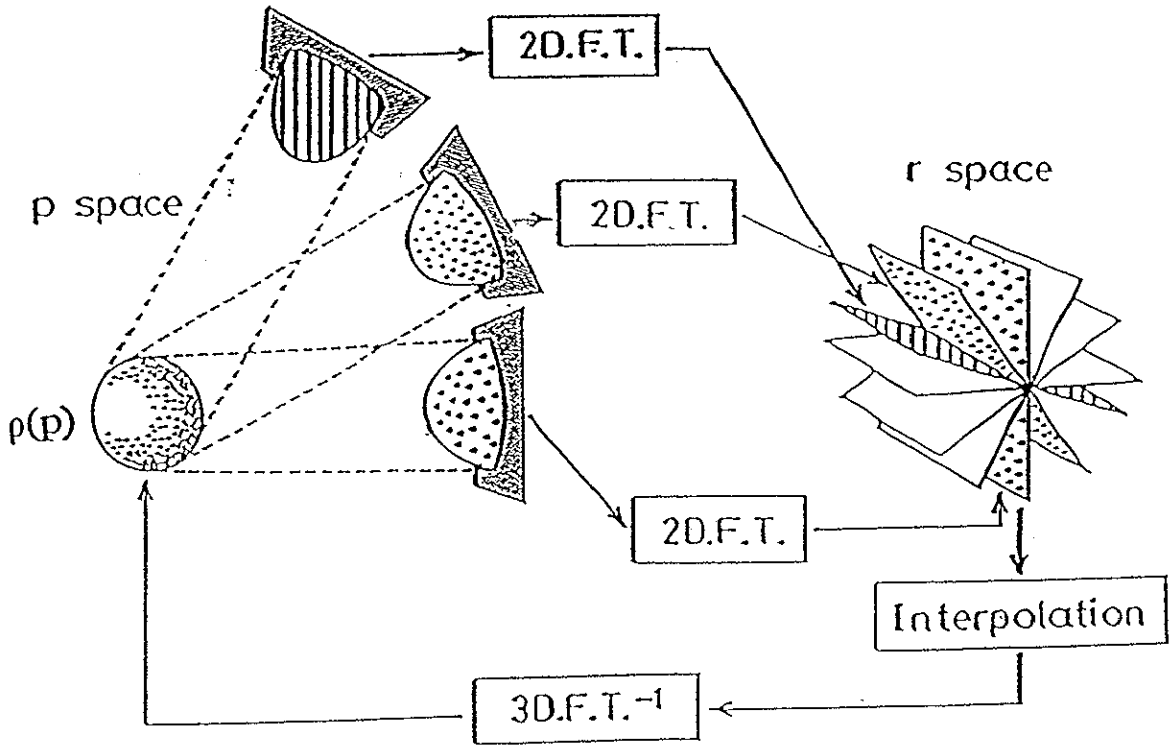


**Figure 2.1.3** schematic representation of different procedures of the reconstruction technique.

## II.3 High Momentum Components HMC's

In a periodic crystal of volume $V=N\Omega$, where $N$ denotes the number of the lattice sites and $\Omega$ denotes the volume of the unit cell, the positron and electron wave functions are the solution of the Schrodenger equation

$$[-\nabla^2 + V(r)]\varphi(r) = E\varphi(r) \tag{2.3.1}$$

Where $V(r)$ is the potential felt by the particle while it moves through the crystal. In the periodic crystal $V(r)$ is a periodic function of $r$, and the wave function has Bloch form

$$\varphi(r) = V^{1/2}U_{k,n}(r)\exp[ik.r] \tag{2.3.2}$$

where $U_{k,n}(r)$ has the periodicity of the lattice, $k$ denotes the wave vector of the particle, and $n$ labels the energy bands. The annihilation probability (equation 2.2.1) can be expressed as

$$\rho(P,T) = 2\sum_n f(E_{k,n},T) f_+(E_+,T)\left|A_n(P,k,k_+)\right|^2 \tag{2.3.3}$$

The factor 2 takes account of the spin degeneracy in the non-magnetic systems considered. $f_+(E_+,T)$ is the Boltzmann distribution (equation 2.1.1). $A_n(P, k, k_+)$ is the overlap integral

$$\begin{aligned}\left|A_n(P,k,k_+)\right|^2 &= \int \exp[-iP\cdot r]\varphi_{k,n}(r)\varphi_+(r)dr \\ &= V^{-1}\int \exp[-i(P-k-k_+)\,r]U_{k,n}(r)U_+(r)dr\end{aligned} \tag{2.3.4}$$

The integration in (2.3.4) which extends over the crystal, may be reduced to one over the unit cell by making use the periodicity of $U_{k,n}$ and $U_+$,

$$A_n(P,k,k_+) = \Omega^{-1}\delta(P-k-k_+-G)\int_{\Omega}\exp[-ik\cdot r]U_{k,n}U_+(r)dr \qquad (2.3.5)$$

**The delta function expresses momentum conservation; the momentum carried off by the photons equals that of the two particles up to a reciprocal-lattice vector. Thus at $T=0$, with the positron in its ground state $k_+=0$, an electron with the wave vector k contributes to ρ(P) not only at $P = k$ (normal process), but also at $P = k + G$ (Umklapp process), and $G$ is the reciprocal lattice points. The contribution with $G \neq 0$ are commonly called the high momentum components (HMC's)**

## II.4 LCW (Loucks, Crisp and West) folding procedure

The momentum associated with a state of Bloch wave vector $k$ is distributed through out the momentum density by the positron and electron eigen functions. The LCW folding procedure [2.4.1] can reduce the electron density in the momentum space to the electron density in the wave vector space, k-space, restricted within the first Brillouin zone as follows,

$$n(k) = \sum_i \rho(P + G_i) \tag{2.4.1}$$

with, $\hbar = 1$ .

Where $G_i$ is the *i th* reciprocal lattice vector and $k$ is the wave vector defined within the first Brillouin zone. The Bloch theorem describes $n(k)$ as

$$n(k) = const_{n,k} \sum \theta(E_F - E_{n,k}) \int_{cell} |\varphi_+(r)|^2 |\varphi_{n,k}(r)|^2 dr \tag{2.4.2}$$

Where $E_F$ and $E_{n,k}$ are the Fermi energy and the energy of the electron at the state $n$ and wave vector $k$, respectively. $\theta(E_F - E_{n,k})$ is a step function in which,

$$\theta(E_F - E_{n,k}) = \begin{cases} 1, E_F \geq E_{n,k} \\ 0, E_F < E_{n,k} \end{cases} \tag{2.4.3}$$

Therefore, $n(k)$ should have breaks corresponding to the breaks in the integral in equation (2.4.2) between inside and outside of Fermi surface. The Fermi surface discontinuities are reinforced while all other parts of the original momentum density sum into a large intensity but relatively smooth background. That is a summation of the individual band occupancies in $k$, and that contains all the wave function effects.

The band number of the Fermi surface sheets can be calculated by normalizing $n(k)$ to the total momentum density, along different principal symmetric lines, as

$$n(k) = \frac{n(k)}{\int n(k)\,dk \;/\; \int dk} \times 100 \qquad (2.4.4)$$

This corresponds to the assumption that the wave function of the positron is uniform in the whole space. In that approximation, the positron wave function is constant or that the electron states are simple plane wave. Consequently, the electron $k$-space density is that which arises from Fermi surface. In reality, the positron wave function effect varies from band to band and each has its own k-dependence. However, because of the orthogonality of the electron states, when they are summed over all the occupied states their overall effect can be quite small. In the present metals, which contain d-like states, this effect is not negligible. In order to correlate the effect of the positron wave function we used the statistical analysis using least square fitting (SALS) method (see subsection III.2.4b). This by including the experimental values of $n_{exp}(k)$ with that obtained using the band structure calculation $n_{th}(k)$. By applying the least square method, using the experimental results with the theoretical ones, the best fitting position for the bands could be determined. This corresponding to the following equation

$$\sum_{k} (n_{\exp}(k) - n_{th}(k))^2 = Min. \qquad (2.4.5)$$

where $n_{exp}(k)$ and $n_{th}(k)$ being the experimental and theoretical values of the electron density in wave vector space. The obtained results from this analysis show the band number n-dependence as well as the wave vector k-dependence.

The dimensions of the Fermi surface sheets are calculated from the maximum of the gradient of the momentum density $n(k)$. When the resolution is finite, the singularity on the line normal to the Fermi surface appears as a peak like experimental resolution function. We calculated

$$\left|\nabla n(k)\right| = \left|\frac{\partial n(k)}{\partial k_x}k_x + \frac{\partial n(k)}{\partial k_y}k_y + \frac{\partial n(k)}{\partial k_z}k_z\right| \qquad \textbf{(2.4.6)}$$

**where $k_X$ , $K_Y$ and $k_Z$ are the unit vector in k-space, and then performed the mapping out of $/\ \nabla n(k)\ /$ to trace the ridge of the singularity peak.**

## II.5 The enhancement effect

The obtained ρ(P) by the positron annihilation experiment is the probability for the two-photon event with the total momentum *P*. The presence of the positron in the metal doesn't change Fermi momentum $P_F$ (as the positron thermalized before annihilation) but, unfortunately, deform the electronic wave functions (the electron density is enhanced at the positron position). ρ(P) increases as *P* approaches the Fermi surface. This momentum dependence is attributed to Pauli exclusion principle, which inhibits positron interactions with electrons deep inside the Fermi sea. This is called the enhancement effect. Kahana [2.5.1] represents ρ(P) as the following expression in an interaction electron gas.

$$\rho(P) = \varepsilon(P) \cdot \rho_{IPM}(P) \tag{2.5.1}$$

Here, ε(P), which depends on the enhancements of various electronic states, is not quantity that can be essentially extracted from the experiment as far as information about the electron-positron interaction. The description of the real behavior of the momentum dependent enhancement factor is given using Kahana formula,

$$\varepsilon(P) = a + b\gamma^2 + c\gamma^4$$
$$\varepsilon(P) = a[1 + (b/a)\gamma^2 + (c/a)\gamma^4] \tag{2.5.2}$$

where a, b and c are the enhancement parameters.

and, $\gamma = (P/P_F)$

# CHAPTER III

## Experimental set-up, Data analysis and Error estimation

## III.1 Experimental set up

**The present 2D-ACAR experimental set up consists of three main parts; a pair of multi-detectors system; a central source-sample vacuum chamber; and an auxiliary electronic and control.**

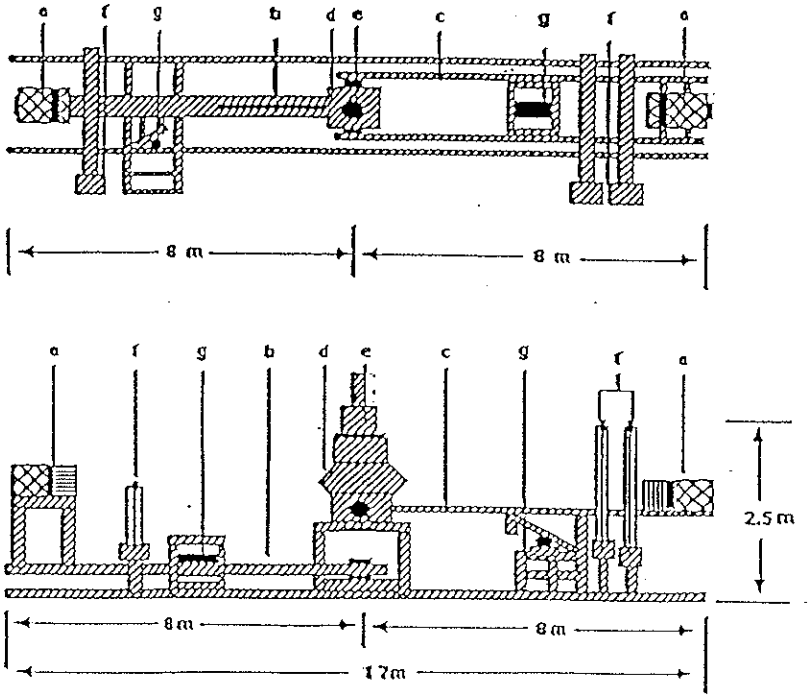


2D-ACAR Experimental set up
a) BGO detector
b) Horizontal arm
c) Vertical arm
d) Magnet
e) Central source-sample vacuum chamber
f) Balance weight
g) Automatic arm driving system

Figure 3.1.1 schematic representation of the main parts of the present 2D-ACAR experiment.

### III.1.1 A pair of multi-detectors system

**The present 2D-ACAR data were measured using two experimental set-ups. In the first, a pair of 128 detectors was used to construct the 20 mrad x 20 mrad spectra. In the second, a pair of 256 detectors was used to construct the 30 mrad x 30 mrad.**

In the next paragraphs we will discuss the later. Figure 3.1.1 shows a schematic representation of the main parts of the present 2D-ACAR experimental configuration.

The spectra were measured by cross correlation machine consists of a pair of 256 $Bi_4Ge_3O_{12}$ (BGO) multi-detectors. They are combined to the same number Hamamatus R-647 ultra compact photo-multiplier tubes. A distance departs both of the pair multi-detectors from the central source-sample vacuum chamber 8 meters long. The detectors in each array are mounted in a frame and arranged as 16×16 detectors each two detectors have successive distance 1.6 Cm. Thus, the distance between each two successive detectors is 2 mrad. A lead collimator of 5 Cm in thickness and 16×16 holes is settled in front of each detectors array, to collimated the emerging γ-rays from the sample. The collimator's holes have a diameter 0.6 Cm. This allows a resolution of 0.75 mrad for each detector (see subsection III.3). Two large arms are carried the two detectors arrays and they are rotated as a step of 0.2 mrad one in a horizontal direction (H-arm) and the other in a vertical direction (V-arm). Each detector array is mounted on the modified milling machine base, which allows for precision positioning, by a stepping motor. The rotational movement is controlled through the CPU of the experiment using a digiruler and stepping motor. The movement of the two arms is adjusted to be 0.2 mrad/step.

### III.1.2 A central source-sample vacuum chamber

It consists of two parts, fixed rectangular container carries the source and movable cylindrical container carries the sample holder (see Fig. 3.1.2).

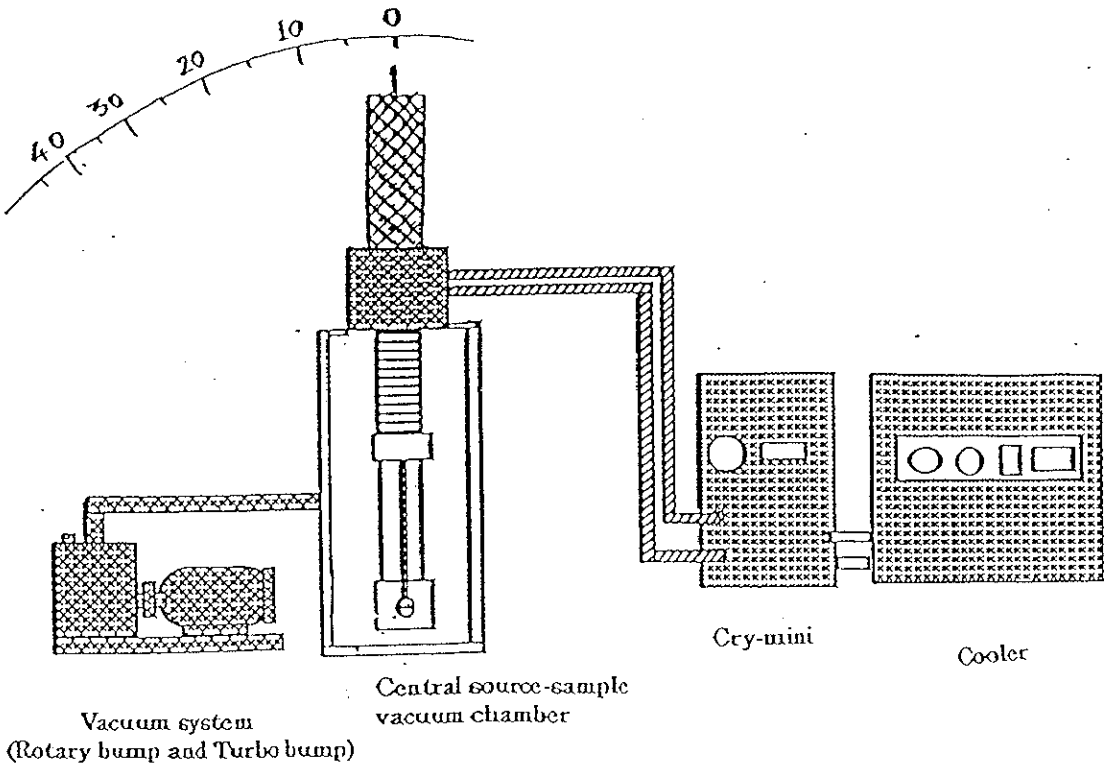


Figure 3.1.2 schematic representation of the central source sample vacuum chamber with its connections to the cryo-mini, vacuum system.

The source holder is carrying the $Na^{22}$ radioisotope in its center. The activity of the used radioisotope is about 80 mCi at the date of production, it was used as a positron emitter. Figure 3.1.3 shows the decay scheme of the $Na^{22}$ and schematic representation of its spectra. The fixed rectangular has two windows. These windows are directed towards the moving multi-detectors, V-detectors and H-detectors arrays. A thin film covered these windows to allow γ-rays to emerge towards V- and H- multi-detectors. The fixed container is connected to the vacuum system, which consists of rotary pump and turbo pump. Vacuum gage was used to measure the vacuum in the source-sample vacuum chamber. The vacuum about $2 \times 10^{-8}$ torr has applied to the central source-sample vacuum chamber.

A lead shield surrounds the fixed container from all directions. This lead shield has two slits towards V- and H- detectors arrays, to allow γ-rays to emerge towards the multi-detectors (see Fig. 3.1.4). The movable cylinder contains head motor of the cryo-mini in its upper part, which in turns connected to the He-container through two hoses. The used cryo-mini in the present experiment allows the temperature of the sample to be about 28 K in order to minimize the effect of the residual momentum due to the thermal motion of the positrons. At the end of the movable cylinder there is a bar carrying the sample holder and the heater.

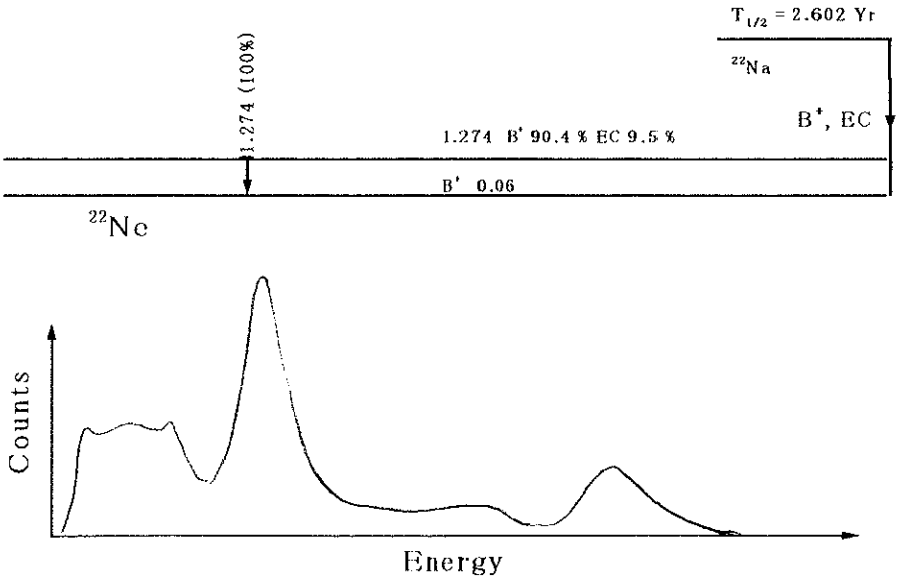


Figure 3.1.3 (a) the decay scheme of the $^{22}$Na spectra
(b) schematic representation of $^{22}$Na spectra

The samples are fixed on a sample holder in (001) plane for FCC structure and in (0001) plane for HCP structure samples. The whole source-sample vacuum chamber can rotate around the source-sample direction, to measure the spectra of different angles without opening the vacuum chamber; also this way gives high precession of the rotational angles. Finally, A large magnet of 1.5 T surrounds the source-sample vacuum chamber in the way that the flux is in parallel direction to the emerging direction of positrons.

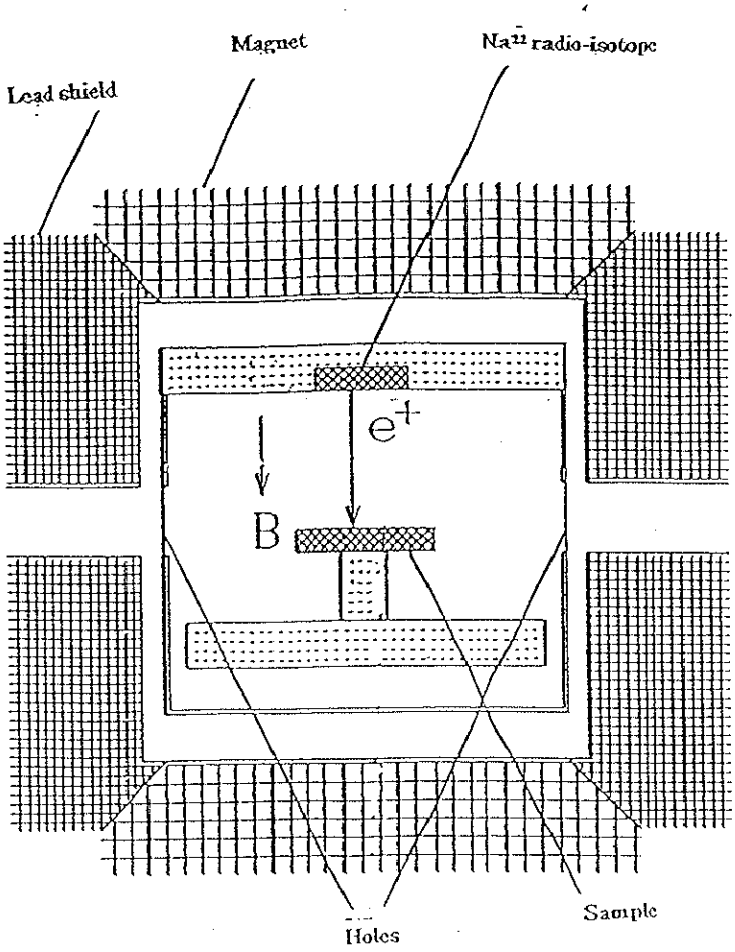


Figure 3.1.4 cross section view of the central source sample vacuum chamber.

### III.1.3 An auxiliary electronic control

Figure 3.1.5 represents a schematic diagram of the measurement control and the electronics. When a positron enters the sample, it annihilates with an electron and emits two γ-rays are nearly linear. The γ-rays interacts with the BGO scintillation crystal emitting a visible light that in turns interacts with the photo cathode in the photo-multiplier tube to emit electrons. These electrons are multiplied by means of the dynodes in the photo-multiplier tube. Then, this constructs the out put signal, which represents the incident 0.511 MeV γ-ray. The output signal from the PMT passes through the Amplifier-Discriminator circuits, then to the OR-circuits, finally this signal goes to the CPU, in which it collected as 2D-ACAR data array in the PC. In the next subsections the task of different circuits will be explained.

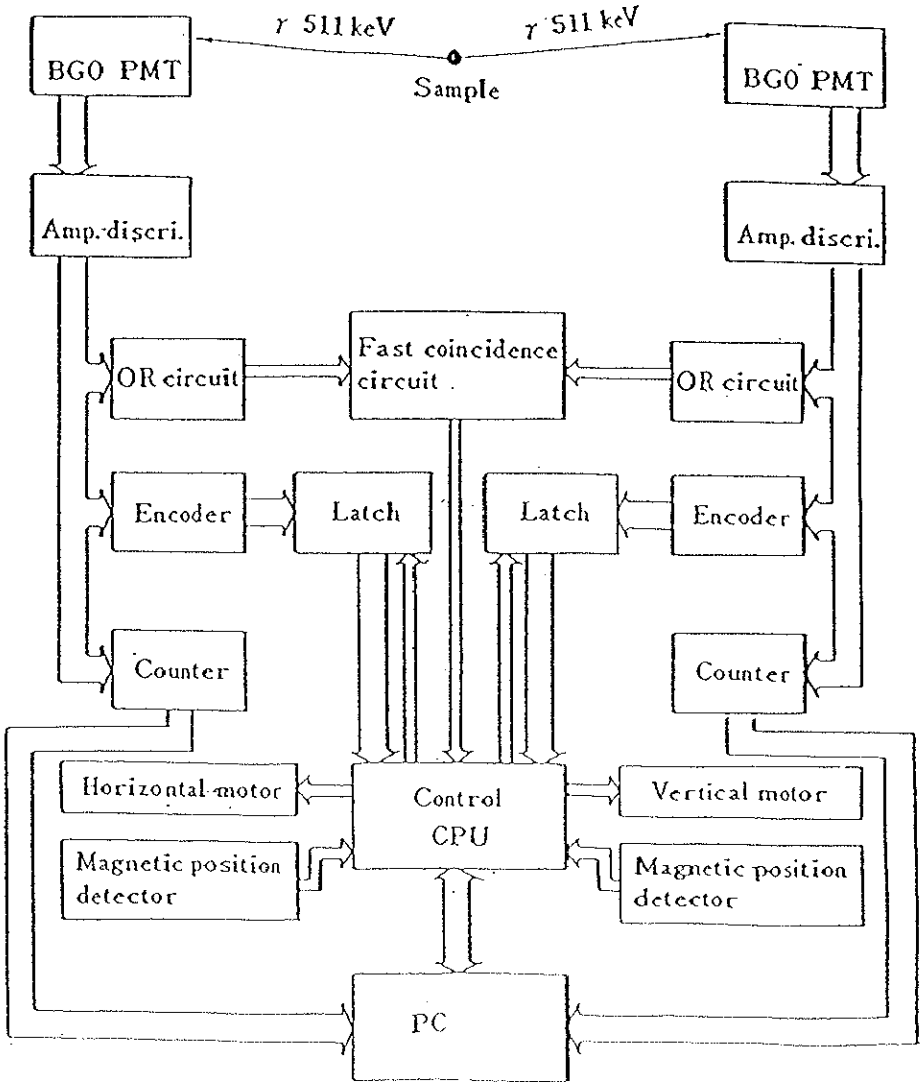


Figure 3.1.5 schematic diagram of the measurement control and electronics.

### III.1.3a Amplifier-Discriminator circuit

The amplifier-discriminator circuit consists of two circuits the first is the amplifier circuit that responsible to amplify the output signals from the PMT then send it to the discriminator circuit. The second is the discriminator circuit that responsible to discriminate the energies of the output signals. Using the multi-channel analyzer, we cut the energies over the 0.511 MeV of the signals.

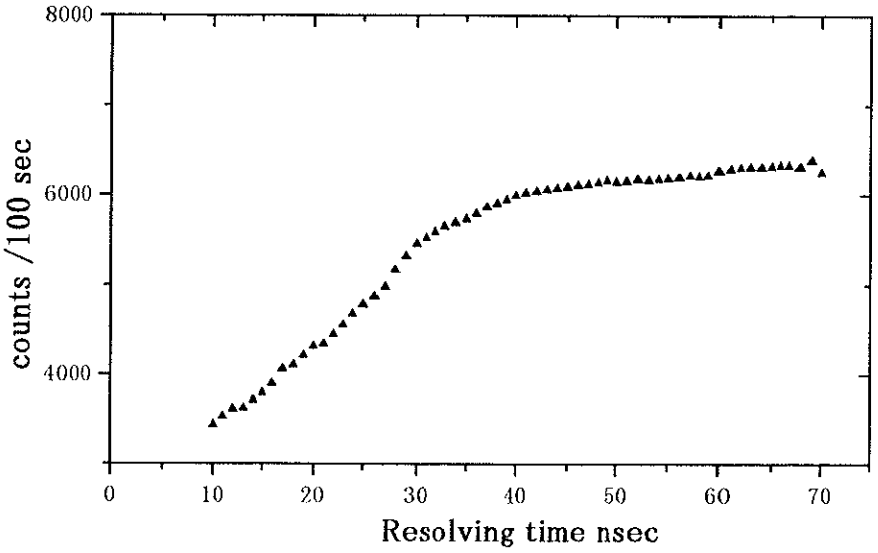


Figure 3.1.6 the total coincidence counts as function of the resolving time using the fast coincidence model (ORTEC 414A).

### III.1.3b OR-circuit

The main task of the OR-circuit is to collect the output signals from the 256 channels (from each detector in the array). It divided into four OR-circuits in each detector arrays each carrying 64 signals. The output signals are passed through three stages OR-circuits connected in series and collected through fast coincidence model (ORTEC 414A). The obtained signals are collected as total coincidence signals in the CPU then in the PC. The resolving time of the fast coincidence is checked experimentally and adjusted to be 55 nsec. Figure 3.1.6 represents the experimental values of the coincidence counts as function of the resolving time.

This Figure shows that as the resolving time increases the total coincidence counts increases up to 40 nsec. Then the gradient of the curve becomes smaller over 40 nsec. This curve explain the features of the total coincidence, the true coincidence and the accidental coincidence in which

The total coincidence counts = the true coincidence counts + the accidental coincidence counts.

We choose the resolving time in the present experiment to be 55 nsec, in which the accidental coincidence becomes small.

### III.1.3c The encoded circuit

The encoder fits the output from the detector's position where γ-rays enters. It consists of four circuits each carries 64 signals from 64 PMT's. These signals are carried to the CPU through the latch signal, which in turns is moving from CPU to the encoded circuit. During the time of the experiment the latch signal keep moving and carrying the encoded signals with its position information. The output signals from the encoded circuit are collected in the CPU with its position's information, then it recorded in the PC as 256 ×256 2D-ACAR data array.

### III.1.3d The counter circuit

The main task of this circuit is to get the single counts from every detector in the two arrays. Thus, the output signal from the counter circuit goes directly to the computer to be detected as single counts. In the counter circuits the data are performed by 64 bit (binary system) and it is performed as 4 bits (hexadecimal system) in the PC. The counter circuit includes four IC's. The 1$^{st}$ is model "Z80CTC", the second is ROM (2764) which carries the program in the machine language. The third is RAM (6264) which is accountable on putting the obtained output to the fourth one, "Z80PIO" that exchanges the data with "Z80CTC".

### III.1.3e The CPU

The CPU includes CTC board, and 8801 IC board. The CTC board is for fitting the measurements. 8801 IC board is using for reading the value of the stepping motor device and the digiruler. It is also performed the readings of the encoded data. The CPU should reset before the measurements. It has many tasks

1. The adjustment of the arms' location using the digiruler.
2. Controlling the movement of the stepping motors.
3. Controlling the coincidence data and entrustment it to the PC.
4. It is also fit the measurements time utilizing the CTC board.
5. It controls the other boards and exchanges the data with the PC.

## III.2 Data Analysis

As mentioned above the coincidence signals are recorded in the PC as an update data array. These data are used to construct the 2D-ACAR spectra, which in turns are used to get ρ(P) then n(k). In this section, the analysis of the data through different techniques will be discussed.

### III.2.1 Experimental data

After 100 run the measurement stopped and the data are recorded in the PC as 256 x 256 data array, for each run. This shows 100 data arrays each one contains 256 x 256 data, for each spectrum. This data represent the recorded coincidence events from every detector in each array to each detector in the other array. There are four main steps to analyze the 2D-ACAR spectra from this data; the experimental effective efficiency; the 60 x 60 spectra; the multiplicity; and the 300 x 300 2D-ACAR spectra.

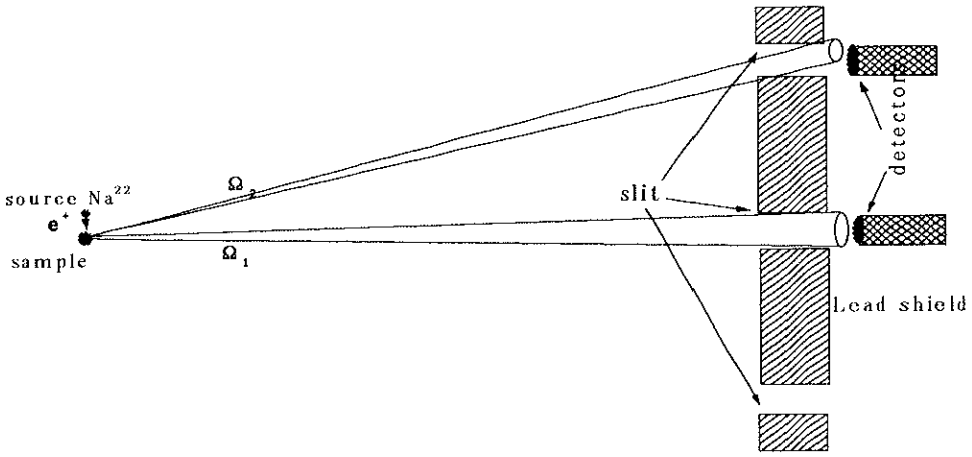


Figure 3.2.1 schematic representation of the solid angle of the incident γ-rays on the slit shield, $\Omega_1$ and $\Omega_2$ are the solid angls

### III.2.1a The experimental effective efficiency

Figure 3.2.1 shows schematic representation of the emerging γ-rays from the sample to the detector array. As can be noted from this figure, while a lead collimator collimates γ-rays, their solid angles decrease as the detector departed

from the center of the arrays. In order to avoid the effect of decreasing the solid angles on the spectra, we measure the single counts for each detector in the two detector arrays. The obtained results show 256 × 256 experimental effective detector efficiency. Then, the results of dividing the experimental data by the

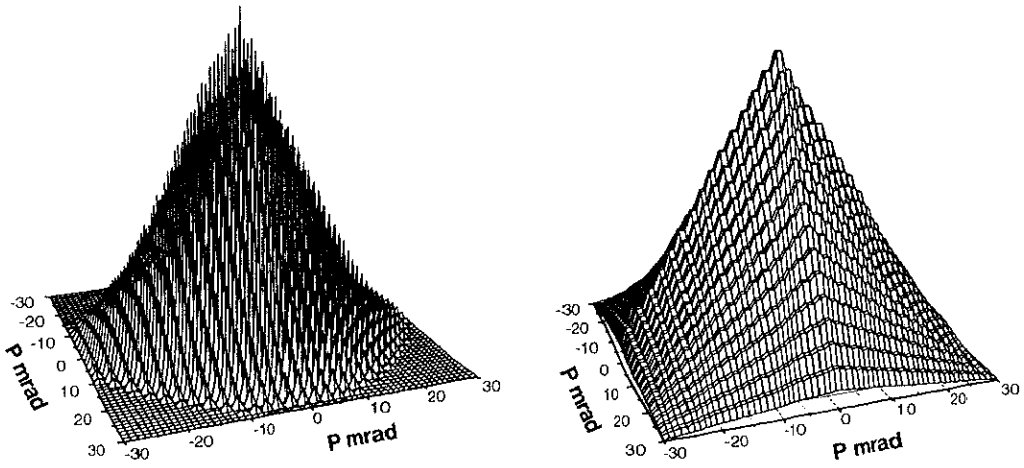


(a) (b)

Figure 3.2.2 (a) 60 x 60 spectrum. The difference between each two data is 2 mrad. (b) the multiplicity spectrum for 30 x 30 mrad

effective detector efficiency gives the 256 × 256 raw data.

### III. 2.1 b The 60 × 60 spectrum

The 256 × 256 data show the correlated coincidence events between the detectors in different detectors arrays. We converted the 256 × 256 raw data into 60 × 60 data Using the "cnt2ch.cpp" program, for each run. This shows 100 data each contain 60 × 60 data array. The later data show how many pairs of γ-rays incident by different deviation angles to the two detector arrays. The distance between each two points in the spectrum is 2 mrad equal to the distance between each two successive detectors in each detector array. Figure 3.2.2a shows the 60 × 60 spectrum for one array of the measurements.

### III.2.1c The multiplicity

It is defined as the probability that a pair of γ-rays of one event (annihilation) incident on the detectors by different angles. This probability is very high in the center of the spectrum and gradually decreases as going to the corner. This means that the multiplicity decreases as the deviation angle between the two γ-rays increases. The obtained 60 ×60 spectrum includes that probability. Figure 3.2.2b show the multiplicity spectrum for an identical pair of 256 detectors arrays. The "calcmult.cpp" program has been used to divide the spectrum by the multiplicity, then the real 60 × 60 spectrum is obtained.

### III.2.1 d 300 × 300 2D-ACAR spectrum

As mentioned above that the 60 × 60 spectrum has a distance of 2 mrad between each successive data. The 100 spectra are represented as 10 × 10 spectra of

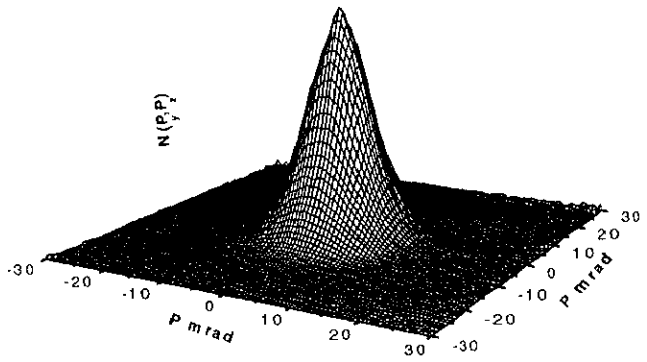


Figure 3.2.3 the measured 300 x 300 2D-ACAR spectrum.

0.2 mrad deviation between each two successive spectra. These spectra are added with their 0.2 mrad deviation to get 300 × 300 data. This data construct the 2D-ACAR spectrum. Figure 3.2.3 shows the obtained 2D-ACAR spectrum of Rh, for 0° deviation angle from [001] projection direction. Finally, the obtained spectra for

different deviation angles for each metal can be obtained by the same way.

For the experimental data analysis we used the batch file " calc100m.bat" to make all of the above-mentioned procedure. The obtained data, then, copied on the MO preparing for the FACOM and the spectrum analysis.

### III.2.2 FACOM and spectrum analysis

The obtained 2D-ACAR spectra is the two dimensional projection of the electron density in the momentum space. The spectrum is analyzed by different method to obtain the experimental results. We used the FACOM system for this analysis because it requires large memory space and long time of analysis. In order to transfer the data we used also the file transfer program FTP, to get the data from MO to the FACOM system. Then the obtained spectrum passes through different technique, deviation, center, folding, reconstruction and LCW. In the following sections these techniques will be discussed.

### III.2.2a Peak Deviation

If the sample center is not aligned precisely on the axis defined by the two detector centers, the symmetry of the spectra can be badly hidden. Here, to determine the deviation from the center we used "ndev" Fortran program. This technique is calculating the integrated counts in one direction then calculate the total counts and divided by 2. Then, start adding from the first channel until the added counts become equal to half of the total counts. This channel shows the deviation in one direction. Then applying this procedure on the other direction to get the deviation in the other direction.

### III.2.2b Peak Center

In order to return the spectrum to its original center we used the "center" program. It bases on shifting all the data points by distance equal the obtained deviation using subroutine "Akmid". The method is based on moving one direction a distance equal to the deviation, then move the other direction a distance equal to its deviation from the center. Figure 3.2.4 shows the contour map of 2D-ACAR

spectra as (a) experimental raw data before moving the center and (b) after moving the center.

### III.2.2c Peak Folding program

Each part of the obtained spectrum contains some information about the momentum density. In order to get all of the these information we used the "twofold" Fortran program, that fold the two halves of the spectrum along one

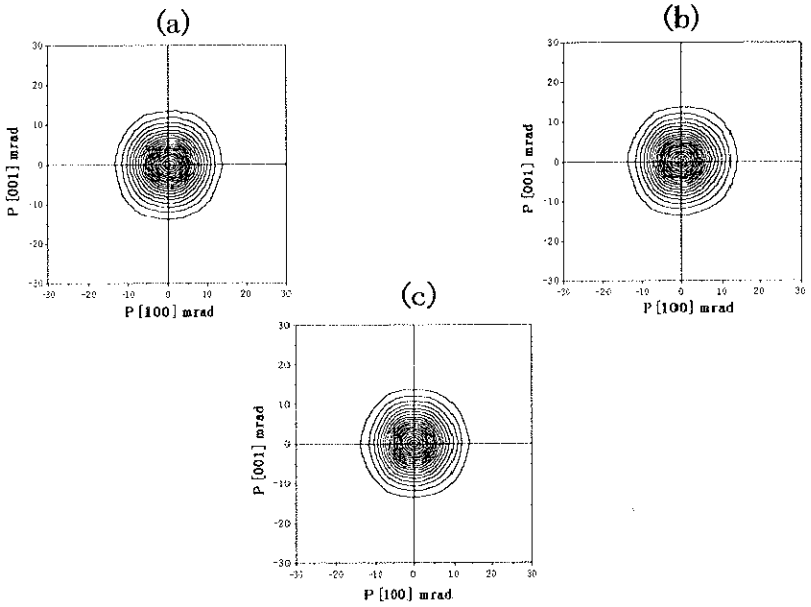


Figure 3.2.4 the contour map of the 2D-ACAR spectra represented as a contour map.
(a) before shifting the center
(b) after shifting the center
(c) after using the two fold symmetry.

direction then rewrites the mean in the same two halves. Then doing the same procedure in the other direction. Figure 3.2.4(c) shows the contour of the spectrum after using the " twofold" program.

### III.2.3 Reconstruction program

The reconstruction technique based on the direct Fourier transform is used to get three dimensional momentum density ρ(P). For the HCP structure materials 7 spectra of different inclination angles on the [0001] projections direction are required. For FCC and BCT structure materials 10 spectra of different inclination angles on the [001] projection direction are required. The reconstruction program includes the two-dimensional Fourier transform, interpolation and the three dimensional inverse Fourier transform. The obtained results from this program are the three dimensional electron density in the momentum space ρ(P). The size of the data is about 17 Mbytes for each material. Another data could be obtain from this program, it is the auto correlation function of the wave function in the real space B(r), and also it has the same memory size. The reconstructed data are cut to get ρ(P) in different plane of symmetry. The programs "DMGMK", "DMALM" and "DMAHK" are used to get ρ(P) in (ΓMK), (ALM) and (AHK) planes, respectively, for the HCP structure materials. The programs "DM001", "DM100", "DM110" and "DM111" are used to get ρ(P) in (001), (100), (110) and (111) planes, respectively.

### III.2.4a LCW Folding program

LCW Fortran program is used to reduce the ρ(P) to the electron density in the wave vector space n(k). "HCPLCW", " FCCLCW" and "BCTLCW" programs are used to get n(k) of the HCP, FCC and BCT structure, respectively. Before using this program, the lattice parameters of the sample should be calculated as follow;

- The lattice constants of the used metals should be obtained.
- For the HCP structure metals, the lattice constants a and c are required. Then calculate the lattice parameters as

$\Gamma M = \{3/4\}^{1/2} (2\pi/a)$

$\Gamma K = (2\pi/a)$

$\Gamma A = (2\pi/c)$

- For the FCC structure metals

$\Gamma X = 2 \times (2\pi/a)$

- For the BCT structure metals

$\Gamma X = 2 \times (2\pi/a)$

$\Gamma Z = 2 \times (2\pi/c)$

This LCW programs are based on dividing the spectrum into many parts each equal the lattice parameters, which in turns determined the Brillouin zone of the used metal. Then folding the divided parts to be included in the 1st B.Z. Consequently, the obtained results represent the three dimensional electron density in the wave vector space. To cut n(k) in different planes, we used three Fortran programs. First is "GR" to cut n(k) as a plane perpendicular to the c-axis. Second is "CUTLCW" to get the different plane of symmetry of Brillouin zone. The third is "WRTLCW" to get n(k)% in different symmetric directions. In order to calculate the Fermi surface dimensions we used also " CUTLCW" to get the differential of the n (k).

III.2.4b Statistical analysis with least square fitting (SALS) program

A present program has used the SALS to make least square fitting for the experimental data of the normalized momentum density in the wave vector space with respect to the theoretical band structure calculation. The input data is the number of data, the number of the band's width and the number of bands obtained by the theory

The procedure of the program:

1. read number of experimental data.
2. read the band numbers.
3. read the width of the intervals (the intervals here is the width of the band in k-space).
4. read the input data (the experimental data of the normalized momentum density in the wave vector space of the sample under consideration ).
5. get the minimum value of n(k).
6. write the output data as the band value.

### III.2.5 Other programs

In order to get the figures of the spectra we used two main programs. "3D30A" and "cont30" for drawing the isometric view and the contour map, respectively. This program gets the isometric view and the contour map of the sample in different angles.

### III.2.6 Origin software

Another way to get the figure of the obtained results is the ORIGIN software. We used here the ORIGIN 3.5 and ORIGIN 5.0 versions. In order to use the data from FACOM, we used the "I30IT10" Fortran program to get a compressed 100 × 100 data from the 300 × 300 data. Then transfers it through the ASCII mode to the PC.

## III.3 Error Estimation

There are three main sources of errors in the present measurements. These errors are; the error due to the angular resolution of the thermal motion of the positron; the error due to the detector resolution; and the error due to the reconstruction technique based on Fourier transform.

### III.3.1 Angular resolution and positron thermal motion

The thermal motion of the positron obeys the Boltzmann distribution equation (2.1.1). It is clear that the positron displays a small thermal motion, which will broaden the momentum resolution function in the angular correlation experiment. The resolution function in the *Pz* direction can be expressed as

$$\begin{aligned} R(P_z) &= \exp\left[ -\frac{P_z^2}{2m^* KT} \right] \\ P_z &= mc\ \theta_z \\ R(\theta_z) &= \exp\left[ -\frac{(mc\ \theta_z)^2}{2m^* KT} \right] \end{aligned} \tag{3.1}$$

the resolution function at the full width at half maximum (*FWHM*) is

$$R(\theta_z) = \frac{1}{2},$$

where, $m^*$ is the mass of the positron and it considered to be twice of that of electron

$m^* = 2m$

$$\theta_{1/2} = \left( \frac{4KT \ln 2}{mc^2} \right)^{1/2} \tag{3.2}$$

$$FWHM = 2\theta_z$$

using the cryo- mini (see subsection III.1.2) the temperature of the sample reaches 28 K. The estimation of the error in the (*FWHM*) due to the thermal motion of the

positron is

at $T = 28$ K , $\theta_T = 0.24$ *mrad*

### III.3.2 The estimation of the error due to the detector resolution

The error due to the detector resolution can be expressed as

$$\Delta_D = D / L \tag{3.3}$$

where, $D$ denotes the diameter of the hole in the lead shield

$L$ is the distance between the slit and the sample

In the present measurements, the diameter of the lead-shielding slit is 6 mm, and the distance between the sample and the detector is 8000 mm, then the estimation of the error due to the resolution of the detector is

$$\Delta_D = 6/8000 = 0.75 mrad$$

### III.3.3 The estimation of the error due to the reconstruction technique

The reconstruction technique based on Fourier transform *FT*-theorem has been used. There are two main problems in using this technique. They are; the noise and the number of the projection required for the construction. In the present experiment, we have followed carefully the noise and the noise propagation. The second is the number of projections. In principle the use of a finite number of projections includes an effective resolution in the reconstructed data. Even for poor experimental resolution and more projections would show better results. In the present experiment, the numbers of projections are 10 for the FCC and BCT structure and 7 for the HCP structure materials. In order to calculate the error

due to the reconstruction technique, we calculate the FWHM of the reconstructed spectra and compare it with the original spectra (2D-ACAR spectra) in the same directions. The difference at *FWHM* was nearly 0.02 a.u.. Consequently, the error in determining the sheets of Fermi surface will be about 0.02 a.u.

# CHAPTER IV

## Results and Discussions

## IV.1 The divalent HCP structure metals Magnesium (Mg), Zinc (Zn) and Cadmium (Cd)

**The motivation of undertaking and comparing the divalent HCP metals Mg, Zn and Cd in the present work based on the following two facts:**

**a) These metals have an axial ratio c/a varies from close to ideal Mg (=1.623) to far from ideal Zn (=1.828) and Cd (=1.862)[4.1.1].**

**b) Some of them can be placed in the transition series and since they are nearly free electron-like, details from their s-electron conduction bands are mainly determined by crystal symmetry and lattice parameters.**

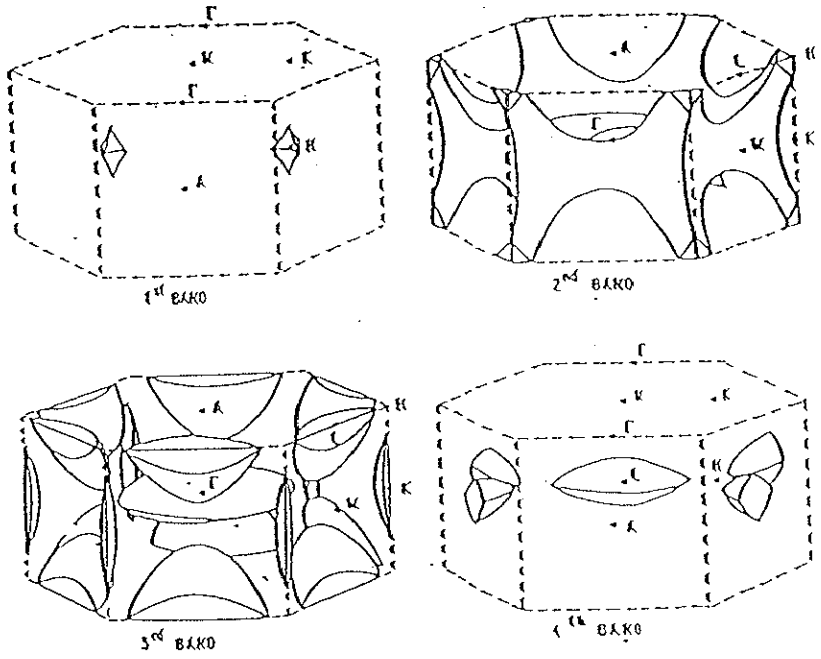

Figure 4.1.1 the free electron Fermi surface of the divalent HCP structure materials including the spin orbital effect shows six sheets of Fermi surface;

- the 1st band hole surface around H point (cap)
- the 2nd band hole (monster)
- the 3rd band electron surface at Γ point (lens)
- the 3rd band electron surface at K point (needles)
- the 3rd band electron surface at L point (butterfly)
- the 4th band electron surface at L point (cigar)

**The free electron model including spin orbital effect for divalent HCP of ideal c/a ratio predicts six different sheets [4.1.2]. These sheets are; the 1st band contains a hole centered on H points (cap), which has been separated by the spin orbital splitting from the main region of the 2nd band; the 2nd band contains a multiply**

connected surface hole (monster); the 3rd band contains electron sheets centered on Γ point (lens), on L point (butterfly) and on K point (needles)(the needles are not predicted for Cd in the free electron model); and the 4th band contains an electron surface centered on L point (cigar) which is formed within the intersection of the two wings that comprise the butterfly (see fig. 4.1.1).

The axial ratio c/a has a prominent effect in the shape and the size of Fermi surface sheets, especially needles, since its critical value at which these needles disappear is 1.861[4.1.3], while it is smaller than (c/a) ratio of Cd. A number of studies of the Fermi surface of Mg [4.1.4- 4.1.9] ,Zn [4.1.10- 4.1.13] and Cd [4.1.14-4.1.16] and some comparative studies[4.1.17-4.1.19] have been performed. However, not all the results agree with each other even qualitatively. Furthermore, the results of Zn and Cd have shown discrepancies from each other in the dimensions of some Fermi surface sheets.

### IV.1.1 2D-ACAR spectra, and electron density in the momentum space ρ(P)

The measured 2D-ACAR spectra of Mg, Zn and Cd are represented in Figs. 4.1.2, 4.1.3 and 4.1.4 as (a) isometric view and (b) contour maps. The written angles on the spectra represent the inclination angles on the [0001] projection direction ranging between $0^{o}$ to $30^{o}$. In the contour map, the contours are represented as 2% from the peak's heights. These spectra show deformations in their upper parts, they are attributed to the Brillouin zone interaction. ρ(P) is obtained by reconstructing the measured 2D-ACAR spectra, using reconstruction technique based on Fourier transformation equation (2.2.2). Figures 4.1.5, 4.1.6 and 4.1.7 represent ρ(P) in ΓMK, ALM and AHK planes as (a) contour map and (b) isometric view for Mg, Zn and Cd, respectively. These figures show some important features namely; the contribution due to the interaction of the positron with the core state; the contributions of the high momentum components (HMC's) which are attributed to Umklapp process; and distortions in the upper parts of the spectra which are attributed to Kahana-like enhancement factor.

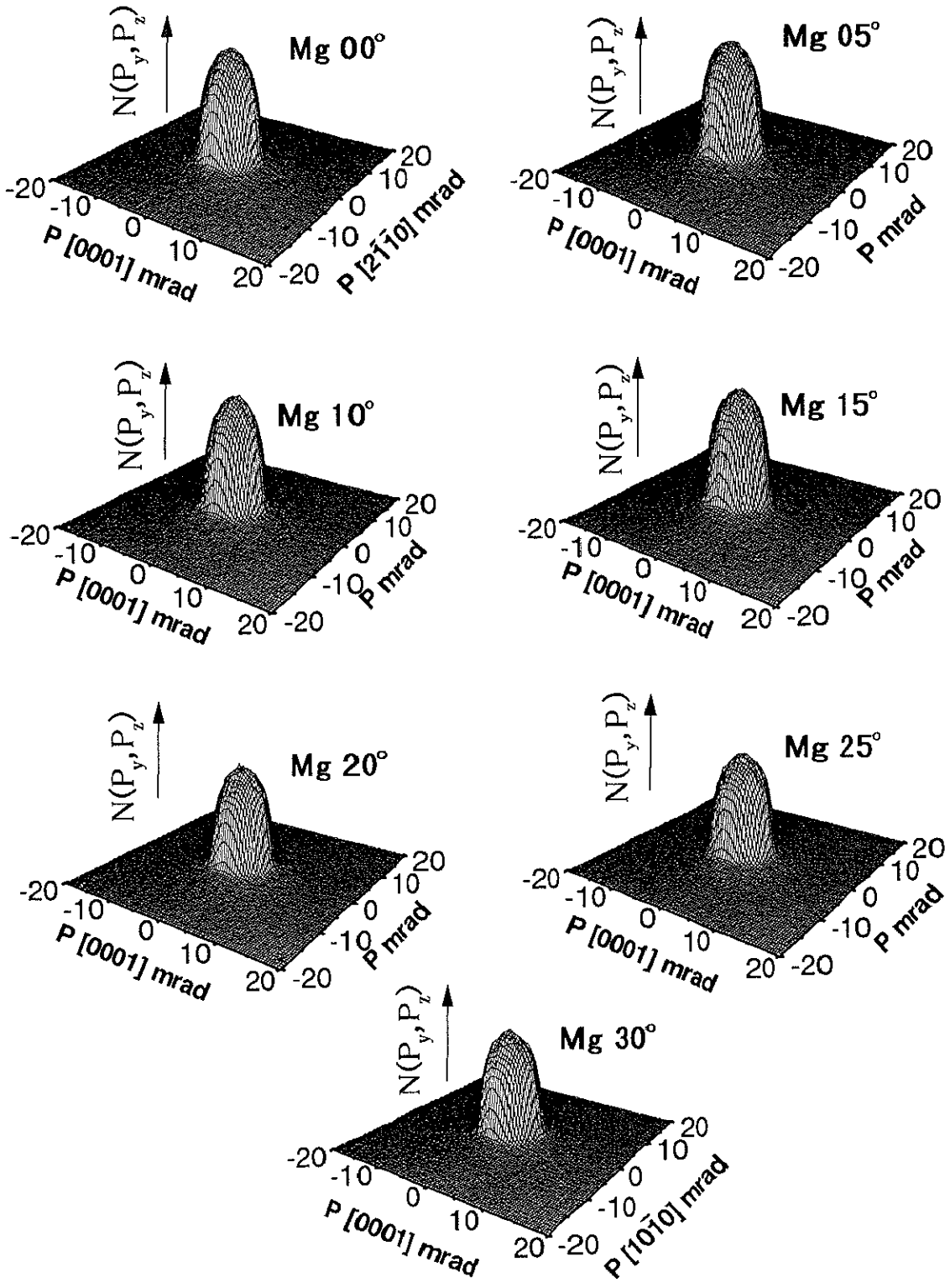


Figure 4.1.2a 2D-ACAR spectra of Mg as a projection of [0001] direction from inclination angles of 0° to 30° as step of 5°. (a) shows the isometric view and (b) shows the contour map respectively.

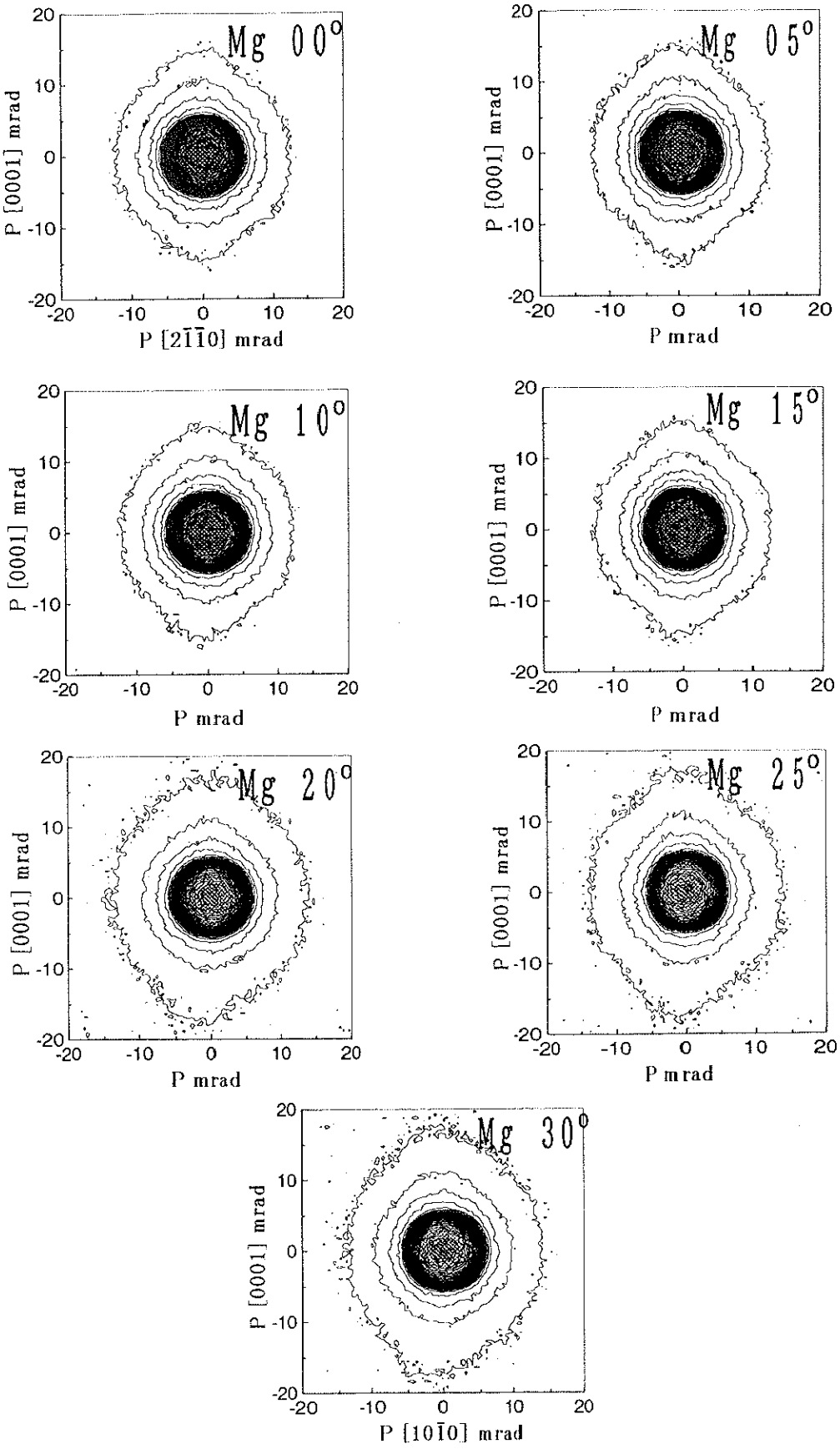
Mg 00°
Mg 05°
Mg 10°
Mg 15°
Mg 20°
Mg 25°
Mg 30°
P [0001] mrad
P [2$\bar{1}\bar{1}$0] mrad
P [10$\bar{1}$0] mrad
P mrad
20
10
0
-10
-20

Figure 4.1.2 b

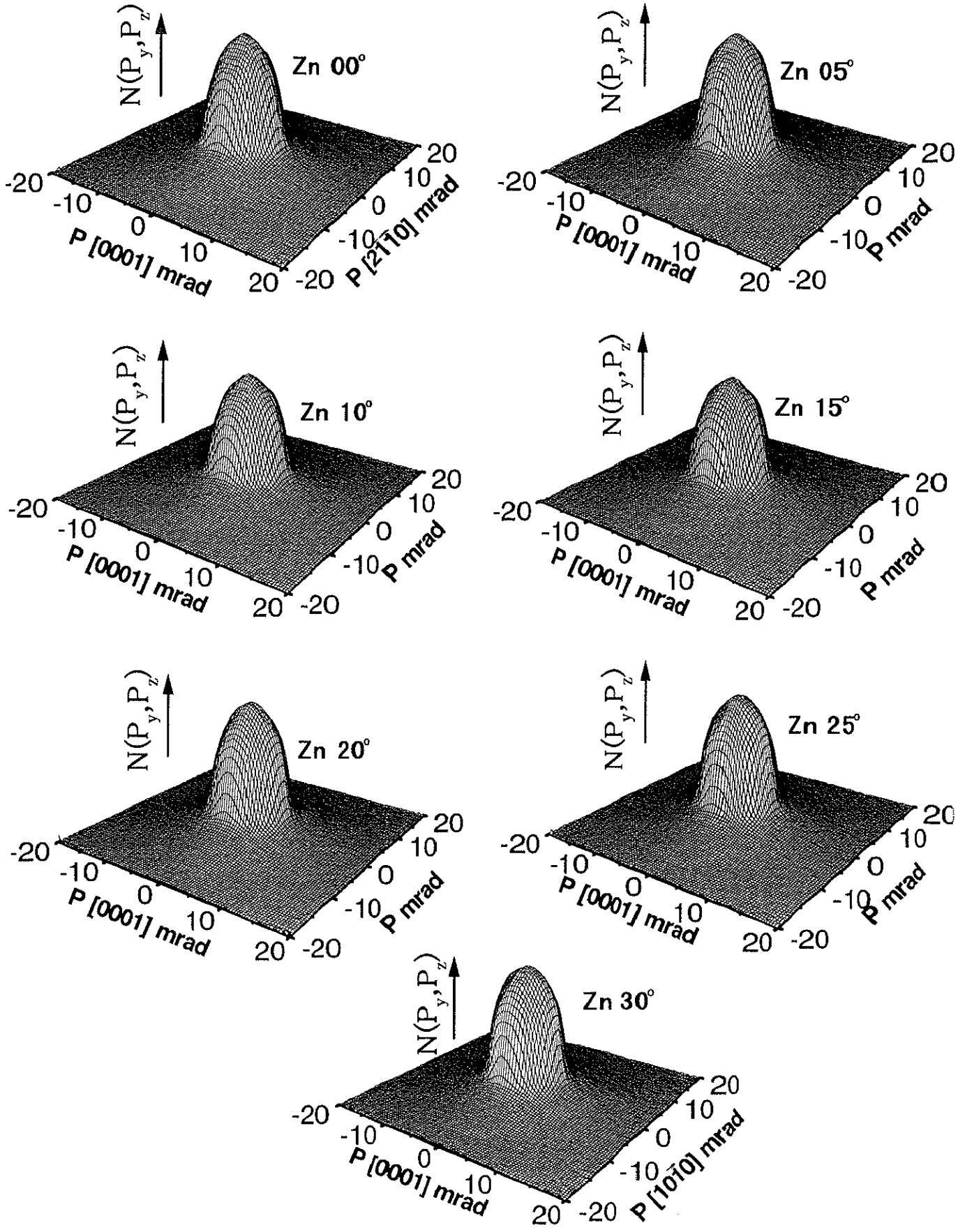


Figure 4.1.3a 2D-ACAR spectra of Zn as a projection of [0001] direction from inclination angles of 0° to 30° as step of 5°. (a) shows the isometric view and (b) shows the contour map respectively.

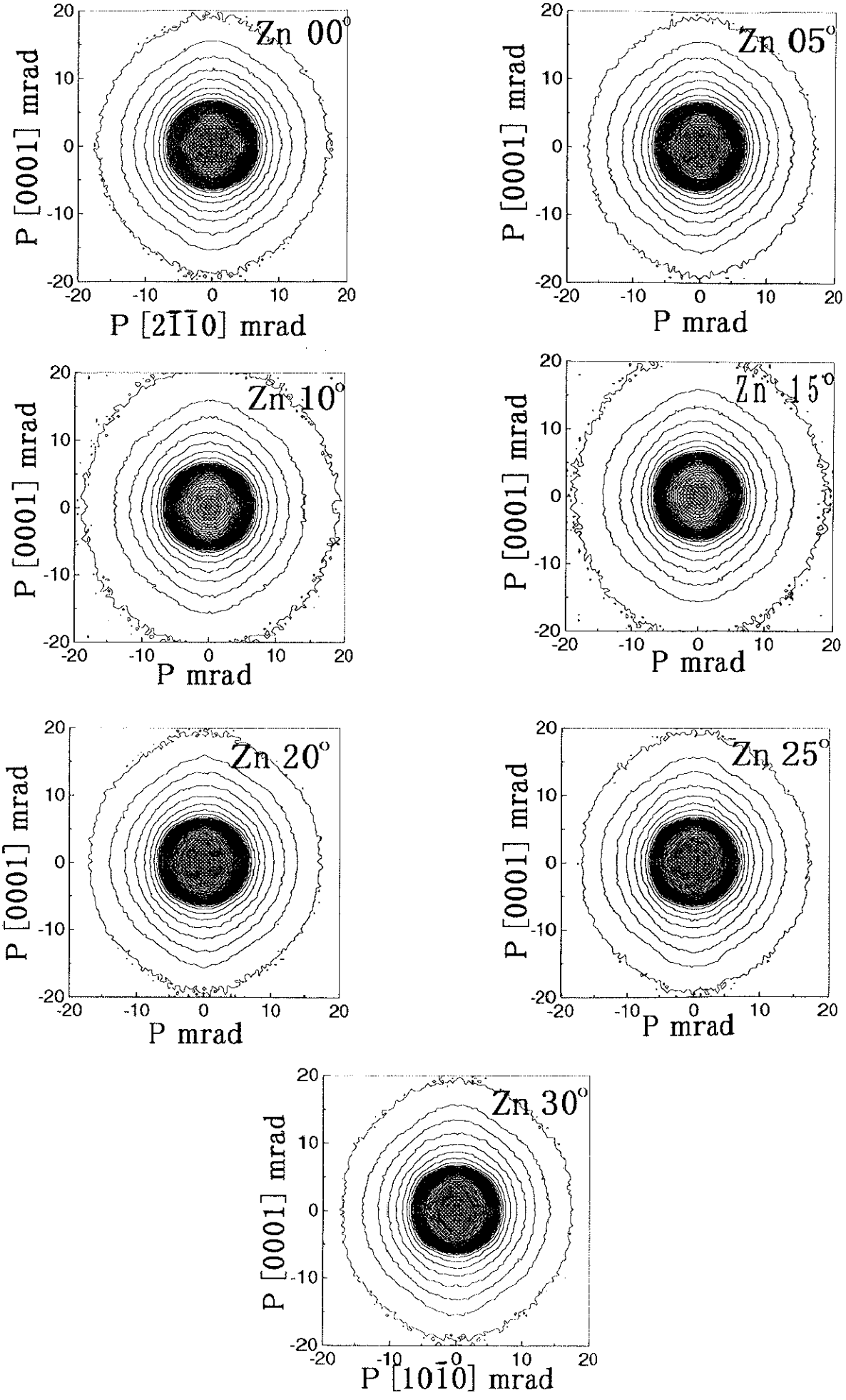
Zn 00°
Zn 05°
Zn 10°
Zn 15°
Zn 20°
Zn 25°
Zn 30°
P [0001] mrad
P [2$\bar{1}\bar{1}$0] mrad
P mrad
P [10$\bar{1}$0] mrad
20
10
0
-10
-20

Figure 4.1.3 b

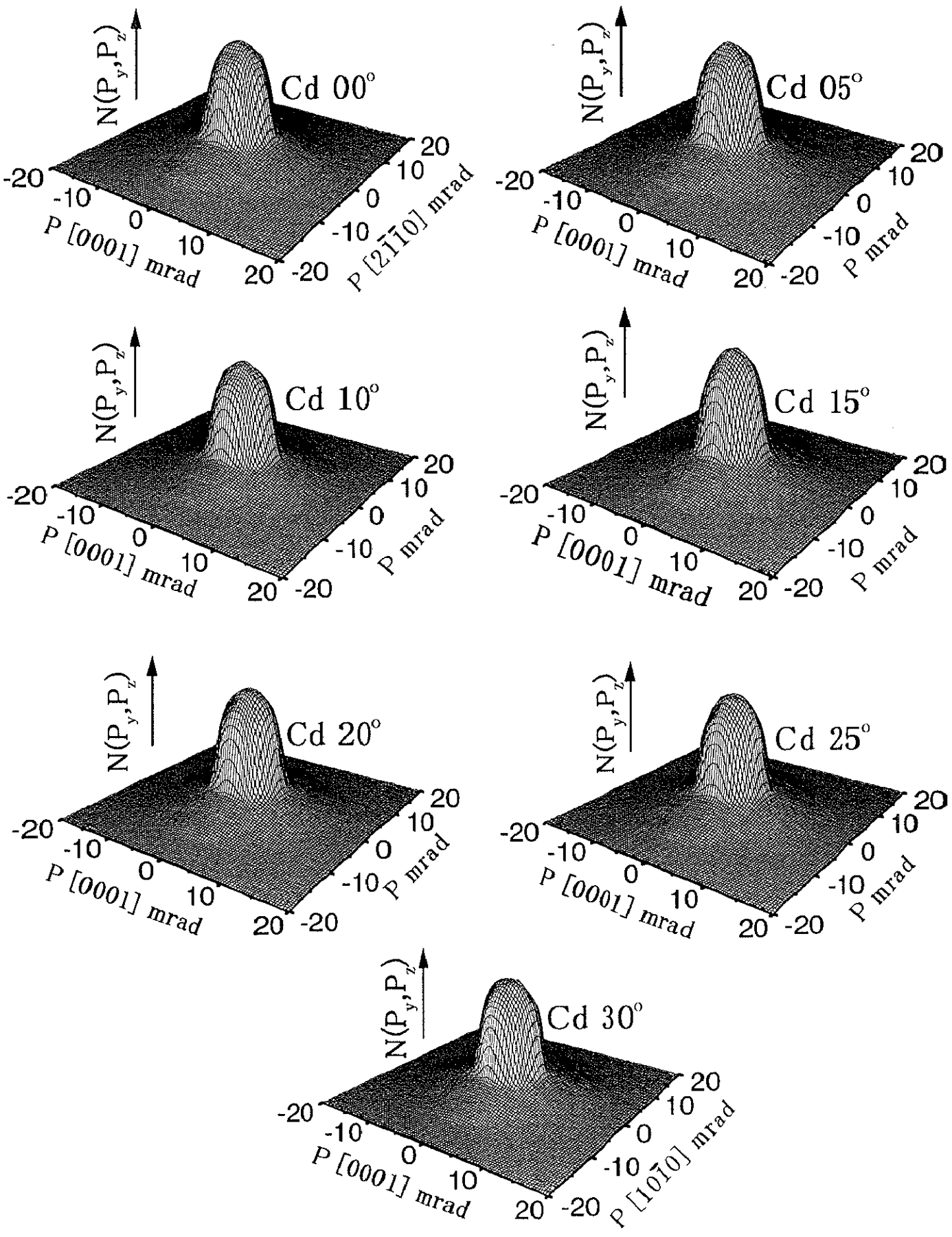


Figure 4.1.4a 2D-ACAR spectra of Cd as a projection of [0001] direction from inclination angles of 0° to 30° as step of 5°. (a) shows the isometric view and (b) shows the contour map respectively.

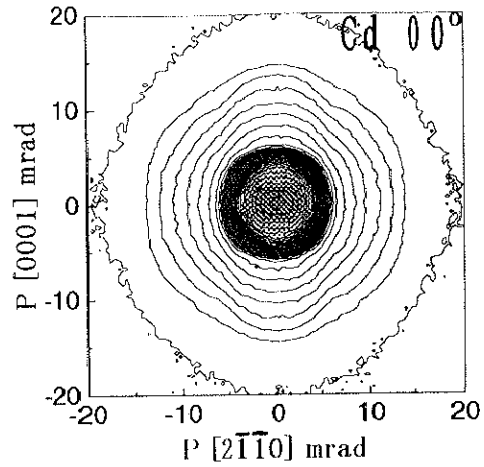
Cd 00°
P [0001] mrad
P [2$\bar{1}\bar{1}$0] mrad

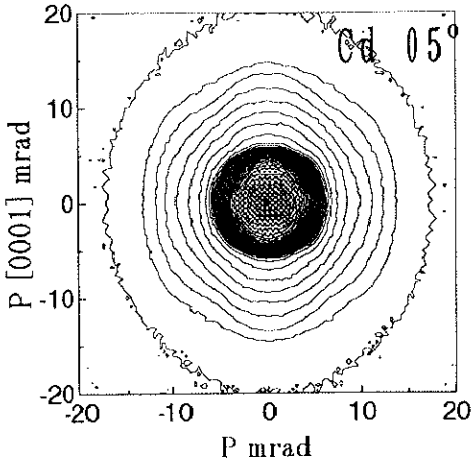
Cd 05°
P [0001] mrad
P mrad

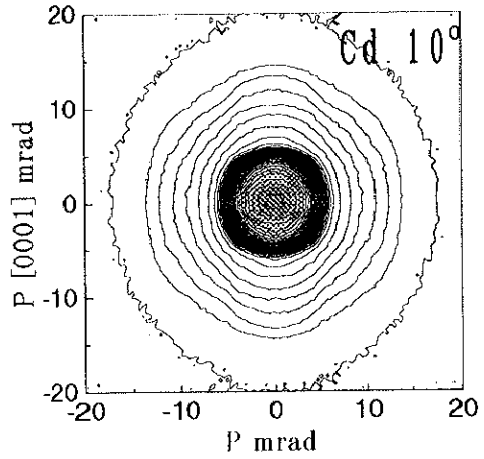
Cd 10°
P [0001] mrad
P mrad

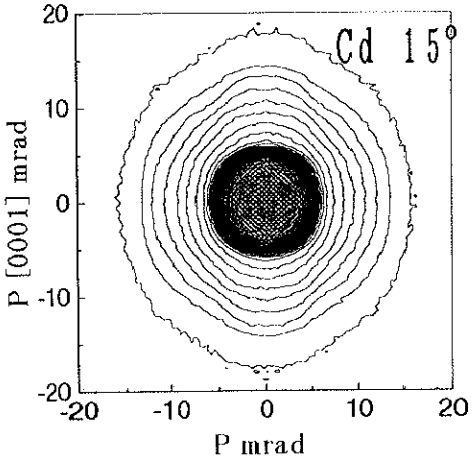
Cd 15°
P [0001] mrad
P mrad

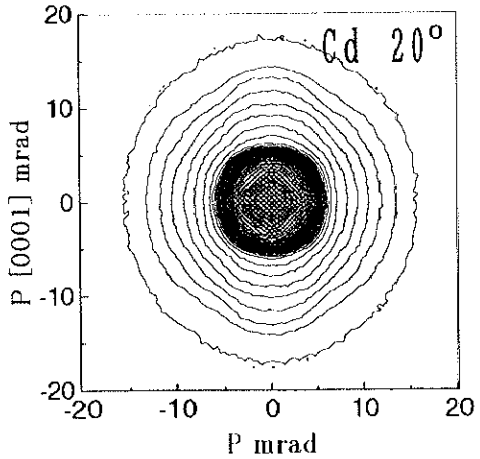
Cd 20°
P [0001] mrad
P mrad

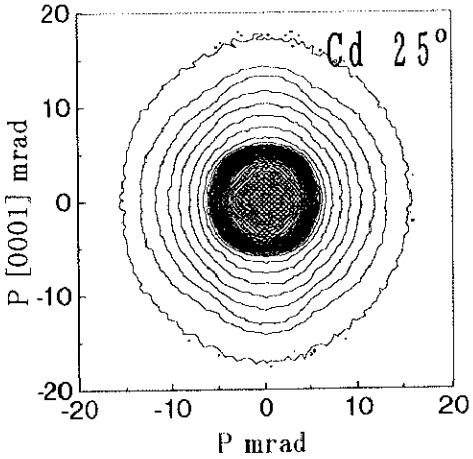
Cd 25°
P [0001] mrad
P mrad

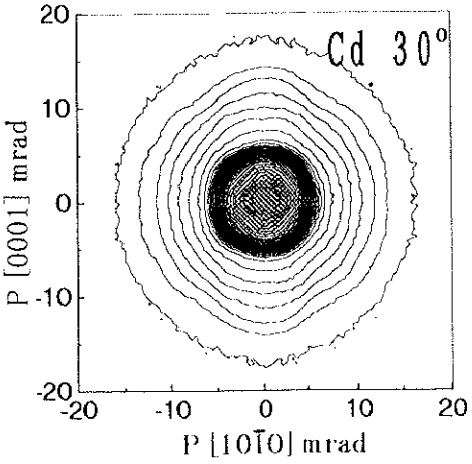
Cd 30°
P [0001] mrad
P [10$\bar{1}$0] mrad

Figure 4.1.4 b

In order to follow the HMC's, we enlarged the spectra, then cut up to 10% from their maxima. Figures 4.1.8, 4.1.9 and 4.1.10 represent the enlarged spectra in ΓMK, ALM and AHK planes for Mg, Zn and Cd, respectively. The dark points in the Figure show the reciprocal lattice point's positions. From these Figures the nearest neighbor reciprocal lattice points, $G_{111}$, in Mg are located at $P_{\Gamma M}$=7.6, $P_{\Gamma K}$=8.8 and $P_{\Gamma A}$ =4.7 mrad. The nearest neighbor reciprocal lattice points in Zn are located at $P_{\Gamma M}$=9.2, $P_{\Gamma K}$=10.6 and $P_{\Gamma A}$ =5.0 mrad. The nearest neighbor reciprocal lattice points in Cd are located at $P_{\Gamma M}$=8.2, $P_{\Gamma K}$=9.4 and $P_{\Gamma A}$ =4.4 mrad. It is noticed that, these values are far from Fermi momentum $P_F$ of Mg (5.308 mrad), Zn (6.187 mrad) and Cd (5.449 mrad). As a result, the contribution to the Fermi surface is mainly due to $G_o$ (G=0), and the Fermi surface feature in the first Brillouin zone will be the strongest and the Fermi surface feature in the higher zone is weak (see subsection II.3 page 16).

In view of electron gas calculations, the electron momentum density increases as P approaches the Fermi momentum $P_F$. The enhanced contribution are observed in upper parts of the spectra of Mg, Zn and Cd. Figure 4.1.11 represents the electron momentum density in ΓM, ΓK and ΓA directions for Mg, Zn and Cd, respectively, with that obtained using Kahana-like enhancement formula (2.5.2). The enhancement parameters are obtained from statistical analysis using least square method (SALS). Table 4.1.1 declares the obtained (b/a) factor in ΓM, ΓK and ΓA directions for Mg, Zn and Cd, respectively. It is obvious that the enhancement (b/a) factor is closed to that of the values obtained by Kahana[2.5.1] for Mg in ΓM and ΓK directions. The fitted enhancement factor (b/a) is smaller than the theory in ΓM and ΓK directions for Zn, and it is larger than it for Cd in ΓM and ΓK directions. It is also clear that the gradient of the fitted curve increases as the atomic number of the used element increases. This shows that Mg is very closed to free electron model, while the enhanced contribution increases as going from Zn to Cd.

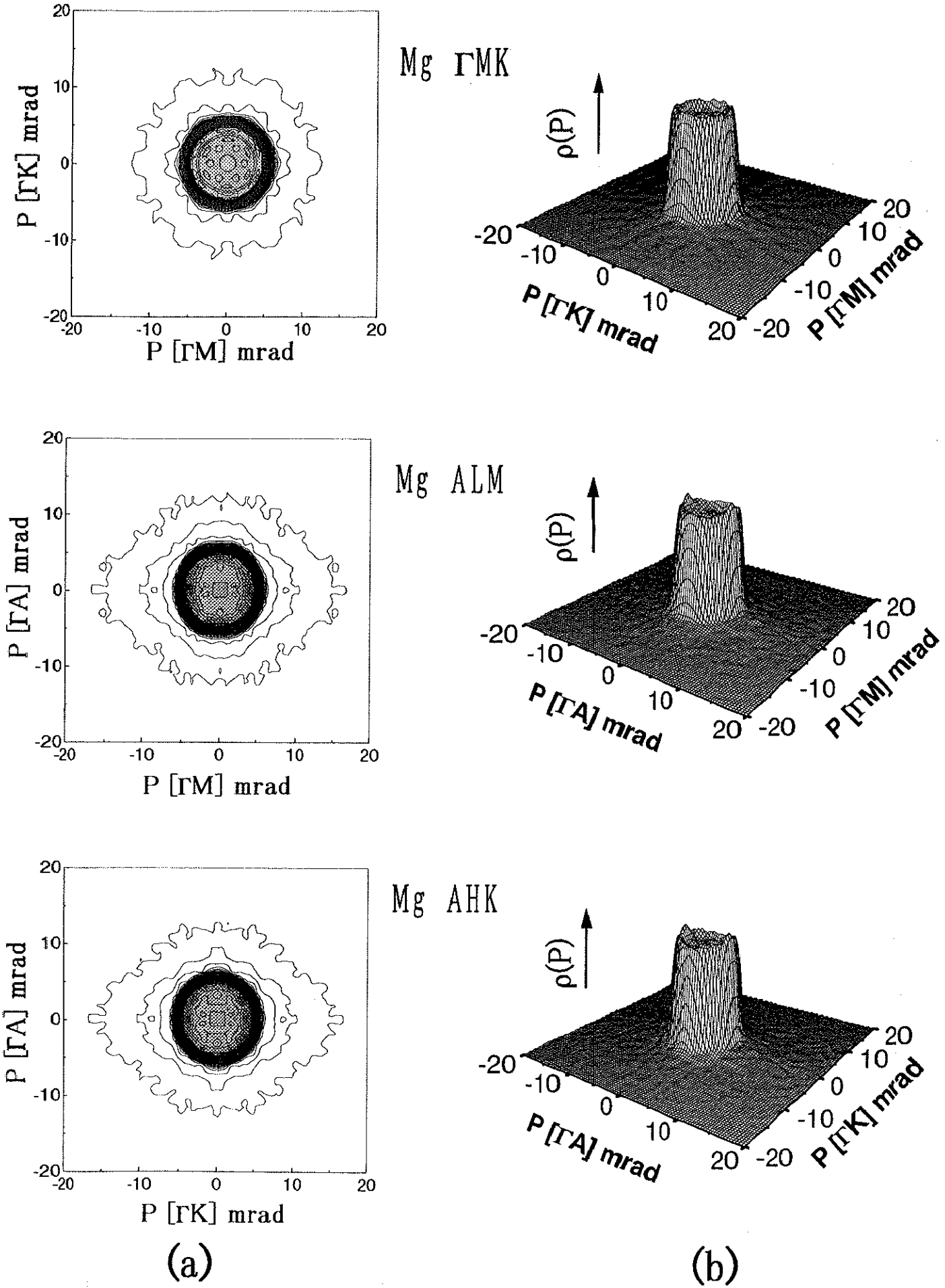


Figure 4.1.5 the electron density in the momentum space ρ(P) of Mg in ΓMK, ALM and AHK plane,respectively, as (a) contour maps and (b) isometric view.

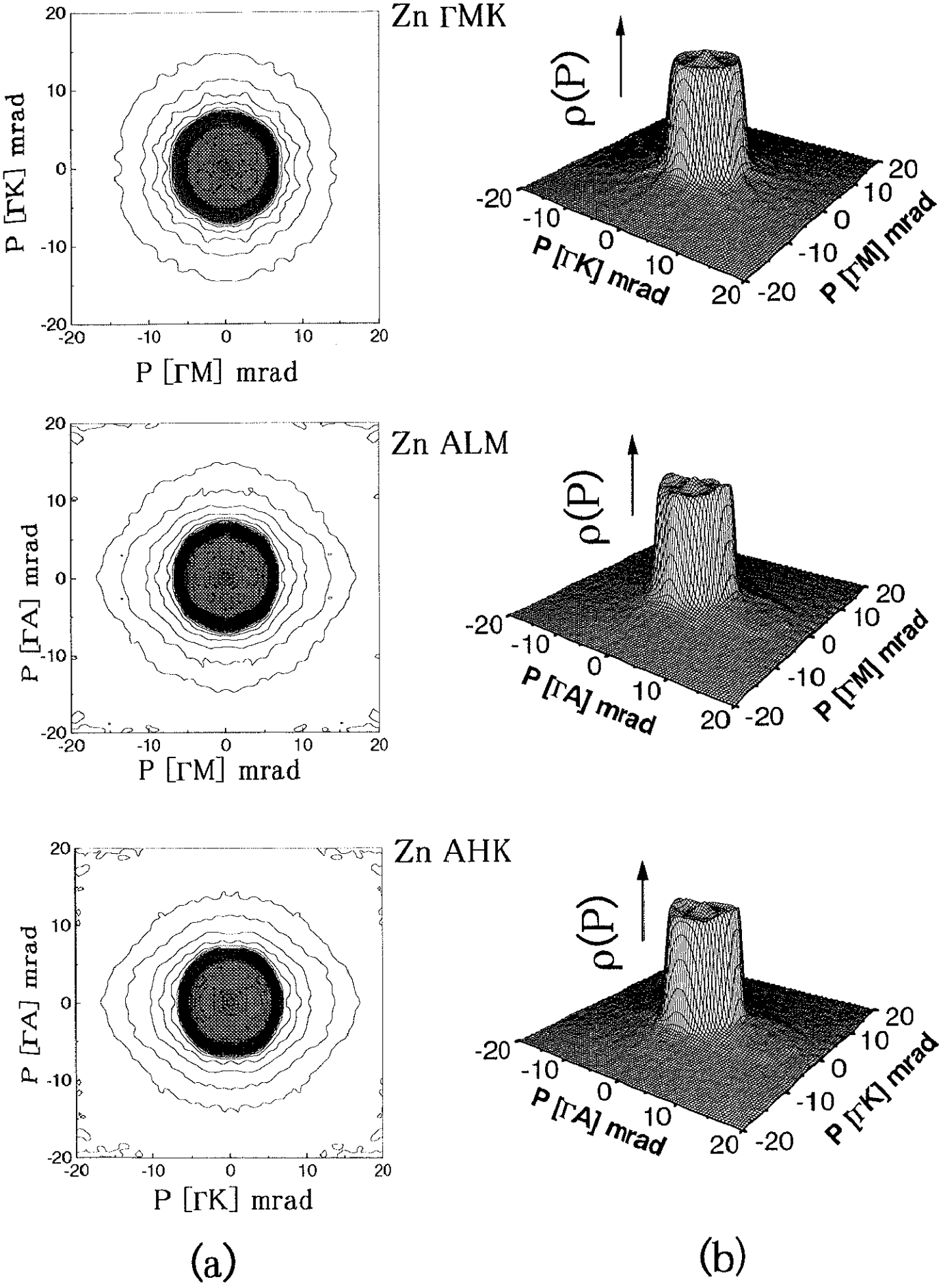


Figure 4.1.6 the electron density in the momentum space ρ(P) of Zn in ΓMK, ALM and AHK plane,respectively, as (a) contour maps and (b) isometric view.

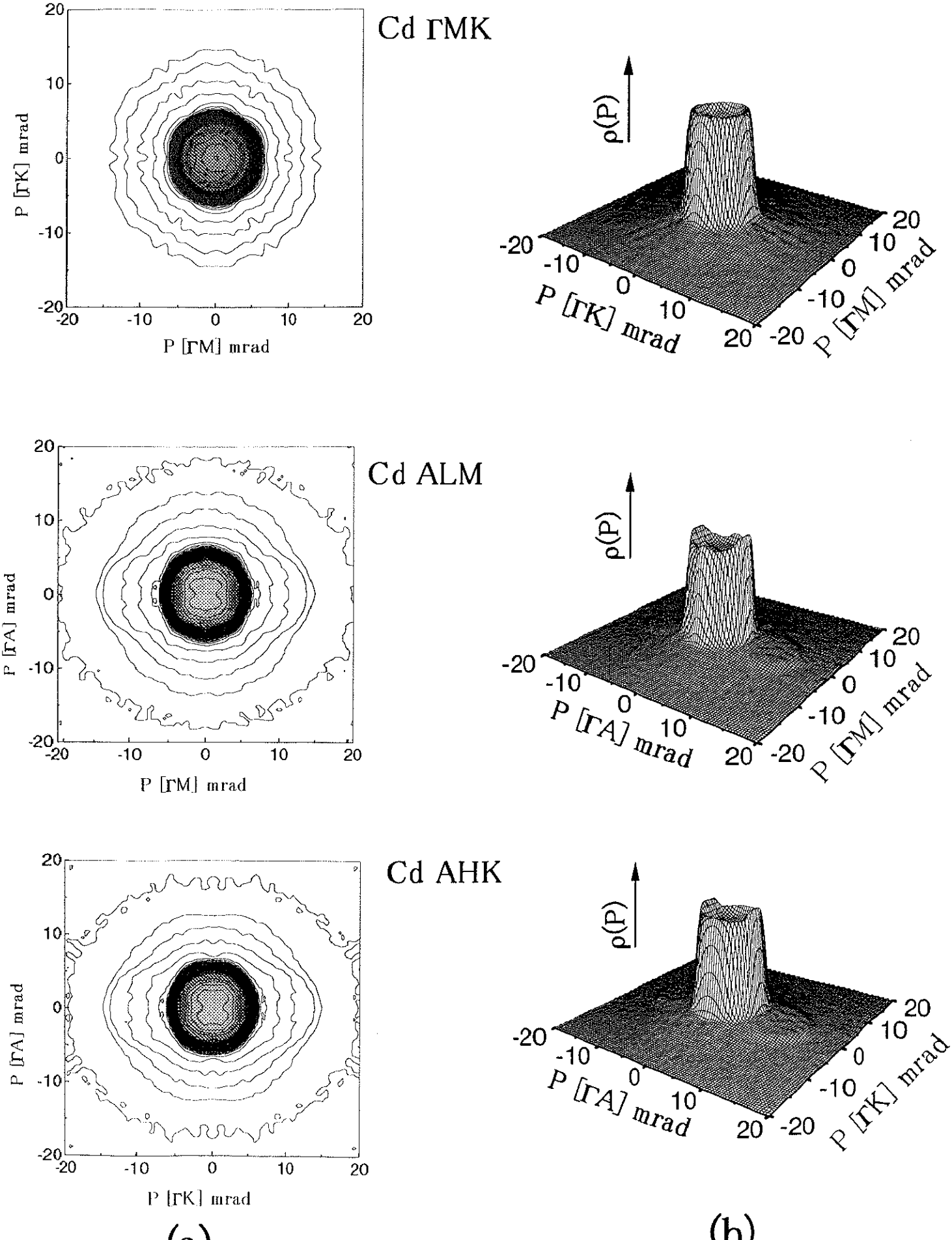


Figure 4.1.7 the electron density in the momentum space ρ(P) of Cd in ΓMK, ALM and AHK plane,respectively, as (a) contour maps and (b) isometric view.

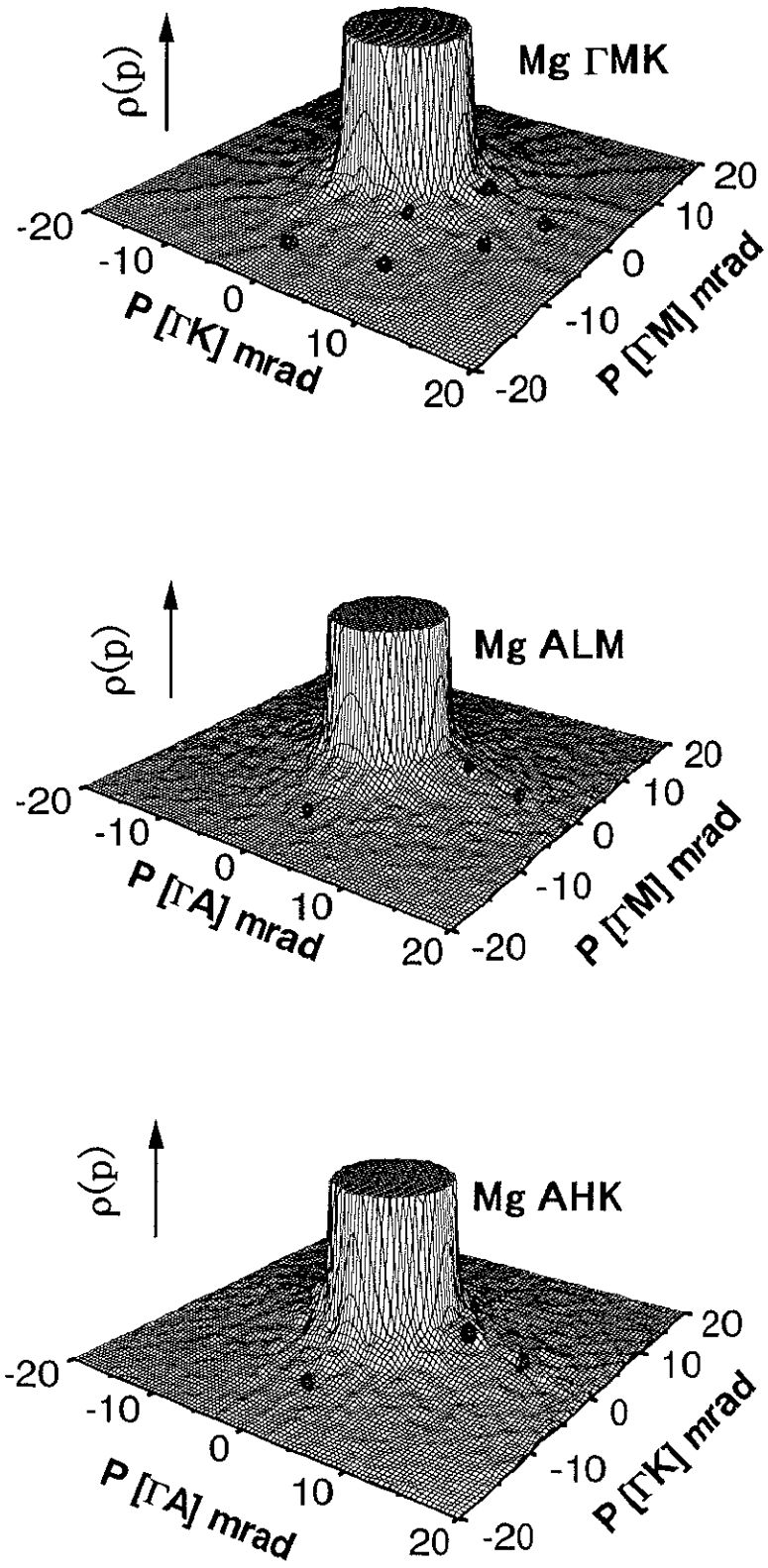


Figure 4.1.8 the enlarged ρ(P) spectra of Mg up to 10% from their maxima in ΓMK, ALM and AHK plane, respectively. the dark circles show the reciprocal lattice points.

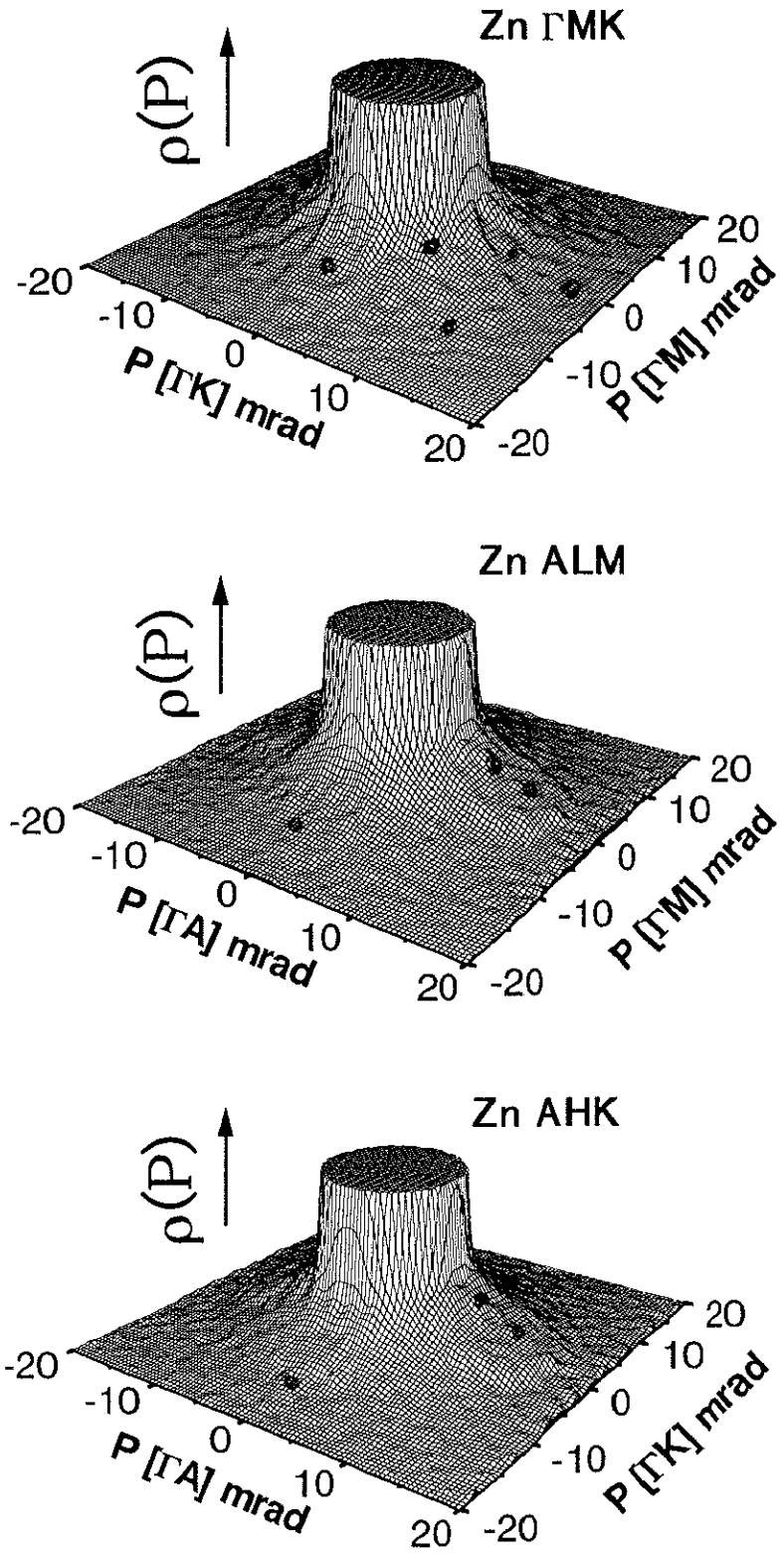


Figure 4.1.9 the enlarged ρ(P) spectra of Zn up to 10% from their maxima in ΓMK, ALM and AHK plane, respectively. the dark circles show the reciprocal lattice points.

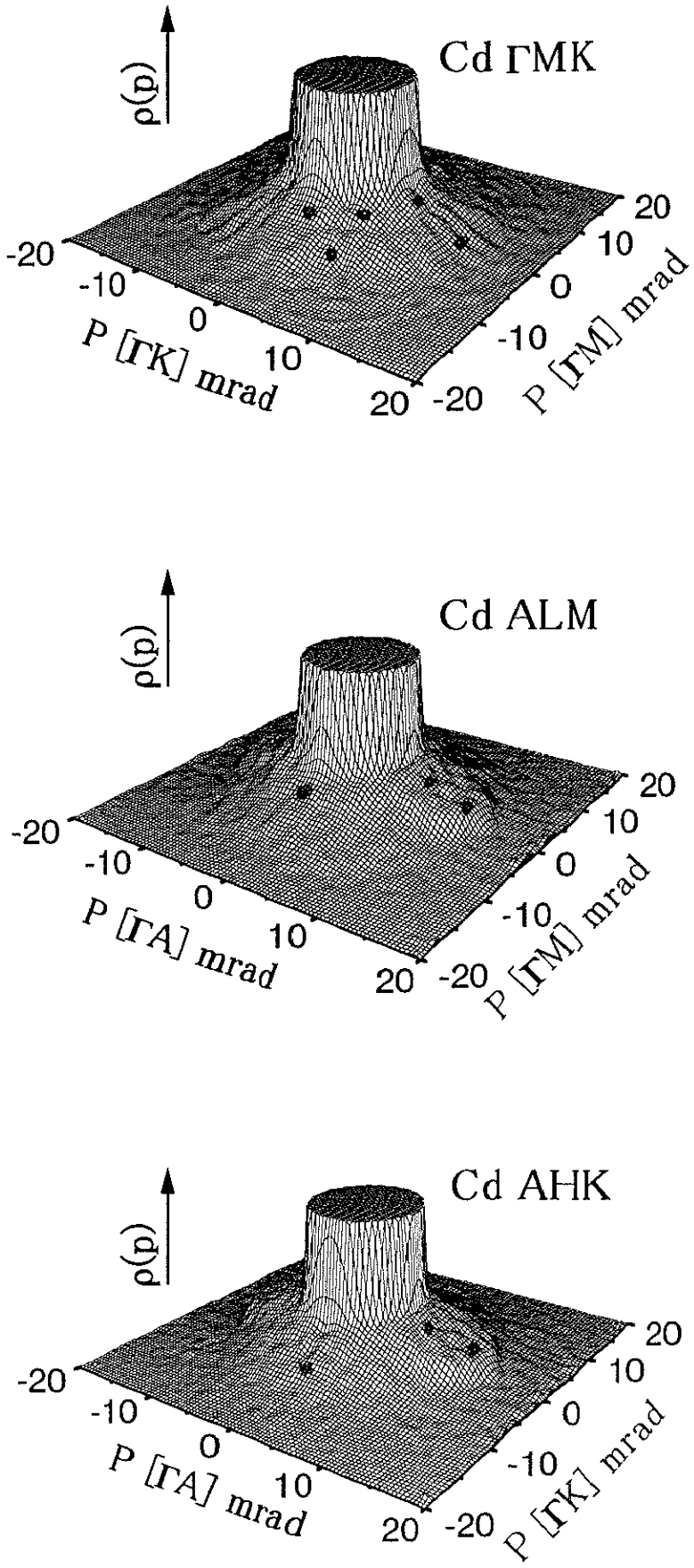


Figure 4.1.10 the enlarged ρ(P) spectra of Cd up to 10% from their maxima in ΓMK, ALM and AHK plane, respectively. the dark circles show the reciprocal lattice points.

The above mentioned enhancement effect can be explained through the many body effects. Due to the electron positron attraction, an electronic charge screening the positron is formed. As a result, an additional electron positron correlation potential is formed. It is mainly due to the work done to bring the positron to its position against the coulomb forces between the positron and the electronic polarization cloud. Furthermore, in the atomic system there are some electrons in state $k_F$ in Fermi sea, scattered to a new state above Fermi level. According to Pauli exclusion principal, the electrons must easily scattered are those in a state close to $k_F$. The above mentioned positron screening cloud in such system is built up by scattering of the states close to Fermi surface. This scattering pulls the positron and particular electron-like excitation into a stronger correlation.

Fermi surface boundaries are determined from the locus of $|\nabla\rho(P)|_{Max}$. Figure 4.1.12 shows experimental Fermi radii along ΓMK, ALM and AHK planes normalized to the free electron Fermi radius of individual metals, respectively. The free electron Fermi radii of Mg, Zn and Cd are taken as a unity. In ΓMK and ALM planes the angle is measured from ΓM direction, while in AHK plane it is measured from ΓK direction. In ΓMK plane the maximum deviations from the free electron Fermi radius for Mg, Zn and Cd are hesitating around ±1.5% about 0.01 a.u.. In ALM plane the maximum deviations from free electron Fermi radius is hesitating around ±2% about 0.02 a.u.. In AHK plane the maximum deviations from free electron Fermi radius for Mg at ΓA direction is -1.0% (about 0.005 a.u.), for Zn at ΓH direction is -3.0% (about 0.022 a.u.) and for Cd at ΓH direction is -4.0% (about 0.028 a.u.). From these figures it can be noted that all the Fermi radii of the examined metals are varied around free electron ones within error estimation.

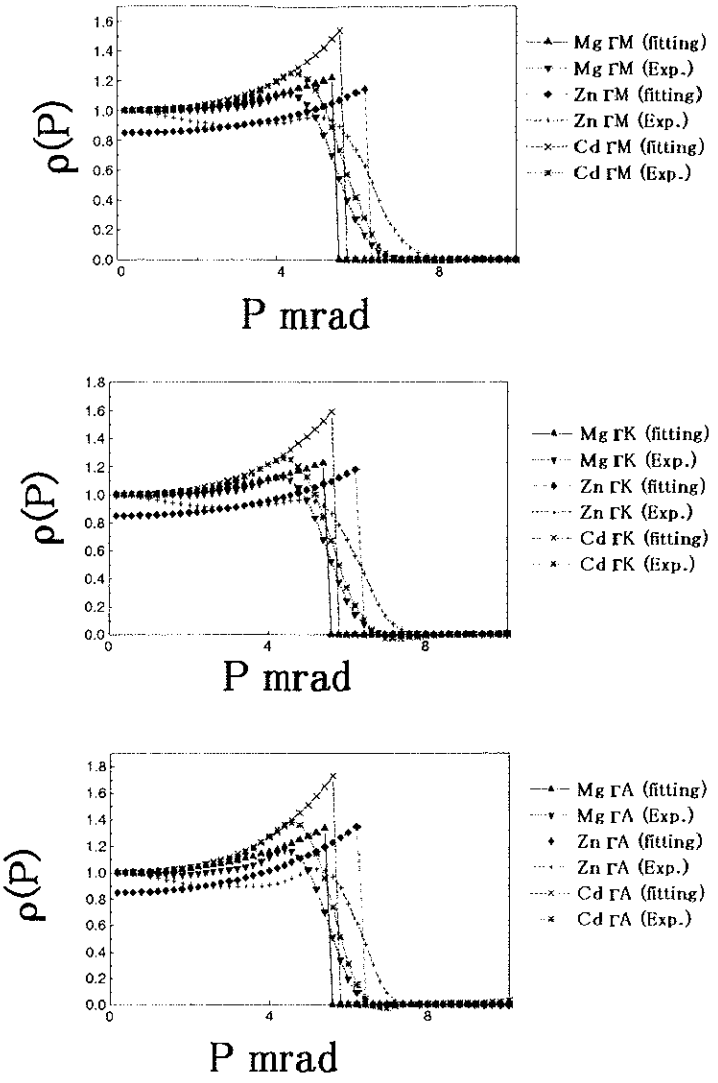


Figure 4.1.11 the electron momentum density of (a) Mg, (b) Zn and (c) Cd in ΓM, ΓK and ΓA directions, respectively, with that fitted using the Kahana enhancement equation (2.5.2)

**Table 4.1.1 the enhancement factor b/a of Mg, Zn and Cd with that obtained by Kahana[2.5.1].**

| | Mg | Zn | Cd |
|---|---|---|---|
| ΓM | 0.18 | 0.12 | 0.20 |
| ΓK | 0.18 | 0.13 | 0.25 |
| ΓA | 0.27 | 0.20 | 0.33 |
| Kahan [2.5.1] | 0.20 | 0.19 | 0.20 |

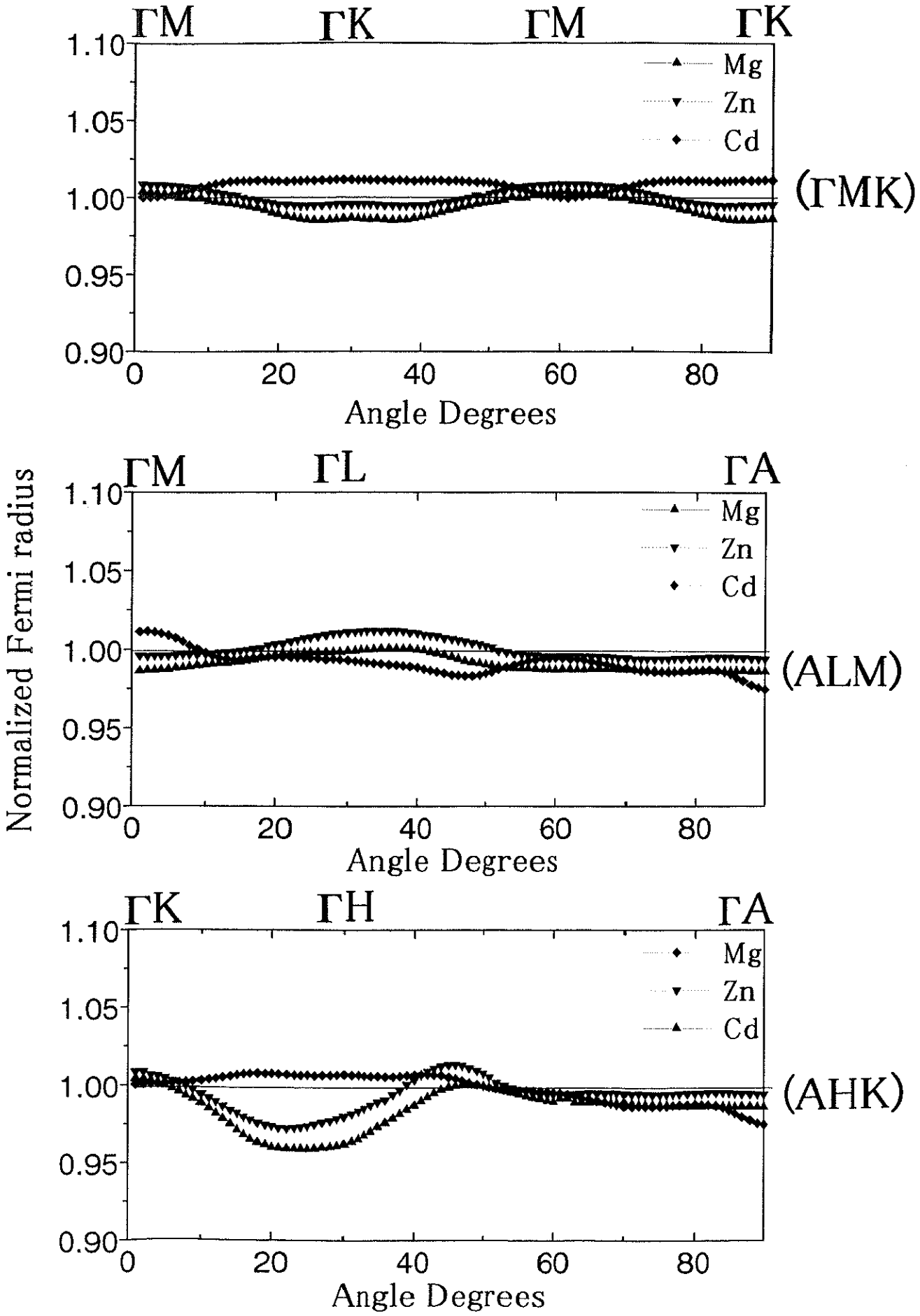


Figure 4.1.12 the normalized Fermi radius of Mg, Zn and Cd in the three main planes ΓMK, ALM and AHK, respectively

### IV.1.2 Electron density in the wave vector space n(k)

The full three-electron density ρ(P) in P-space was reduced to the electron density in wave vector space k-space n(k) using LCW folding procedure (equation (2.4.1)). Figures 4.1.13, 4.1.14 and 4.1.15 represent the intersection of Fermi surface with different symmetry plane in the 1st Brillouin zone, for Mg, Zn and Cd, respectively. Figures that denoted as (a) show the present results, and that denoted as (b) show the results of the band structure using LMTO method [4.1.1]. Figure 4.1.13a shows two electron surfaces at Γ and at L points. Figure 4.1.13b shows nearly the same features around Γ and L point as electron surfaces. While H and K points show hole and electron surfaces, respectively in Fig. 4.1.13b, they don't show any Fermi surface features in Fig. 4.1.13a. For Zn, Figs. 4.1.14a and b show the same feature of the electron surface at Γ point and at L point and a hole surface at H point. In the present result, K point shows an electron surface while it is not observed in Figure 4.1.14b. For Cd, Fig. 4.1.15a and b show electron surface at Γ point and hole surface around H point. The present results show an electron surface at L point contradicting that obtained in 4.1.15b. However, The current results of Mg, Zn and Cd contradict the theoretical calculation using the LMTO method, in the following points. The first is the absence of both the hole surface at H point and the electron surface at K point from the Fermi surface of Mg. The second is the existence of the electron surface at K point in the Fermi surface of Zn. And the third is the existence of the electron surface at L point in Fermi surface of Cd.

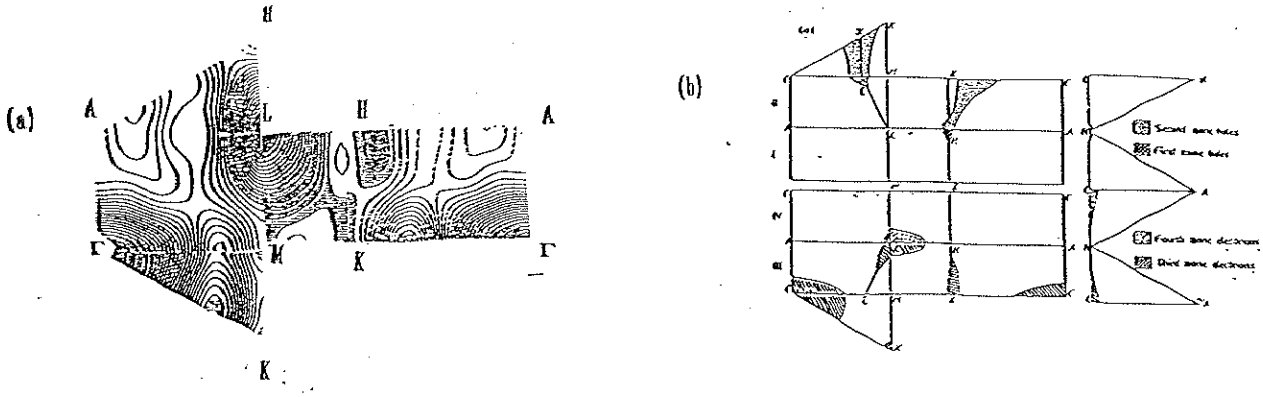


Figure 4.1.13 the intersection of the Fermi surface with different symmetry planes of Brillouin zone of Mg (a) from the present experimental results and (b) from the band structure calculation using LMTO method [4.1.1]

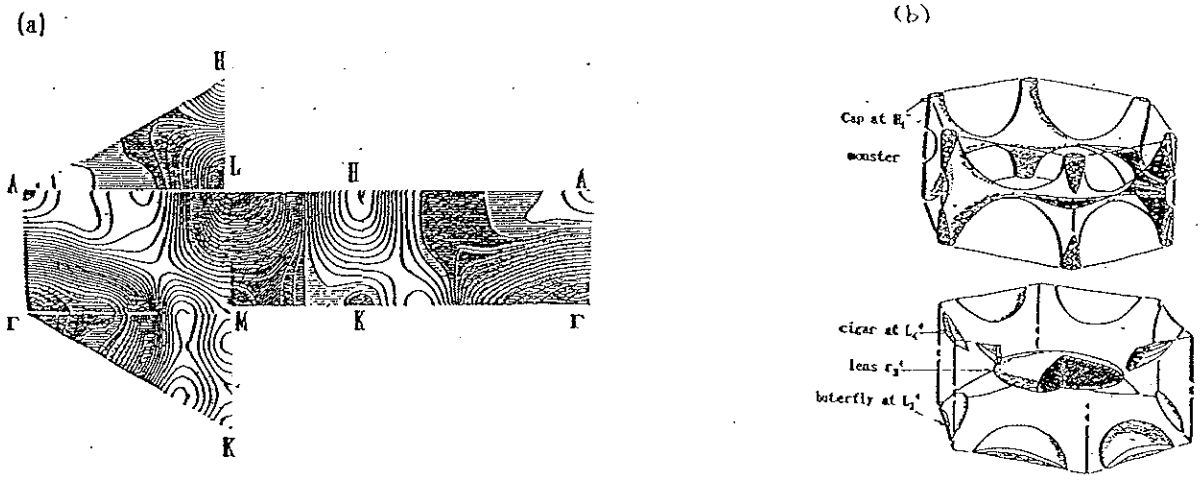


Figure 4.1.14 the intersection of the Fermi surface with different symmetry planes of Brillouin zone of Zn (a) from the present experimental results and (b) from the band structure calculation using LMTO method [4.1.1]

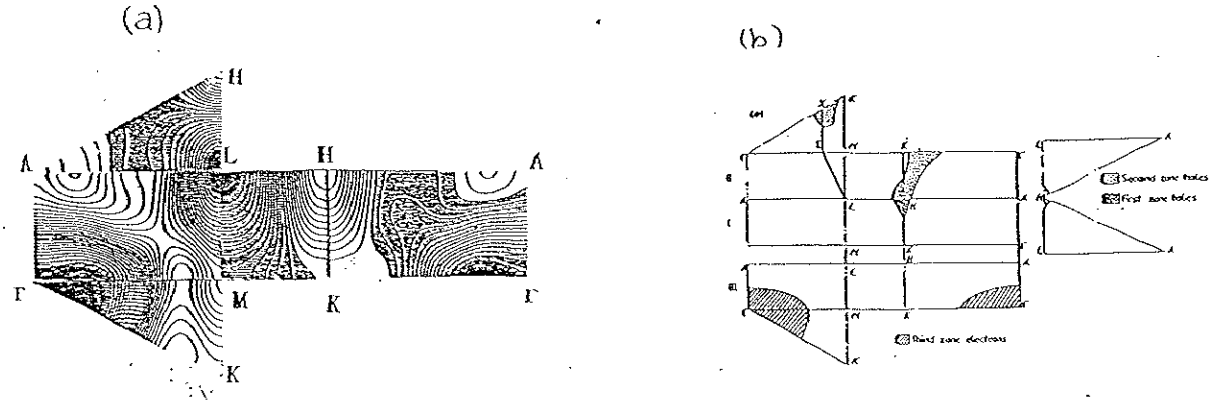


Figure 4.1.15 the intersection of the Fermi surface with different symmetry planes of Brillouin zone of Cd (a) from the present experimental results and (b) from the band structure calculation using LMTO method [4.1.1]

The band number of the above mentioned surfaces can be calculated by normalizing n(k) to the total momentum density, along different principal symmetric lines (equation (2.4.4)). The thickness between the horizontal lines in different bands is derived from statistical analysis using least square method SALS (equation (2.4.5)). The experimental values of n(k) are the sum of the filled bands to the i th band. Figure 4.1.16 represents the normalized electron momentum density in reduced zone scheme in various symmetry directions for (a) Mg, (b) Zn and (c) Cd, respectively. The vertical and the horizontal lines represent Fermi surface edges and band number, respectively. The sharp lines are quoted from the results of band structure calculations using APW method. Using Least square method we could estimate the bands' occupation. Table 4.1.2 shows the estimated values of the bands using least square method. The dimensions of Fermi sheets from LMTO and APW methods are used as input parameters. From Fig.4.1.16, it is obvious that the existence of electron surface (lens) at Γ point for Mg, Zn and Cd agrees with APW method. The hole surface at 1$^{st}$ band around H point, for Mg, is not observed in present results. For Zn, the needles are observed, but its band not exceeds 3$^{rd}$ band. Therefore, we did not consider the existence of the needles in the present results of Zn. The 3$^{rd}$ and the 4$^{th}$ band electron surfaces around L point are observed in the present result and in APW methods. The present results of Cd show good agreement with that obtained using APW method. From these figures we can conclude that Fermi surface of Mg is consisting of, 2$^{nd}$ band hole surface (monster), 3$^{rd}$ band electron surface centered on Γ (lens), 3$^{rd}$ band electron surface centered on L point ( butterfly), and 4$^{th}$ band electron surface centered on L point (cigar). Neither the 1$^{st}$ band hole surface centered on H point (cap) nor the electron surface centered on K point (needles) are seen in the present results of Mg. Fermi surface of Zn is consisting of; 1$^{st}$ band hole surface at H point (cap), 2$^{nd}$ band hole surface (monster), 3$^{rd}$ band electron surface at Γ point (lens) and 3$^{rd}$ and 4$^{th}$ bands electron surfaces at L point (butterfly) and (cigar),respectively. Fermi surface of Cd consists of; 1$^{st}$ band hole crossed to Fermi level near the point H (cap), 2$^{nd}$ band hole (monster),3$^{rd}$ band electron centered on Γ point (lens), and 3$^{rd}$ and 4$^{th}$ bands electron surfaces centered on L point (butterfly) and (cigar),respectively. The 3$^{rd}$

band electron surface centered on K point (needles) hasn't been observed in the present experiment and in niether APW method nor free electron model. The maximum in the gradient of the momentum density $|\nabla n(k)|_{Max}$ (equation (2.4.6)) is used to calculate Fermi surface sheets' dimensions. The estimation of the error in determining Fermi surface dimensions is about 0.02 a.u.. Table 4.1.3 shows the Fermi surface dimensions of 2D-ACAR experimental results with those obtained from the free electron model [4.1.2], references [4.1.7], [4.1.10] and [4.1.1]. For Mg the dimensions of the lens are in good agreement with that of the free electron model. The size of the butterfly is fluctuating around that of the free electron model within the experimental error. The 4$^{th}$ band electron centered on L point (cigar) has dimensions larger than that of the free electron model in LA and LM directions, while it is close to it in LH direction.

| | Mg LMTO | Mg APW | Zn LMTO | Zn APw | Cd LMTO | Cd APW |
|---|---|---|---|---|---|---|
| 1$^{st}$ band $n_1$ | 89.2±1.5 | 91.3±2.1 | 86.4±2.4 | 86.9±2.23 | 86.5±2.3 | 88.4±2.5 |
| 2$^{nd}$ band $n_2$ | 104.6±1.6 | 100.2±1.2 | 100.2±1.14 | 96.6±1.15 | 98.3±1.03 | 94.9±1.1 |
| 3$^{rd}$ band $n_3$ | 121.5±2.1 | 115.0±1.9 | 119.1±1.89 | 116.1±1.5 | 115.1±1.7 | 112.6±1.44 |
| 4$^{th}$ band $n_4$ | 128.5±2.9 | 129.1±2.8 | -- | 121.0±3.01 | -- | 116.3±2.9 |

Table 4.1.2 the obtained fitting parameters using least square-fitting program. LMTO and APW represent the used input dimensions are from the bands from LMTO and APW methods, respectively. The values of the bands are represented with its uncertainty of calculation.

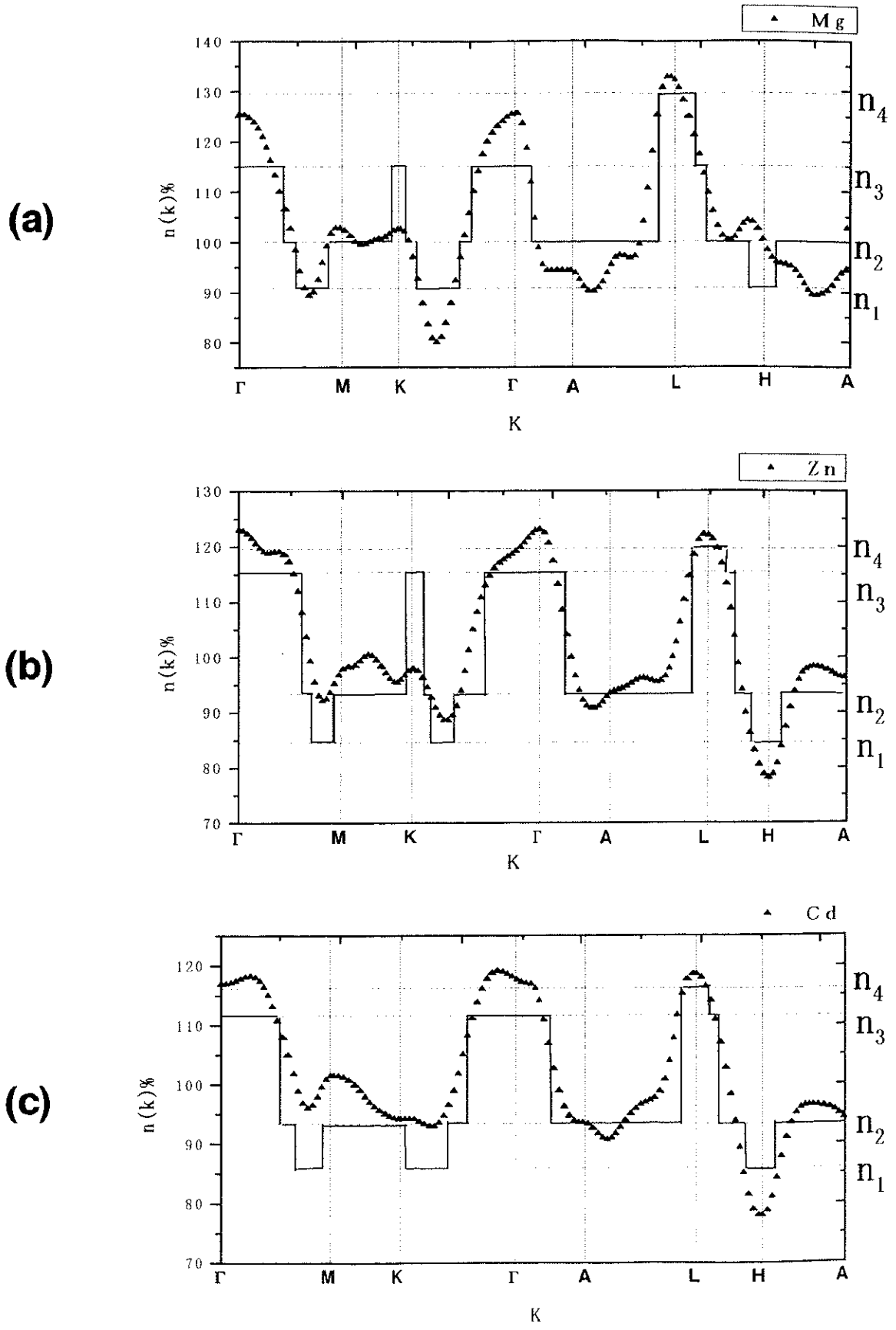


**Figure 4.1.16 the normalized electron density in the wave vector space n(k)% for (a) Mg, (b) Zn and (c) Cd. The sharp lines show the results of the band structure calculation using the APW method.**

| Fermi | Free [4.1.2] | Ref. [4.1.7] | LMTO [4.1.1] | 2D-ACAR | Free [4.1.2] | Ref. [4.1.7] | LMTO [4.1.1] | 2D-ACAR | Free [4.1.2] | Ref. [4.1.10] | LMTO [4.1.1] | 2D-ACAR |
|---|---|---|---|---|---|---|---|---|---|---|---|---|
| Cap ($H_1$) | | | | | | | | | | | | |
| HA | 0.042 | -- | 0.029 | -- | 0.086 | 0.147 | 0.066 | 0.116 | 0..063 | 0.057 | 0.050 | 0.084 |
| HL | 0.096 | -- | 0.039 | -- | 0.162 | 0.146 | 0.099 | 0.196 | 0.153 | 0.094 | 0.078 | 0.162 |
| HK | 0.107 | -- | 0.071 | -- | 0.251 | -- | 0.257 | 0.199 | 0.301 | -- | 0.135 | 0.150 |
| Monster | | | | | | | | | | | | |
| $\sum L$ | 0.112 | 0.064 | 0.063 | 0..049 | 0.123 | -- | -- | 0.066 | 0.111 | -- | -- | -- |
| $\Gamma M_{in}$ | 0.341 | 0.370 | 0.369 | 0.386 | 0.485 | 0.543 | $<L\sum$ | 0.499 | 0.442 | 0.590 | -- | 0.500 |
| $\Gamma_{Mout}$ | 0.341 | 0.370 | 0.369 | 0.363 | 0.485 | 0.518 | 0.531 | 0.527 | 0.442 | 0.102 | 0.516 | -- |
| $\Gamma K_{in}$ | 0.477 | 0.476 | 0.469 | 0.483 | 0.605 | -- | $\geq L\sum$ | 0.645 | 0.547 | -- | 0.710 | 0.500 |
| $\Gamma K_{out}$ | 0.634 | 0.622 | 0.621 | 0.598 | 0.824 | 0.819 | 0.822 | 0.714 | 0.747 | 0.486 | 0.050 | -- |
| HA | 0.142 | -- | 0.029 | -- | 0.068 | 0.057 | 0.066 | 0.116 | 0.063 | -- | 0.078 | 0.07 |
| HL | 0.096 | -- | 0.039 | -- | 0.162 | 0.151 | 0.099 | 0.196 | 0.153 | -- | | 0.130 |
| Needles ($K_3^+$) | | | | | | | | | | | | |
| $K\Gamma$ | 0.061 | 0.067 | 0.062 | -- | 0.10 | -- | -- | -- | -- | -- | -- | -- |
| KM | 0.032 | 0.033 | 0.036 | -- | 0.005 | -- | -- | -- | -- | -- | -- | -- |
| Butterfly $L_3^+$ | | | | | | | | | | | | |
| $L\sum$ | 0.256 | 0.205 | 0.200 | 0.200 | 0.255 | -- | -- | -- | 0.221 | -- | -- | -- |
| LH | 0.252 | 0.184 | 0.200 | 0.170 | 0.255 | -- | -- | -- | 0.221 | -- | -- | -- |
| LM | 0.087 | -- | 0.082 | 0.130 | 0.085 | -- | -- | -- | 0.072 | -- | -- | -- |
| LA | 0.051 | -- | 0.047 | 0.112 | 0.044 | -- | -- | -- | 0.037 | -- | -- | -- |
| Lens($\Gamma_3^+$) | | | | | | | | | | | | |
| $\Gamma A$ | 0.085 | 0.080 | 0.084 | 0.085 | 0.155 | 0.147 | 0.145 | 0.136 | 0.145 | 0.146 | 0.149 | 0.132 |
| $\Gamma M$ | 0.341 | 0.312 | 0.320 | 0.341 | 0.485 | 0.460 | 0.441 | 0.465 | 0.442 | 0.413 | 0.389 | 0.390 |
| $\Gamma K$ | 0.341 | 0.312 | 0.320 | 0.334 | 0.485 | 0.460 | 0.435 | 0.465 | 0.442 | 0.413 | 0.402 | 0.390 |
| Cigar($L_4^+$) | | | | | | | | | | | | |
| LA | 0.051 | -- | 0.047 | 0.085 | 0.044 | -- | -- | 0.112 | 0.037 | -- | -- | 0.124 |
| LM | 0.087 | 0.043 | 0.080 | 0.130 | 0.085 | -- | -- | 0.160 | 0.072 | -- | -- | 0.160 |
| LH | 0.252 | -- | 0.198 | 0.178 | 0.255 | -- | -- | 0.222 | 0.221 | -- | -- | 0.200 |

**Table 4.1.3 the Fermi surface dimensions (in a.u.) in comparison with the free electron model and other results. The error estimation of Fermi surface sheets is 0.02 a.u.**

The missing of the hole surface around H point in Mg (cap) in the present results is attributed to the fact that, the hole region in 1st and 2nd bands are reduced at the expense of the reduction of 3rd and 4th bands electron sheets butterfly and cigar. Therefore, the cap size becomes too small to be detected. For the same reason the needles couldn't be observed in the present experiment. Since their size is smaller than the experimental resolution. For Zn, the size of the cap predicted by free electron model along HA, and HL are (=0.086 and 0.162 a.u.), respectively, and the size of the butterfly predicted by free electron model along LA, and LM are (=0.044 and 0.085 a.u.). They are smaller than experimental values, so that the butterfly shows overlapping with the cigar around L point. The size of the lens along ΓA, ΓM and ΓK are (=0.155, 0.485 and 0.485 a.u.), respectively, and these values are larger than that experimentally determined. Fermi surface dimensions of Cd shows that the size of the lens is smaller than that of the free electron model, and also the size of 1st band hole surface centered on H (cap) is smaller than it along HK direction. The 4th band electron (cigar) is larger than that predicted by free electron model along LA and LM directions. The difference in the dimensions of the Cap and Cigar in Cd is attributed to the fact that, the experimental resolution is larger than the size of the cap along HA (=0.063 a.u.) and of the cigar along LA and LM (=0.037 and 0.072 a.u.), respectively. The butterfly is overlapped with the cigar at L point. Therefore, its dimensions become difficult to be determined. These values are around the experimental resolution, from which it shows a large uncertainty. Generally, as a qualitative and quantitative analysis of Fermi surface sheets of Mg, Zn and Cd, the present results show good agreement with free electron model within the available experimental error.

## IV.2 HCP structure metals of valence three Scandium Sc and Yttrium Y

During the last few years, widespread interests in determining the momentum space density and Fermi surface of transition metal [4.2.1]. The metals of group IIIA, Sc and Y have some interest in which they have full 4s- and 5s- shell, respectively, then d-band start to be occupied by one electron. In contrast with divalent HCP structure metals, there have been relatively small amount of experimental work performed on momentum space density and Fermi surface of Sc [4.2.2] and Y [4.2.3], this is because of the difficulties in obtaining sufficient pure samples. Figure 4.2.1 represents the free electron Fermi surface for trivalent HCP metal of ideal c/a ratio [4.2.4] and the constructed Fermi surface by the band structure calculation using the cellular method for both Sc and Y, respectively.

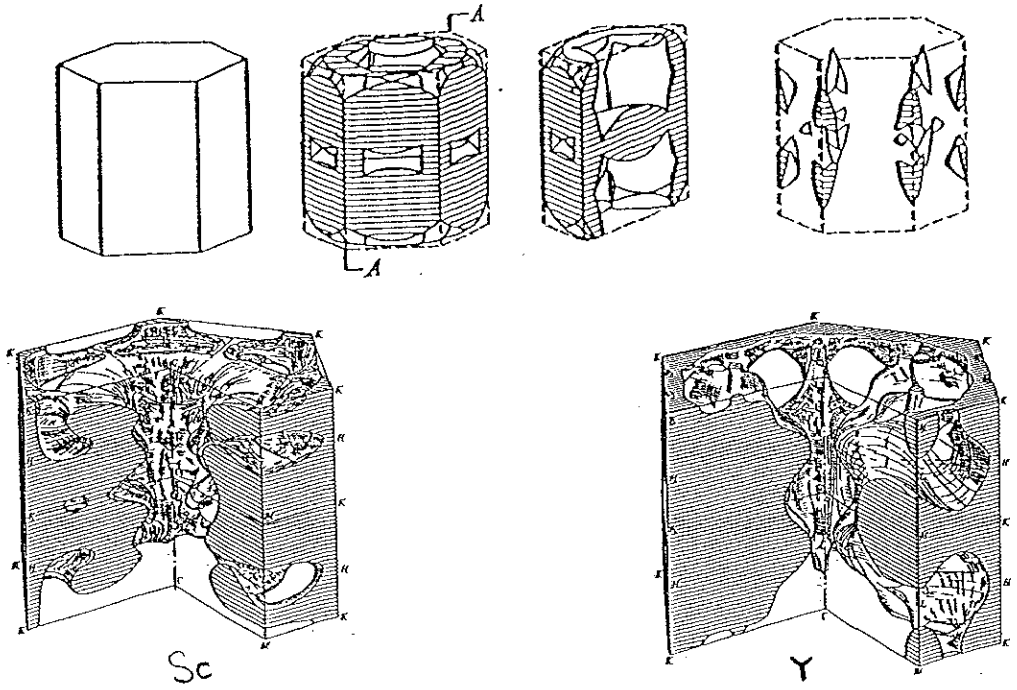


Figure 4.2.1 (a) the free electron Fermi surface of for HCP structure of valence 3. It shows a multiply connected surface in the 3rd and 4th bands and pockets of electrons in the 5th and 6th bands. (b) shows the obtained Fermi surfaces of Sc and Y using cellular method.

Altmann et al [4.2.5] have calculated the Fermi surface of Sc using cellular method. This Fermi surface has a complicated multiply connected structure in the 3rd and 4th bands. It is substantially distorted from that obtained by free electron

model. It shows a hole surface at Γ point, a region occupied by a filament of electrons at a point along ΓK line, and a region of holes at a point along MK line. Felming et al [4.2.6] have calculated the Fermi surface of Sc using APW method. This Fermi surface would consist of a multiply connected surface in 3rd and 4th bands. It is departed from that calculated by cellular method [4.2.5]. The difference between the two calculated Fermi surfaces was that the filaments of electrons along ΓK line are vanished. Bogod and Eremenko [4.2.2] have measured the shape of Fermi surface of Sc using magneto resistance measurements. They have concluded that the Fermi surface of Sc is multiplied connected in a complicated shape in 3rd and 4th bands. However this measurements could not differentiate between the above mentioned two calculated Fermi surfaces [4.2.5] and [4.2.6]. The band structure of Y has been calculated using cellular method [4.2.5] and APW [4.2.7] method. Loucks [4.2.7] has obtained Fermi surface of Y using APW method. This Fermi surface consists of entirely contained in the 3rd and 4th bands and separates a multiply connected region of holes enclosing Γ, A and L points, and multiply connected region of electrons enclosing K, and M points. This Fermi surface was different from that obtained using cellular method [4.2.5] in which 4th band was found to be empty at M point.

### IV.2.1. 2D-ACAR spectra $N(P_y,P_z)$ and momentum density $\rho(P)$

Figure 4.2.2 represents 2D-ACAR spectra in two extreme angles $0^0$ and $30^0$ as contour map, of (a) Sc and (b)Y, respectively. The written angles above the spectra show the deviation angle on [0001] projection direction. The spectra of Sc are measured up to 20 mrad through a pair of 128 detectors 2D-ACAR experimental set-up and that of Y are measured up to 30 mrad through a pair of 256 2D-ACAR experimental set up. The represented figures show some distortions in the upper part of the spectra of both Sc and Y. These distortions will discuss later. From the measured spectra of both of Sc and Y, $\rho(P)$ are reconstructed in extended zone scheme using reconstruction technique based on direct Fourier transformation.

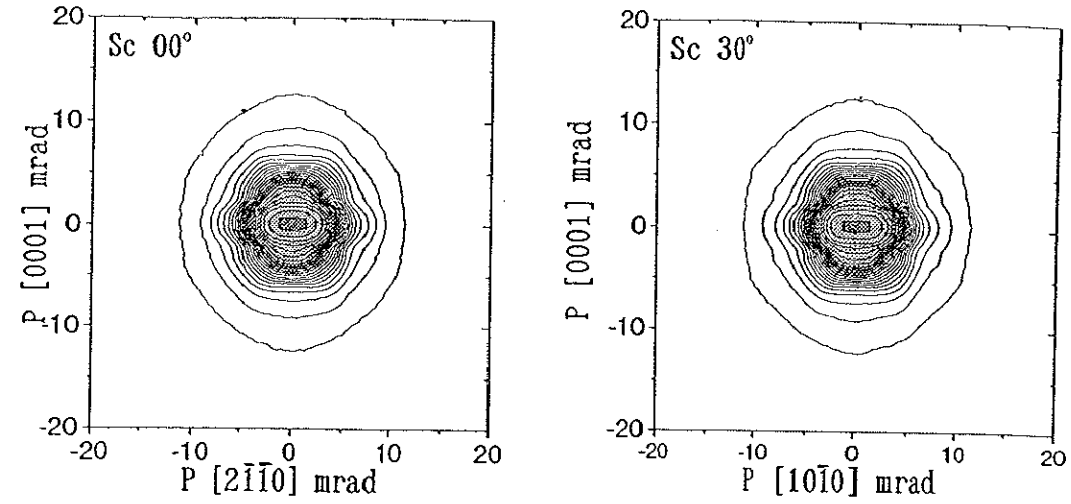


(a)

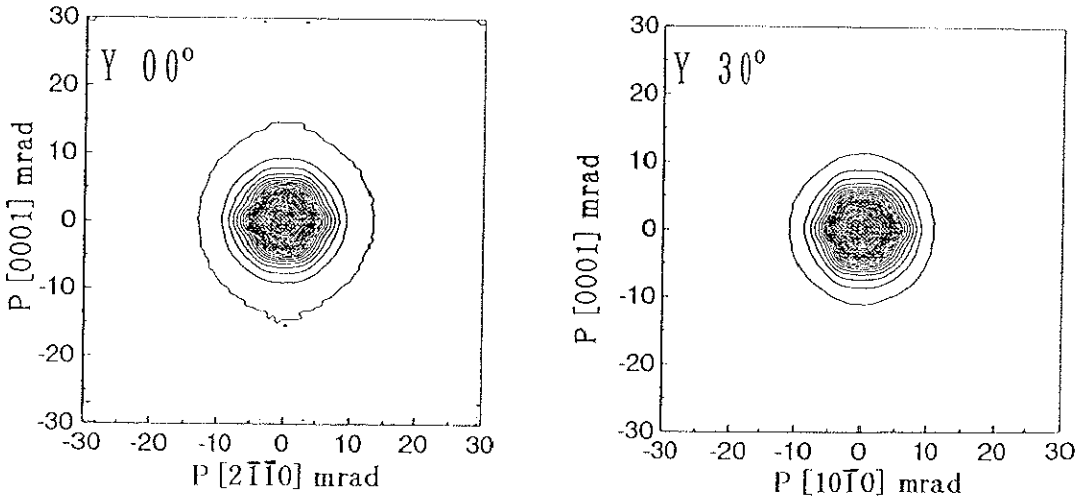


(b)

Figure 4.2.2 the 2D-ACAR spectra of Sc and Y in two extreme angles 0° and 30°. The spectra represented as a contour map in step of 2% of the peak height.

Figure 4.2.3 shows the contour map of ρ(P) in ΓMK, ALM and AHK planes respectively for (a) Sc and (b) Y. The dark circles show the position of reciprocal lattice points. Figure 4.2.4 shows ρ(P) in ΓM and ΓK directions for Sc and Y, respectively. Breaks are observed around 2.5 mrad and HMC's are shown in figures (c) and (d). The above mentioned distortions in the upper part of the spectra are shown as breaks and they are attributed to the fact that both of Sc and Y contain 3 valence electrons, i.e., the conduction band is partially filled. Therefore, the momentum density displays a discontinuity at Fermi momentum $k_F$ in first Brillouin zone and at momentum $k_F < G$ (G represents the vector of the reciprocal lattice points) in higher zones, but these breaks are superimposed on continuous contribution from the full valence band. Figure 4.2.5 and 4.2.6 show the enlarged spectra of Sc and Y in ΓMK, ALM and AHK planes respectively, up to 10% from their maximum. The nearest neighbor reciprocal lattice points for both Sc and Y, $G_{111}$, are obtained at ΓM=7 and 6.5 mrad , ΓK = 8.5 and 7.5 mrad and ΓA=4.5 and 4.2 mrad, respectively. These values are closed to the Fermi momentum ($P_F$ = 5.639 and 6.209 mrad for Sc and Y, respectively). As it is well known, both of Sc ($3d\ 4s^2$) and Y ($4d\ 5s^2$) include tight bounded electrons (d-electron). Therefore, the strongest signal of the d-like parts of Fermi surface occurs in the higher Brillouin zone. This is different from the divalent HCP structure metals Mg, Zn and Cd [4.2.8] in which the main contribution to Fermi surface is due to $G_o$ (G=0), and the first Brillouin zone is the strongest, and Fermi surface in the higher zones is weaker.

Fermi radii of Sc and Y are determined from the locus of $|\nabla\rho(P)|_{Max}$. Figure 4.2.7 shows the experimental Fermi radii along ΓMK, ALM and AHK planes normalized to free electron Fermi radius of individual metals, respectively. The free electron Fermi radii of Sc (=5.639 mrad) and Y (=6.209 mrad) are taken as a unity. In ΓMK and ALM planes the angle is measured from ΓM direction, while in AHK plane it is measured from ΓK direction. In ΓMK plane the maximum deviations from the free electron Fermi radius for Sc and Y are hesitating around --6% and -15% (about 0.04 and 0.13 a.u.), respectively. In ALM plane the maximum deviations from the free electron Fermi radius is around -15% and

**±20% (about 0.11 and 0.16 a.u) for Sc and Y, respectively. In AHK plane the maximum deviations from the free electron Fermi radius for Sc is at ΓA direction -12% (about 0.08 a.u.) and for Y is at ΓH direction +35% (about 0.3 a.u.). In conclusion, the maximum deviation from the free electron Fermi radii of the examined metals are larger than the experimental error (0.02 a.u.). As a result, Fermi surfaces of Sc and Y are deviated from the free electron model.**

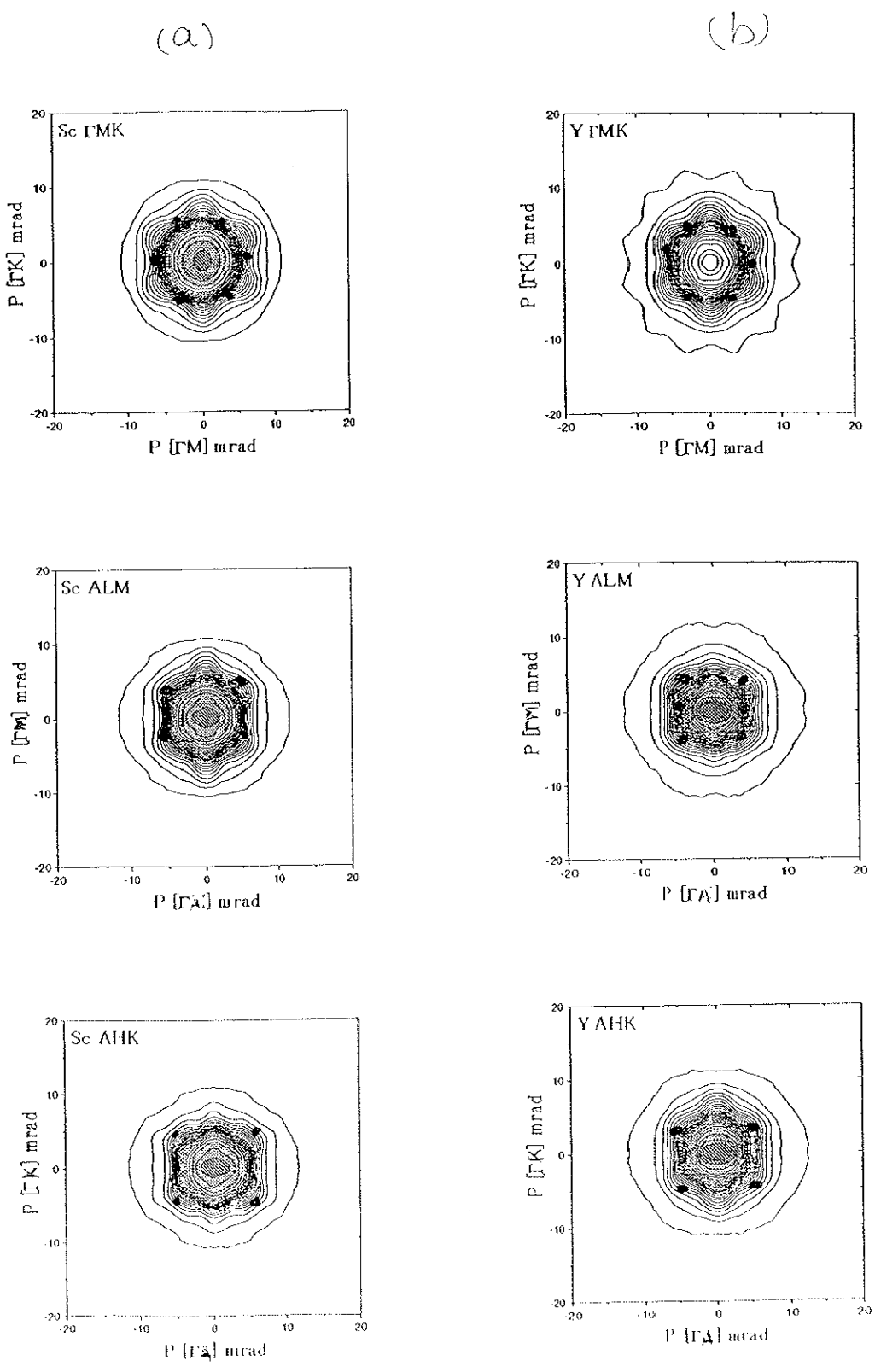


**Figure 4.2.3 the electron density in the momentum space ρ(P) of (a)Sc and (b)Y in ΓMK, ALM and AHK plane, respectively, as a contour maps. The dark circles in the spectra shows the reciprocal lattice point position.**

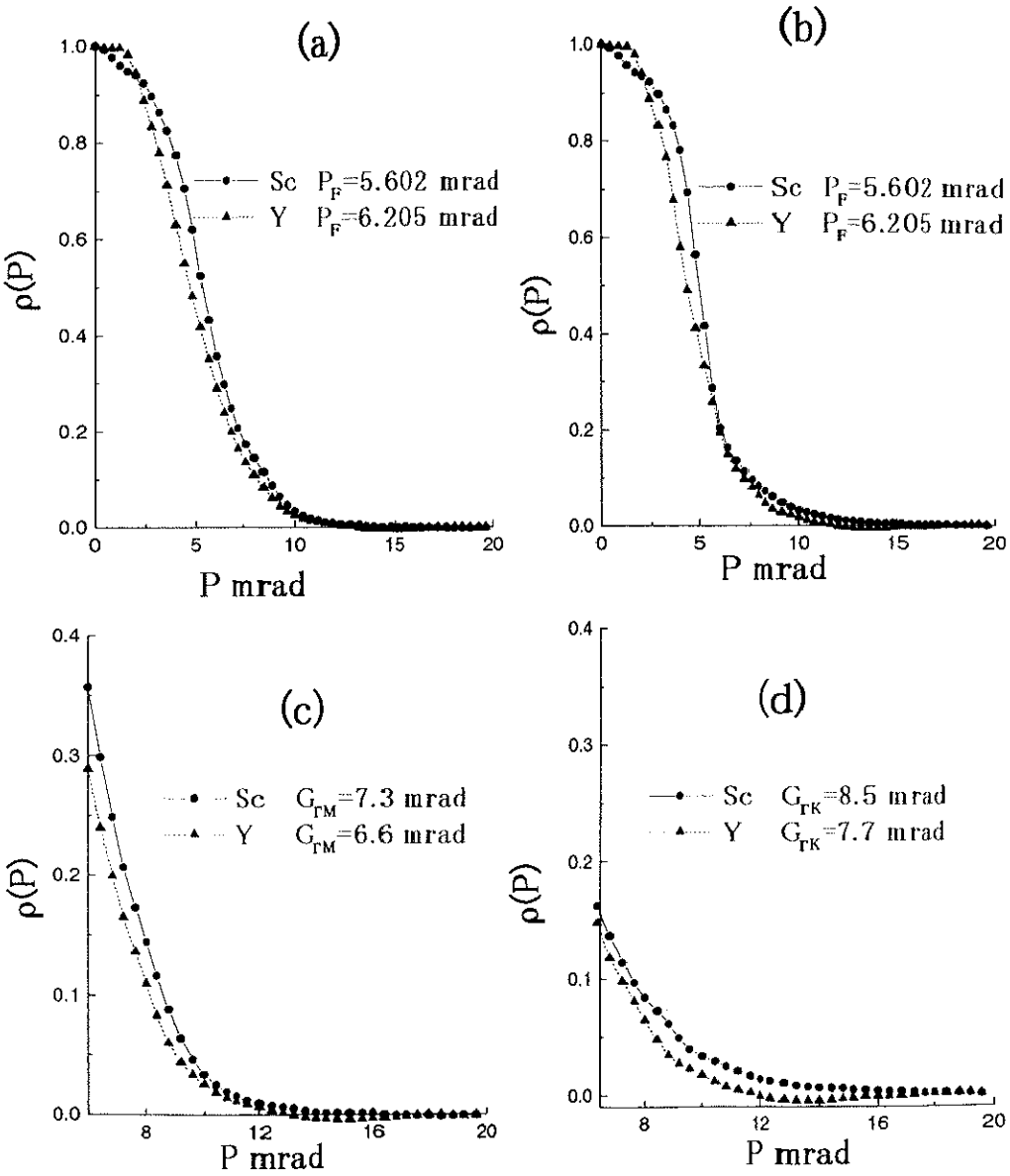


Figure 4.2.4 The spectra of Sc and Y in ΓM and ΓK directions respectively
(a)Sc and Y in ΓM direction up to 20 mrad
(a)Sc and Y in ΓK direction up to 20 mrad
(a)Sc and Y in ΓM direction from 6 mrad up to 20 mrad
(a)Sc and Y in ΓK direction from 6 mrad up to 20 mrad
The Fermi momenta $P_F$ for Sc and Y are represented in the Figure, Also the reciprocal lattice points in ΓM and ΓK.

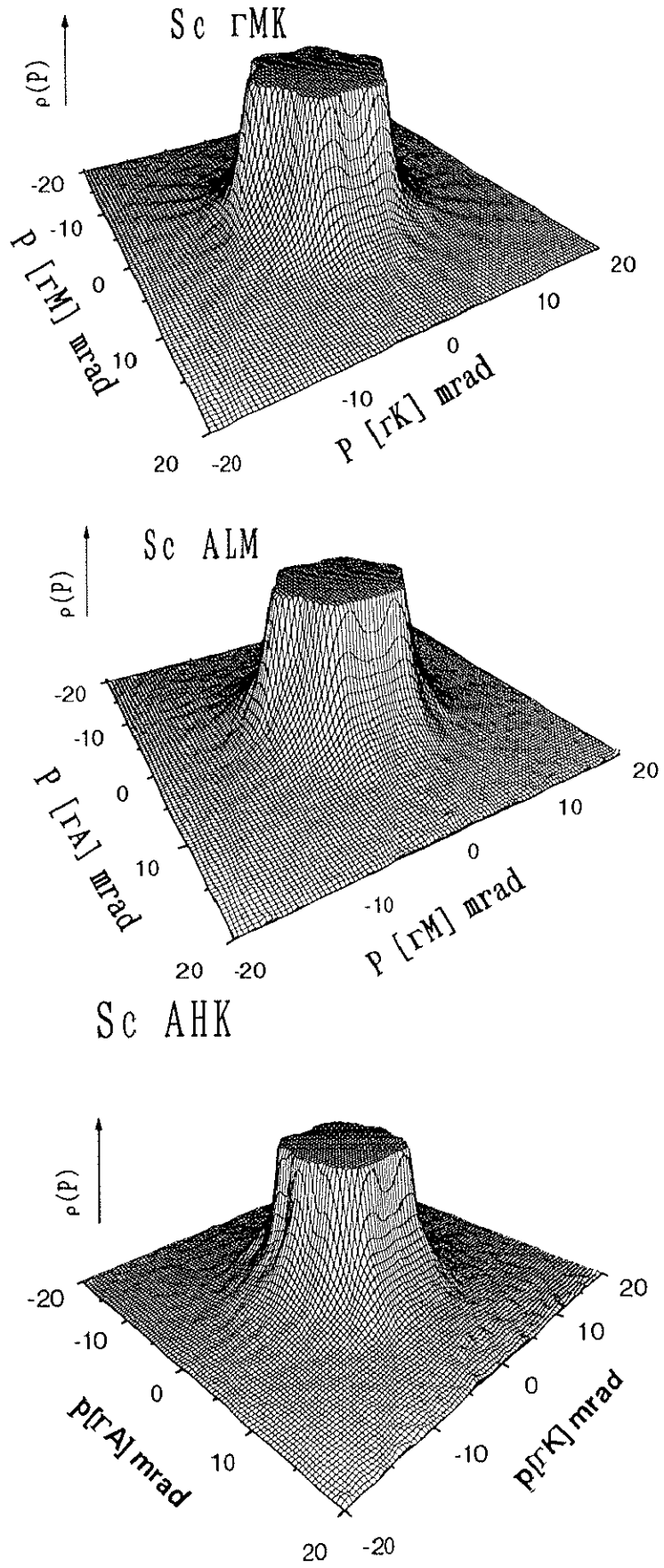


Figure 4.2.5 the enlarged ρ(P)spectra of Sc up to 10% from their maximum in ΓMK, ALM and AHK planes, respectively.

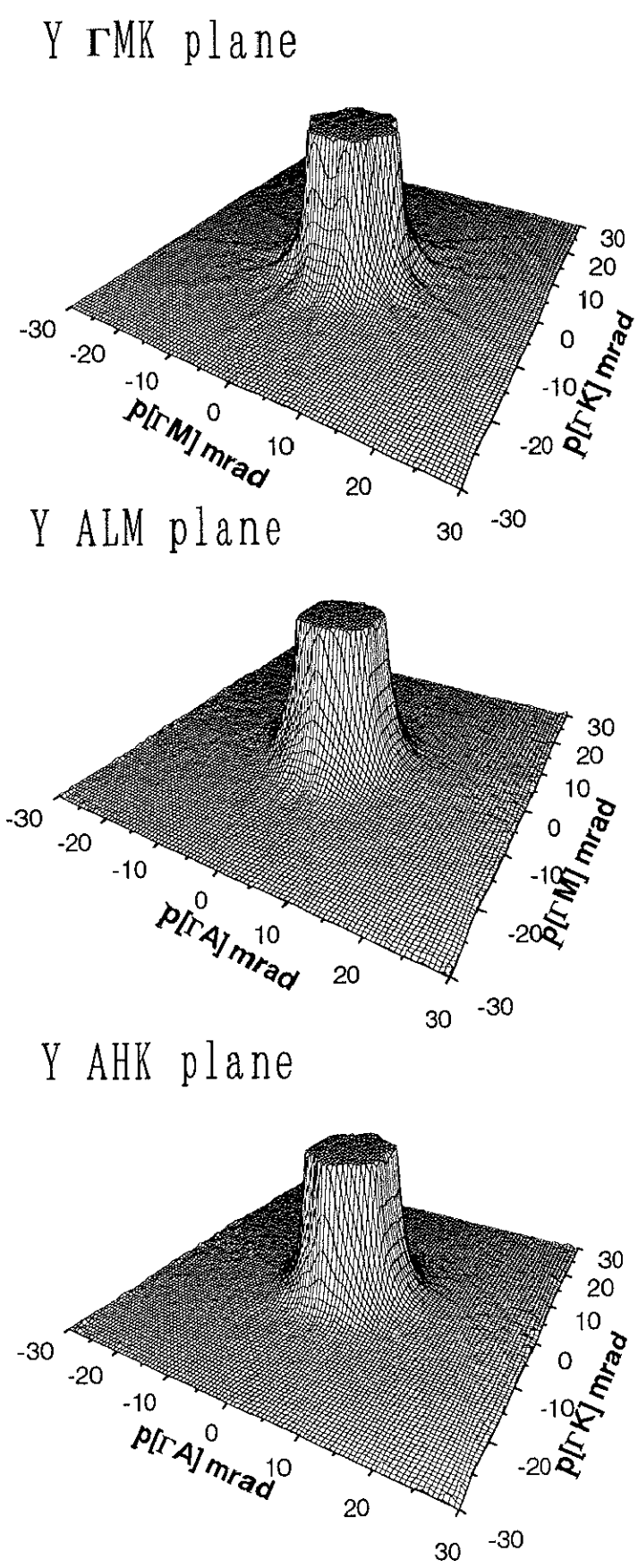


Figure 4.2.6 the enlarged 2D-ACAR spectra of Y up to 10% from their maximum in ΓMK, ALM and AHK planes, respectively.

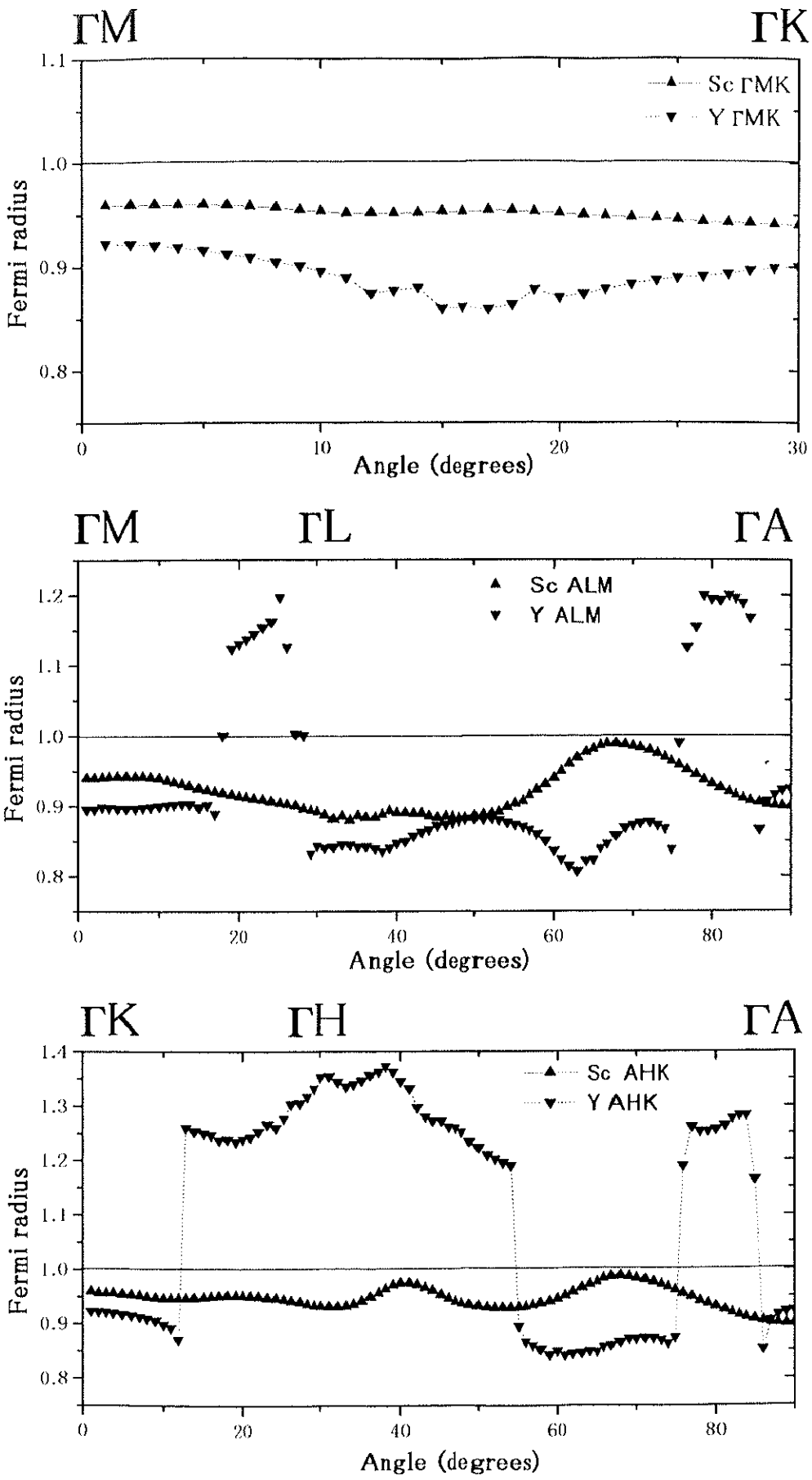


Figure 4.2.7 the normalized Fermi radius of Sc and Y in the ΓMK, ALM and AHK planes, respectively.

### IV.2.2 Electron momentum density in the wave vector space n(k)

Using LCW folding procedure equation (2.4.1) the momentum density, $\rho(P)$ can be reduced to wave vector space, k-space, restricted within the first Brillouin zone. Figures 4.2.8 and 4.2.9 represent the contours of n(k) of Sc and Y, respectively, in 5 cross sections. Figures denoted LCW01 represent ΓMK planes, and that denoted LCW05 represents AHK plane. The other figures are cross sections of the momentum density n(k) with the same intervals. The dark patterns in the figures show the higher momentum density contributions. In the same figure the $1/24^{th}$ part of Brillouin zone of HCP structure is represented. Generally, the represented spectra for both Sc and Y have the same features for the same cross sections. Sc LCW01 shows a hole surface at Γ point. It doesn't change its behavior up to A point in figure Sc LCW05. At K point, a small electron surface starts to grow up to Fig. ScLCW05 at H point. The electron surface at M point in Sc LCW01 still keeping its behavior up to Sc LCW05 at L point. For Y, Nearly the same feature of Fermi surface is observed around Γ and A points, which show a hole surfaces while K point shows an electron surface. At YLCW01 M point shows an electron surface its behavior changes at YLCW02 to be a hole surface up to the Y LCW05 at L point. Figure 4.2.10 represents the intersection of different symmetry planes in the $1^{st}$ Brillouin zone for Sc in ΓMK, ALH, ΓALM and ΓAHK planes, respectively. The hole surfaces at Γ point and at A point are observed in represented figures, and also the hole surface at L point. The electron surfaces at K, M and H points are observed from the four figures. Figure 4.2.11 shows the intersection of the different symmetry planes in the first Brillouin zone for Y in ΓMK, ALH, ΓALM and ΓAHK planes, respectively. The same features are observed at Γ, A and L points which contain a hole surfaces and K, M and H points show electron surfaces. From the above mentioned results it can be seen that both of Sc and Y have the same characters of Fermi surface namely; hole surfaces at Γ, A and L points and electron surfaces at K, M and H points. Figures 4.2.12 represent the normalized density n(k)% in wave vector space along the principal symmetry lines for Sc and Y respectively. The sharp lines represent the calculated results using APW method[4.2.5]. The dotted lines show the calculated results

**using cellular method for Sc[4.2.6] and Y[4.2.7], respectively. The thickness of the bands are calculated from the statistical analysis using least square method (SALS). Table 4.2.1 shows the estimated values of the bands using least square method. The dimensions of Fermi sheets from cellular and APW methods are used as input parameters. As seen from Fig. 4.2.12, for Sc, both of the hole surfaces at Γ point and at L points exceed the 3rd band while the hole surface at A point is observed at 2nd band. The electron surfaces at M and K points are observed at 4th band and the electron surface around H point are observed at 3rd band. The present results of Sc show good agreement with that obtained by the APW method, Except at Γ point. For Y, It shows that Γ and A points are represented as a hole surface at 2nd band and L point shows a hole surface at 3rd band. M and K points show electron surfaces at 4th band. The electron surface at H point is observed at 3rd band. The present results of Y show good agreement with that obtained by APW method. From the above mentioned results, it can be concluded that Fermi surface of Sc consists of Two categories; the first is hole surfaces at Γ and L points in the 3rd band and a hole surface at A point in 2nd band. The second is electron surfaces at M and K points in 4th band. The Fermi surface of Y consists of two categories; the first is, hole surfaces at Γ and A points in 2nd band and the hole surface at L point in 3rd band. The second is, electron surfaces at M and K points in 4th band.**

| | Sc Cellular | Sc APW | Y Cellular | Y APW |
|---|---|---|---|---|
| 2nd band $n_2$ | 94.4±4.3 | 93.4±9.65 | 91.6±1.11 | 88.7±1.22 |
| 3rd band $n_3$ | 101.8±6.7 | 100.9±1.85 | 101.3±1.93 | 96.9±1.5 |
| 4th band $n_4$ | 105.7±5.2 | 108.7±104 | 108.5±1.67 | 108±1.4 |

Table 4.2.1 the obtained fitting parameters using least square-fitting program, for Sc and Y. Cellular and APW represent that the used input dimensions are from the bands from cellular and APW methods, respectively. The values of the bands are represented with its uncertainty of calculation.

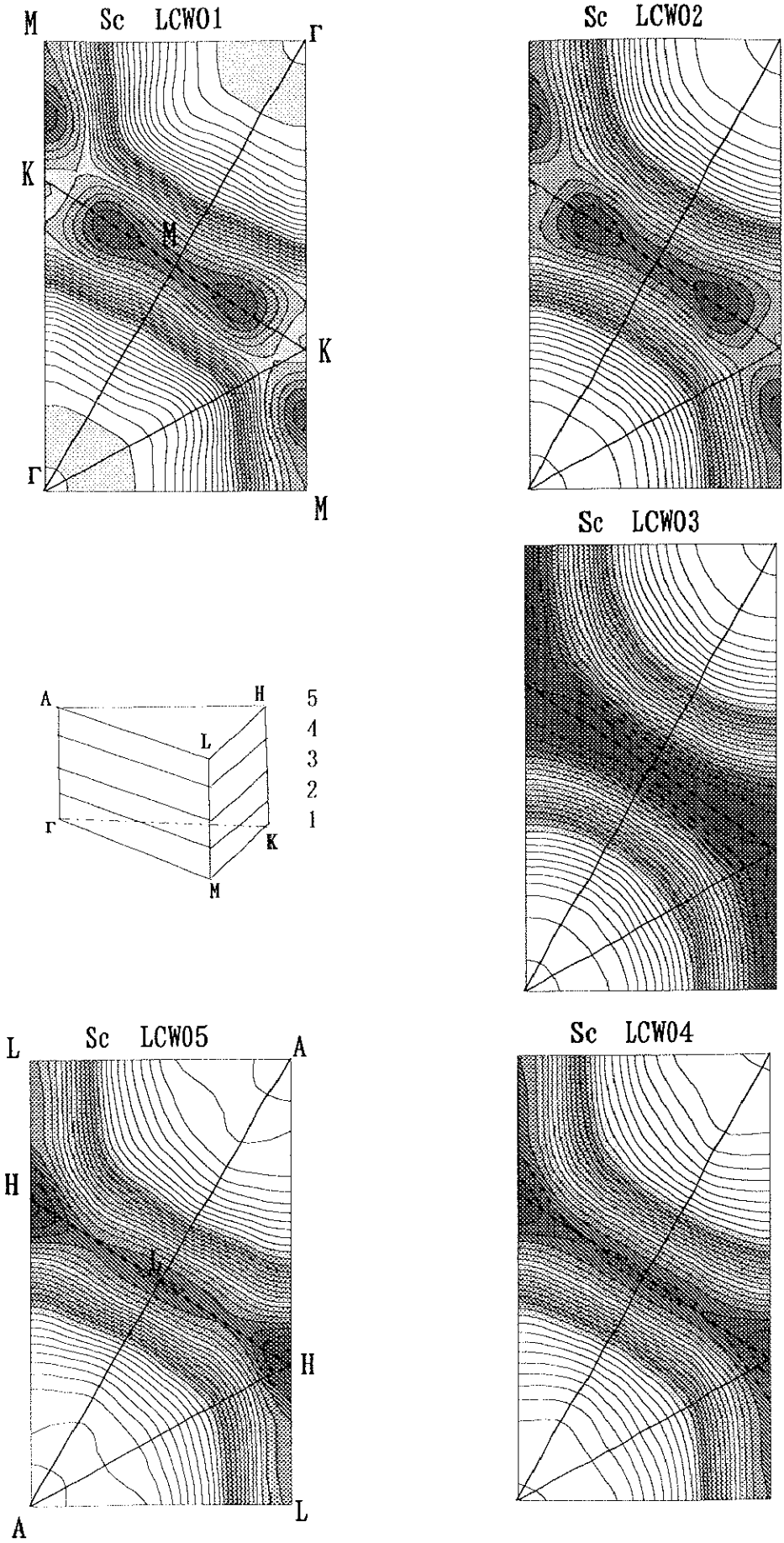


Figure 4.2.8 the contour of the Fermi surface cross sections of Sc normal to c-direction from ΓMK to AHL planes. the dark parts show the higher electron density

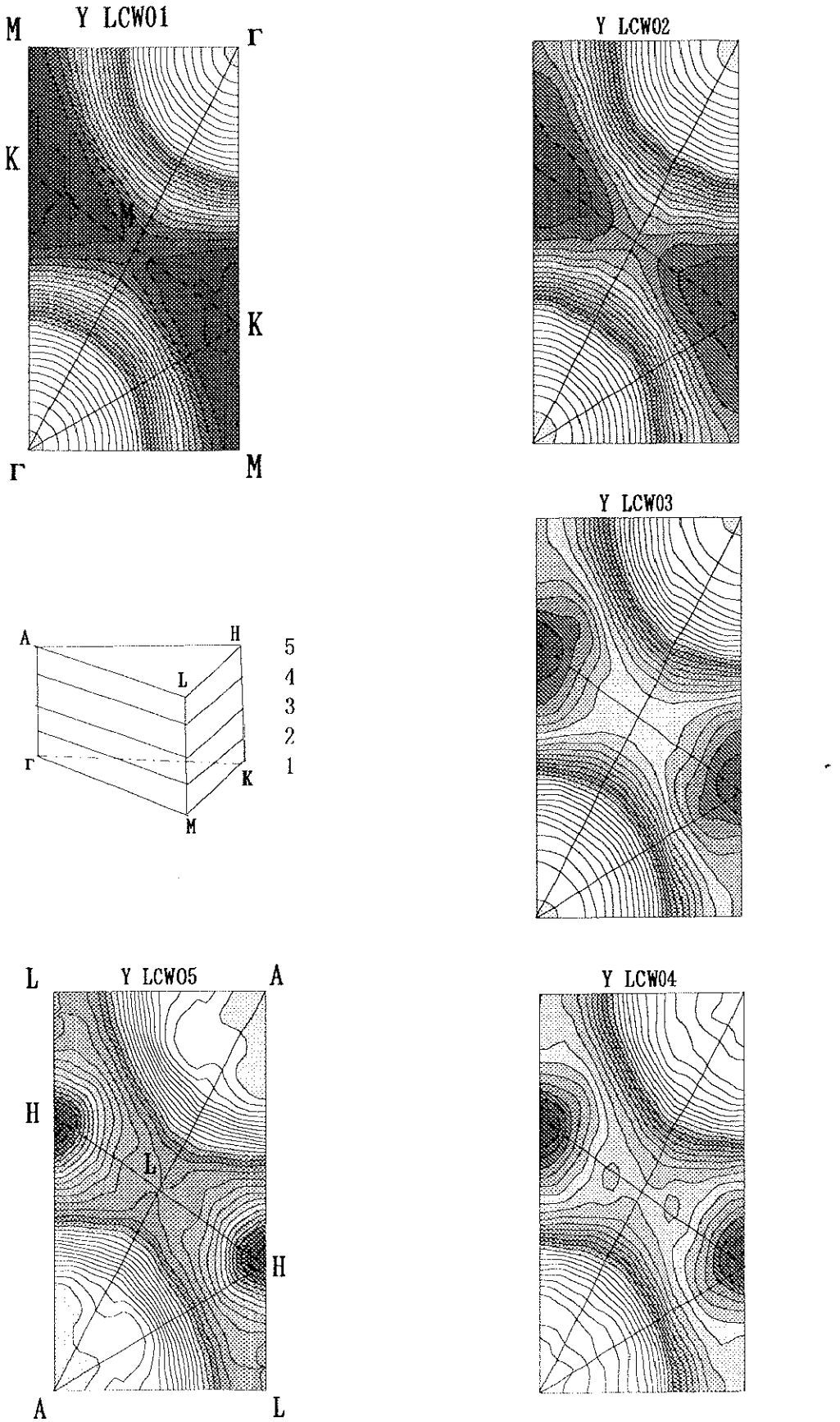


Figure 4.2.9 the contour of the Fermi surface cross sections of Y normal to c-direction from ΓMK to AHL planes. the dark parts show the higher electron density

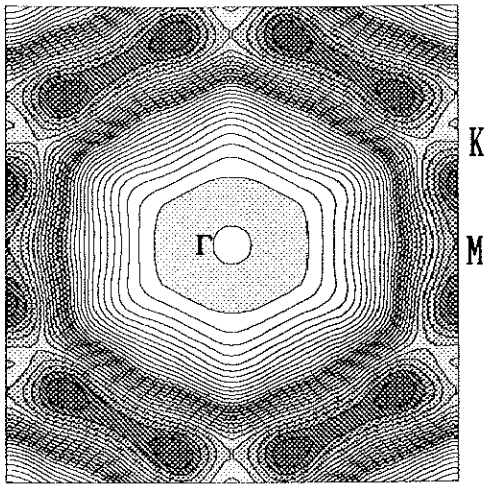


Sc ΓMK plane

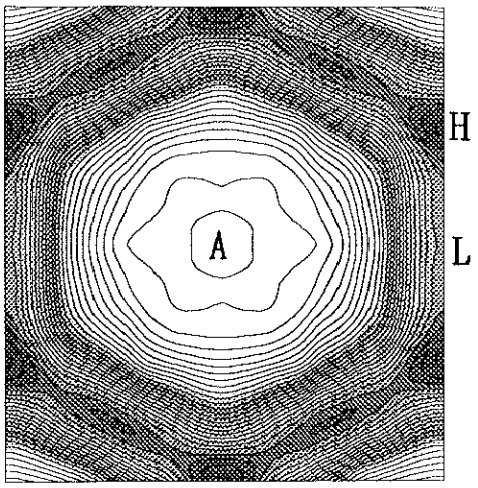


Sc ALH plane

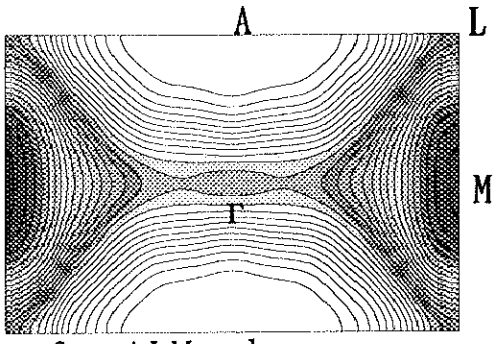


ScrALM plane

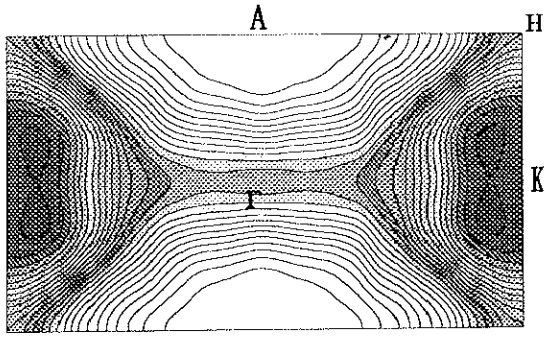


Sc ΓAHK plane

Figure 4.2.10 the electron density in the wave vector space n(k) of Sc in ΓMK, ALH, ΓALM and ΓAHK planes, respectively.

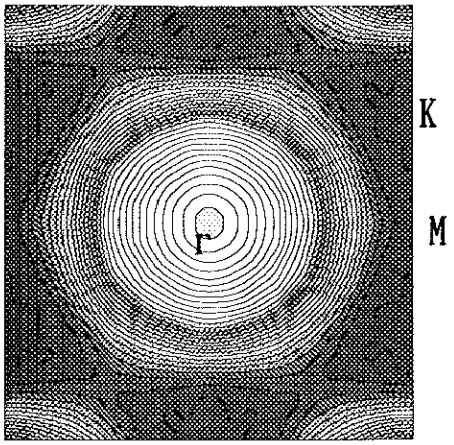


Y ΓMK plane

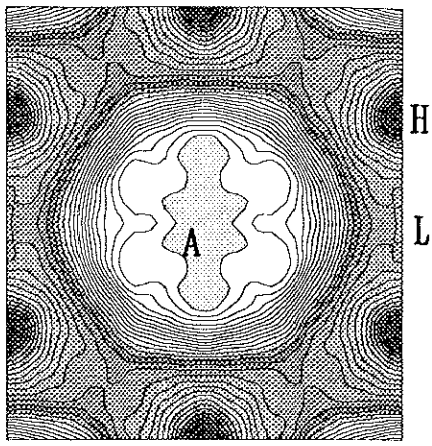


Y ALH plane

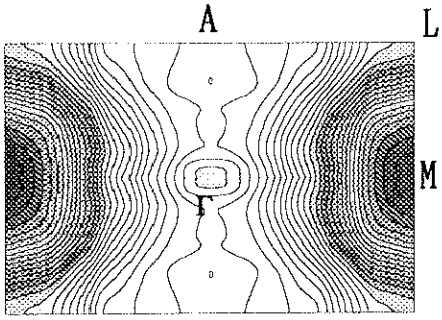


YΓALM plane

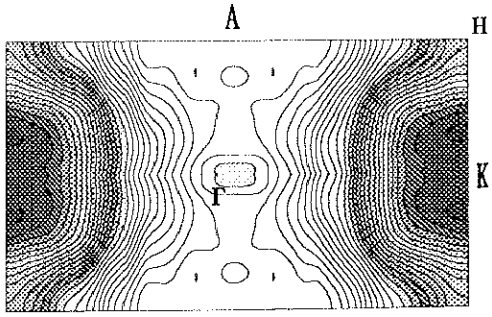


Y ΓAHK plane

Figure 4.2.11 the electron density in the wave vector space n(k) of Y in ΓMK, ALH, ΓALM and ΓAHK planes, respectively.

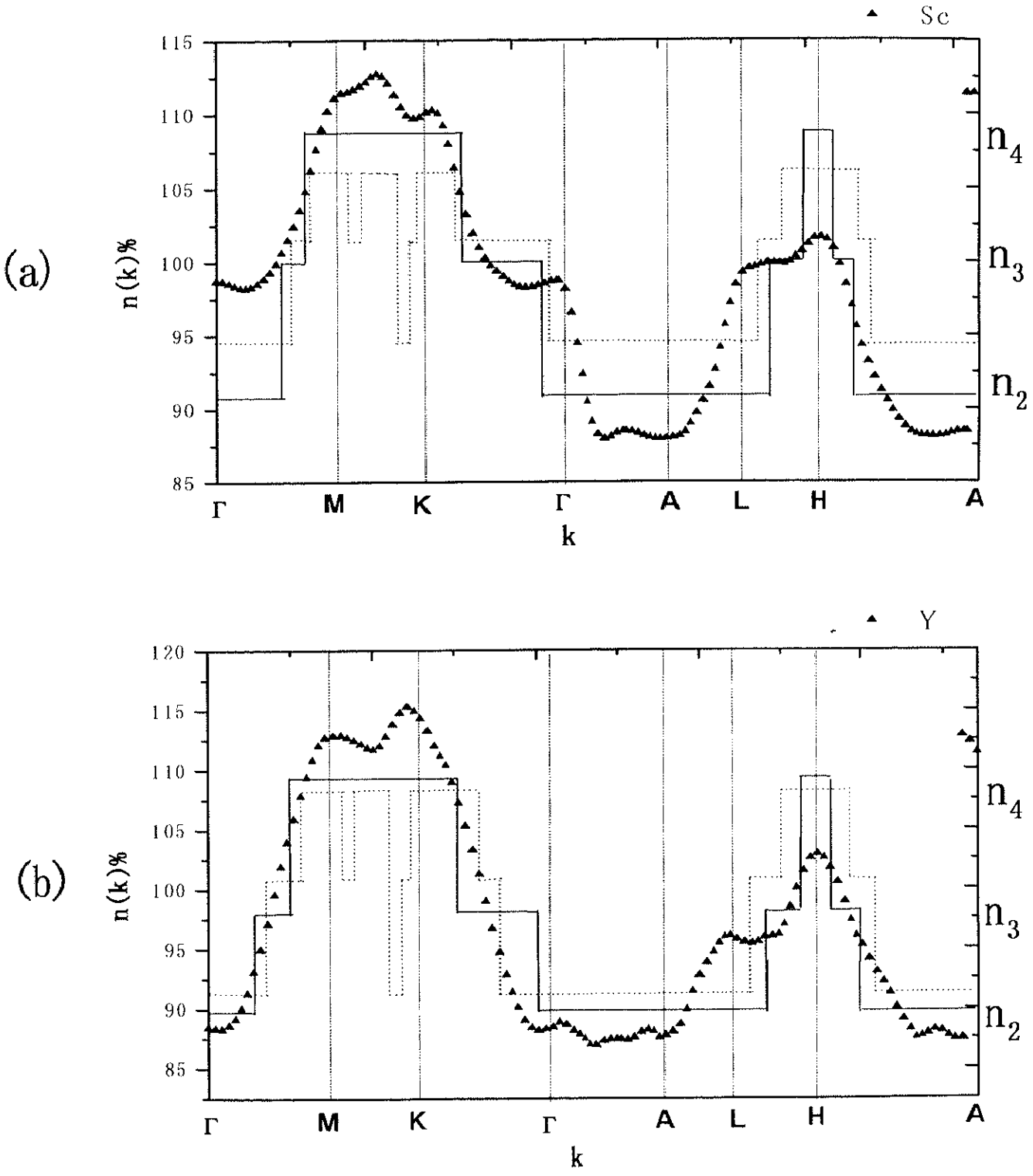


Figure 4.2.12 the normalized electron density in the wave vector space n(k)% for (a) Sc and (b) Y. The sharp and the dotted lines show the results of the band structure calculation using the APW and cellular methods, respectively.

## IV.3 HCP structure metals of group IVA Titanium Ti, Zirconium Zr and Hafnium Hf

The HCP structure of valence four is most common among the transition metals. The combination of uniaxial symmetry and the two atoms per unit cell results in their electronic structure, which is more complex than that of cubic structure. This complexity is reflected in their Fermi surface structures. However, the experimental work of determining the momentum density and Fermi surface are relatively little for Ti and Zr, and according to our knowledge the only experimental study of the momentum density and Fermi surface has been done by the author[4.3.1]. The free electron Fermi surface of HCP structure metals of valance four has been predicted by Thorsen et al [4.3.2]. Then, they have determined the Fermi surface of Zr using dH-vA experimental technique. Figure 4.3.1 represents the Fermi surface of their model, it shows bands 1 and 2 full all over and regions of electrons in bands 3, 4, 5 and 6 occupy Brillouin zone.

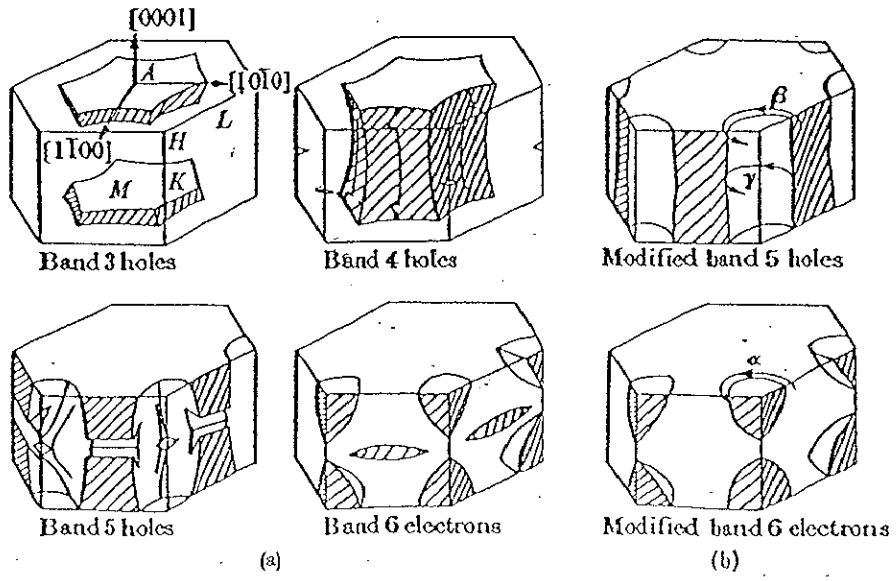


Figure 4.3.1 Sketches of the free-electron Fermi surface for HCP metal of valence 4, and (b) modifications of the Fermi surface in the 5th and 6th band proposed by Thorsen and Joseph [4.3.2] to account for the observed de Haas-van Alphen results in Zr.

Altmann et al [4.3.3] performed a cellular band structure calculation for Zr. They investigated a muffin tin potential constructed from that obtained by Mattheiss [4.3.4]. The same authors [4.3.5] have compared their results of band structure calculation for Ti and Zr. Their band structure calculation shows that Fermi surface of Ti would consist of: closed pocket of holes around L point in the 3$^{rd}$ and 4$^{th}$ bands, and closed pocket of electrons in the 5$^{th}$ and 6$^{th}$ bands around Γ point. Hygh et al [4.3.6] calculated the band structure, for Ti, using the APW method. This band structure was different from that obtained by Thorsen et al [4.3.2] and by Altmann et al [4.3.3]. Papaconstantopoulos [4.3.7] has studied the band structure calculation of Ti using LCAO method and he found that Ti's Fermi surface consists of; a hole surface around Γ and A points at the 3$^{rd}$ and 4$^{th}$ bands, and two electron surfaces around H point at the 5$^{th}$ and 6$^{th}$ bands. Loucks [4.3.8] has calculated the band structure of Zr using the APW method. The obtained Fermi surface by this method was deviated strongly from that calculated by Altmann et al [4.3.5] and Hygh et al [4.3.6]. This Fermi surface consists of a region of holes with an axial rotational symmetry located along the [0001] axis in the 3$^{rd}$ and 4$^{th}$ bands, an isolated region occupied by electrons around H point in the 5$^{th}$ band and small ellipsoidal pockets of electrons at H point in the 6$^{th}$ band. Nearly the same results of Zr's Fermi surface have been obtained from Ref. [4.3.7]. For Hf, Jepsen et al [4.3.9] have calculated the band structure of some of transition metal using RAPW Method. They have shown that the band structure of these materials is synthesized from s p and d bands. Their results of Fermi surface of Hf were departed from that obtained by the free electron model [4.3.2]. This Fermi surface would consist of the 3$^{rd}$ and 4$^{th}$ hole surfaces around Γ and A points, and 5$^{th}$ and 6$^{th}$ electron surfaces around H point. The band structure calculation using the LCAO method [4.3.7] has shown that the Fermi surface of Hf consists of; a hole surface around Γ point at the 3$^{rd}$ band, an electron surface at 4$^{th}$ band at A point, and two electron surfaces along H point at the 5$^{th}$ and the 6$^{th}$ bands.

IV.3.1 2D-ACAR measurement yields $N(P_y, P_z)$,

Figures 4.3.2 shows the contour map of Ti, Zr and Hf, respectively, in two different inclinations from [0001] projection direction at $0^{\circ}$ and $30^{\circ}$ corresponding to $[2\bar{1}\bar{1}0]$ and $[10\bar{1}0]$,respectively. This figure shows the six folded shapes of HCP metals. From the measured 2D-ACAR spectra in real space, $\rho(P)$ is reconstructed using the reconstruction technique based on Fourier transformation, equation (2.2.2). Figure 4.3.3, 4.3.4 and 4.3.5 show $\rho$ (P) in ΓMK, ALM and AHK planes as contour map for Ti, Zr and Hf, respectively. The high momentum components HMC's due to Umklapp process are observed in the spectra. Figures 4.3.6, 4.3.7 and 4.3.8 show the enlarged spectra up to 10% from their maxima of ΓMK, ALM and AHK for Ti Zr and Hf, respectively. From the above Figures the nearest neighbor reciprocal lattice points $G_{111}$ is obtained for Ti, Zr and Hf at 8.2, 7.4 and 7.6 mrad, in ΓK direction, at 7, 6.4 and 6.5 mrad in ΓM direction and at 5, 4.6 and 4.8 mrad in ΓA direction, respectively. These values are near to or inside the Fermi momentum of Ti (=7.3 mrad.), Zr (= 6.64 mrad) and Hf (= 6.71 mrad). Consequently, these results emphasis that the Fermi surface of Ti ($3d^2 4s^2$), Zr ($4d^2 5s^2$) and Hf ($5d^2 6s^2$) are affected by a strong signal d-like which occur in the higher Brillouin zones. Figure 4.3.9 shows the electron density in the momentum space in ΓM and ΓK directions for Ti, Zr and Hf respectively. This Figure shows breaks in the upper part of the spectra. This breaks are attributed to the fact that the metals of group IVA HCP Ti, Zr and Hf have partly filled conduction band which causes Fermi surface breaks to appear but superimposed on the continuous contribution from the full valence band. As explained above, the HMC's are also observed in this figure.

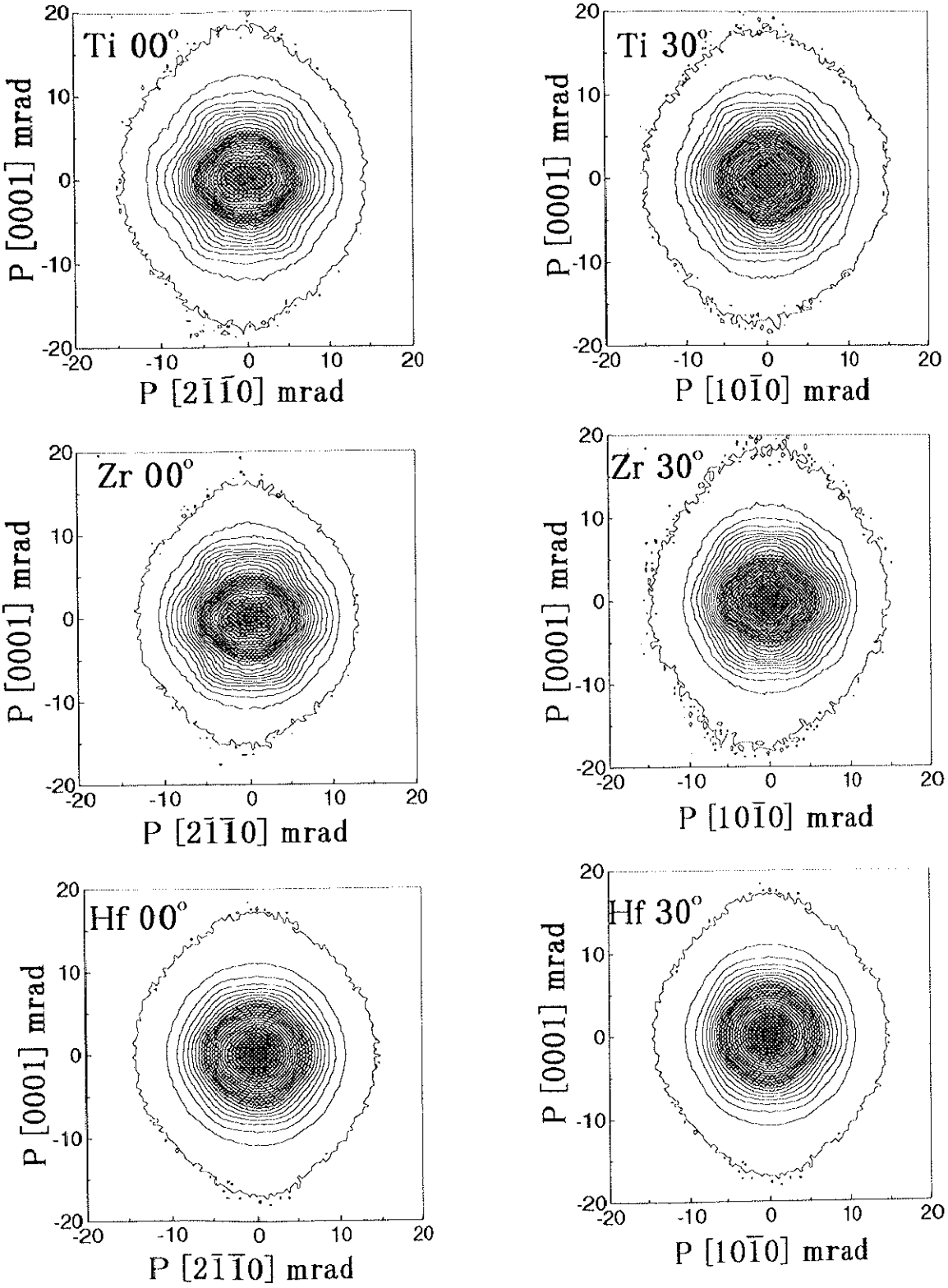


Figure 4.3.2 The 2D-ACAR spectra of Ti, Zr and Hf in two extreme angles 0 and 30°. The spectra represented as a contour map in a step of 2% of the peak height.

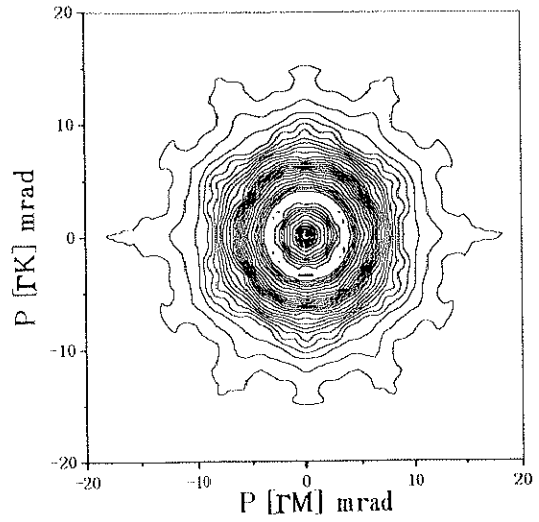


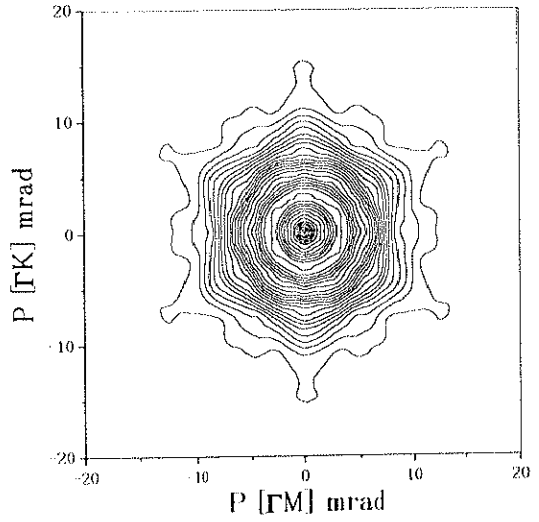


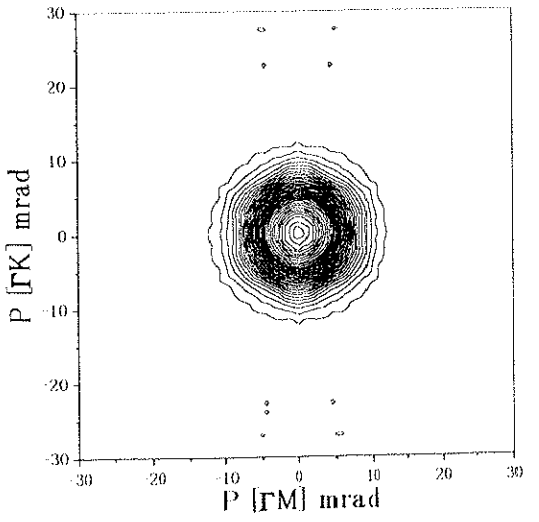


Figure 4.3.3 the electron density in the momentum space $\rho(P)$ of in ΓMK plane of Ti, Zr and Hf, respectively, as contour map.

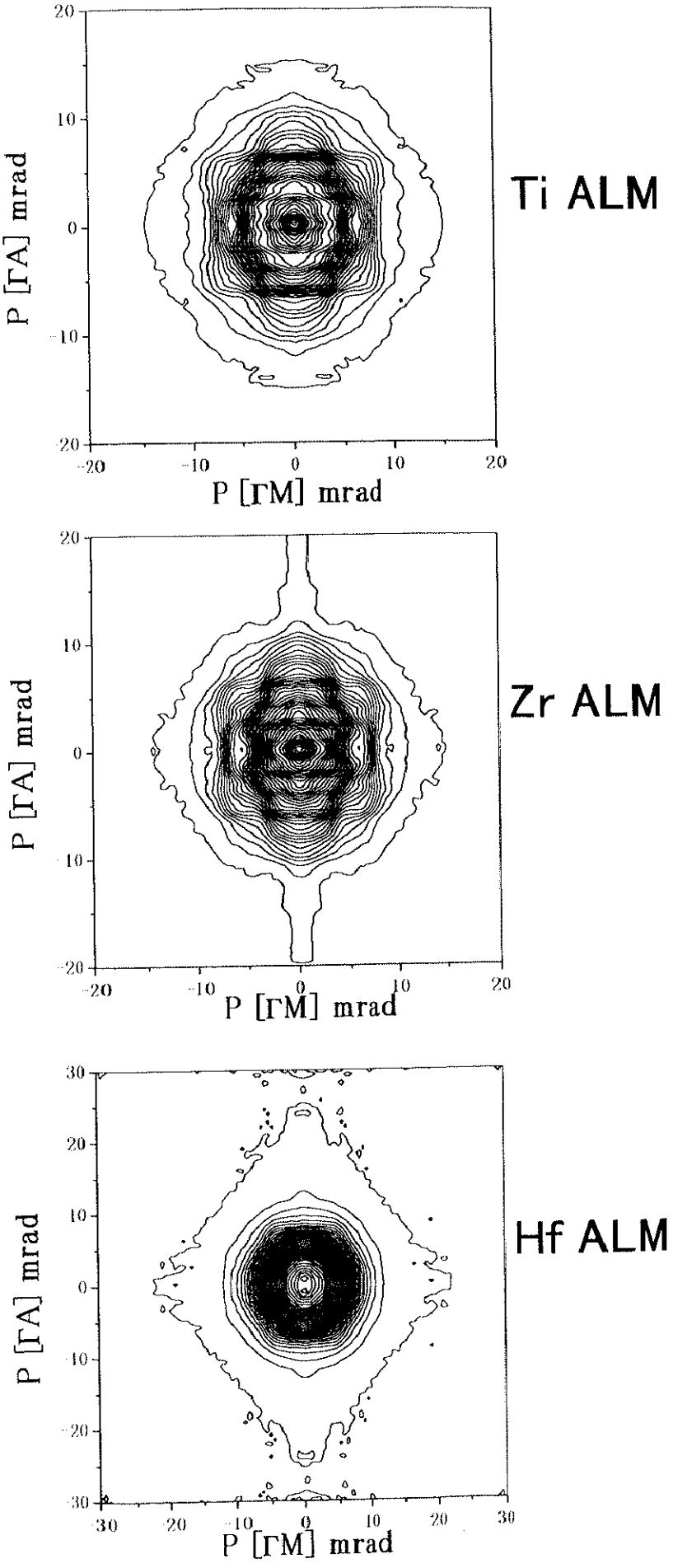


Figure 4.3.4 the electron density in the momentum space $\rho(P)$ of in ALM plane of Ti, Zr and Hf, respectively, as contour map.

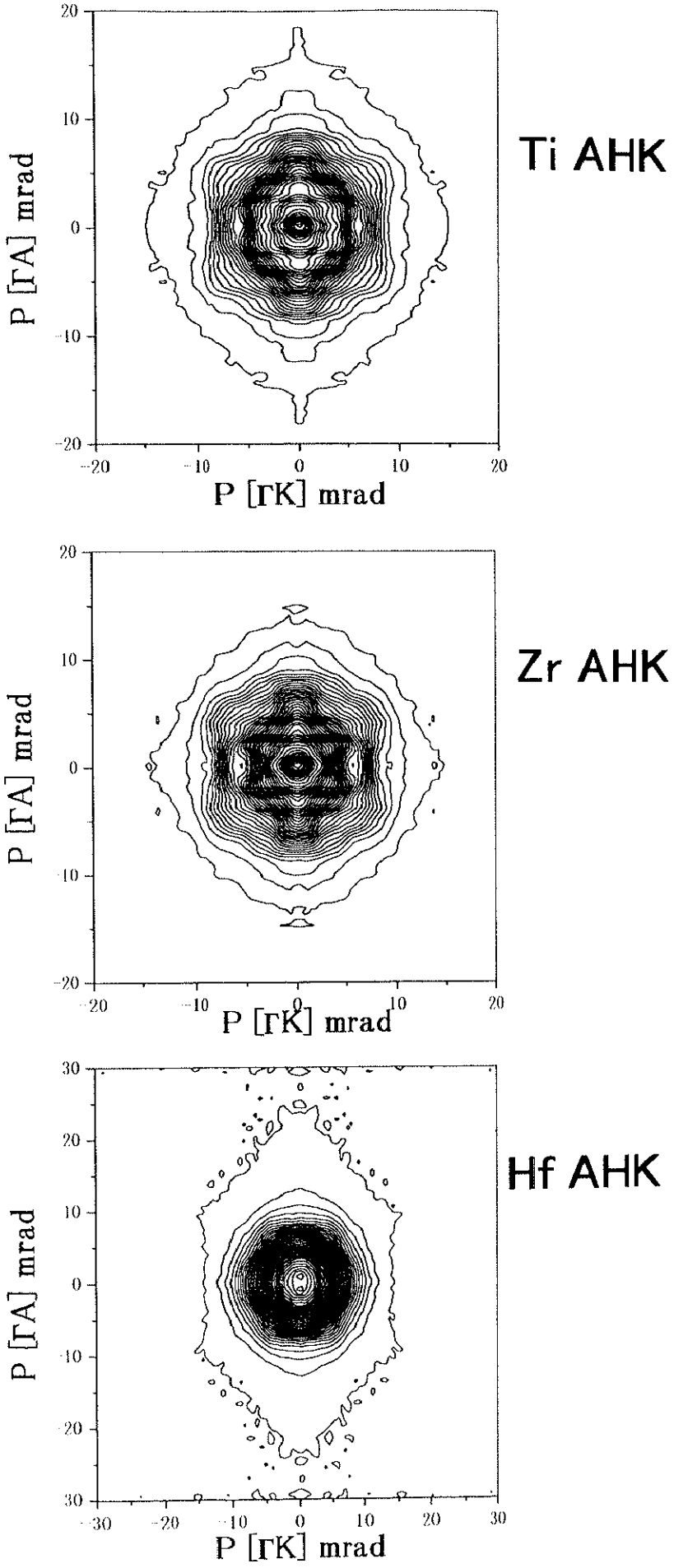


Figure 4.3.5 the electron density in the momentum space $\rho(P)$ of in AHK plane of Ti, Zr and Hf, respectively, as contour map.

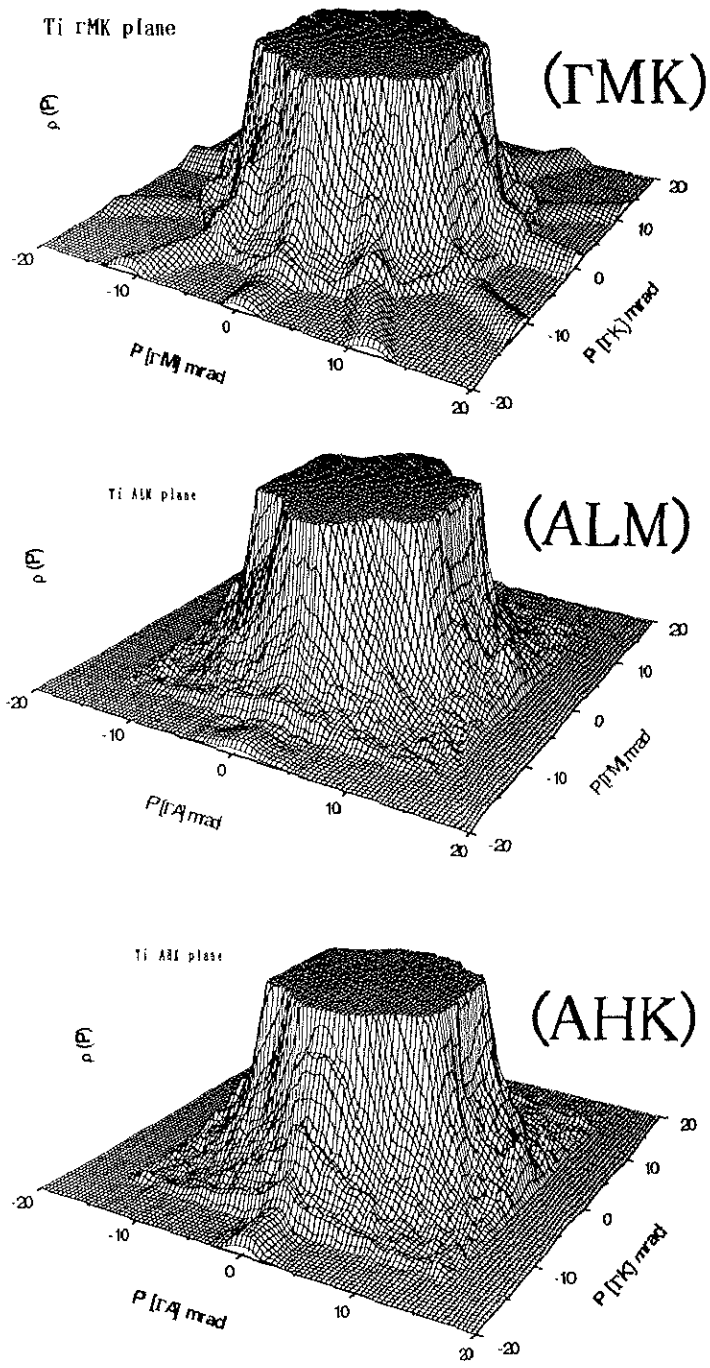


Figure 4.3.6 The enlarged momentum density ρ(P) spectra of Ti, up to 10% from their maxima in ΓMK, ALM and AHK planes as isometric veiw

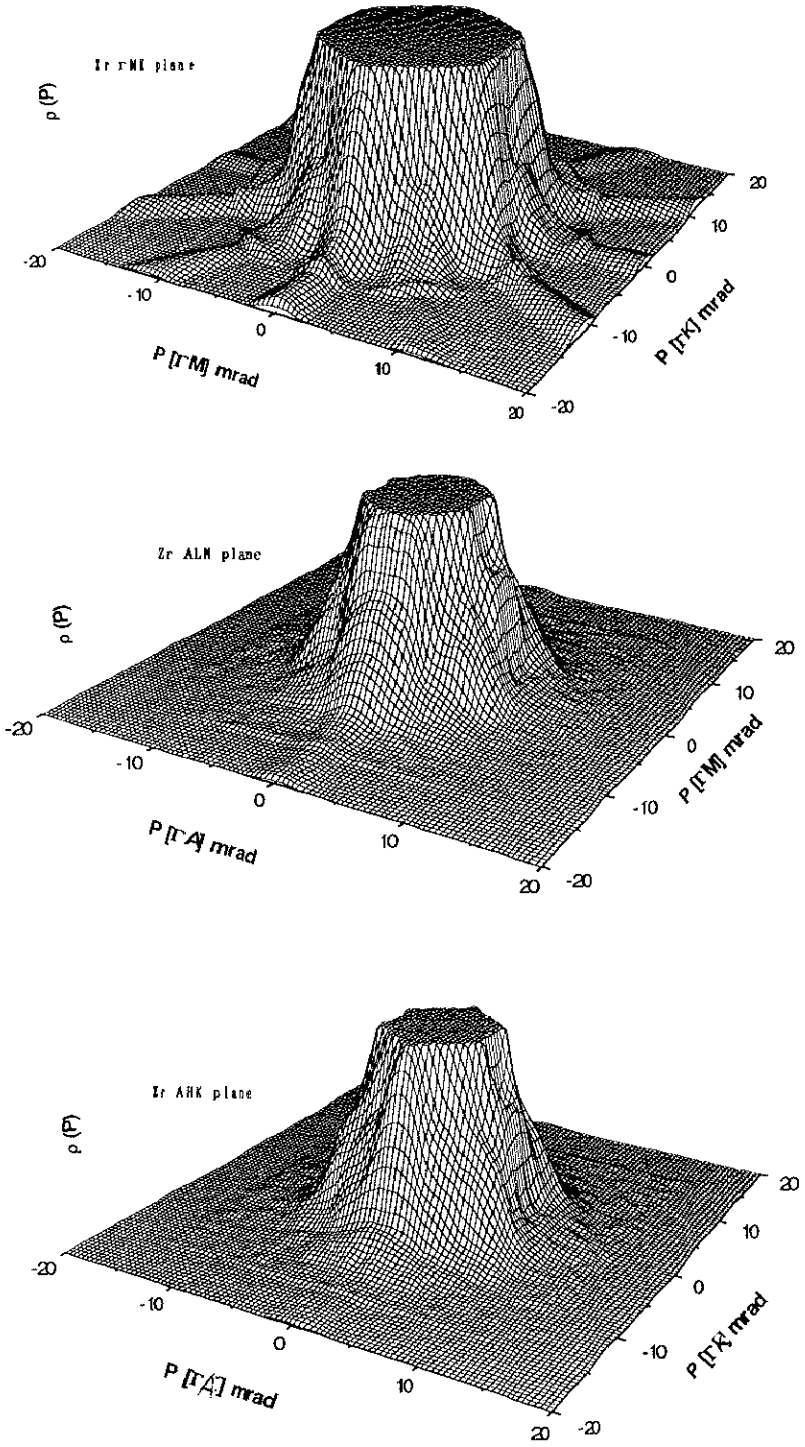


Figure 4.3.7 The enlarged ρ(P) of Zr up to 10% from the maximum in ΓMK, ALM and AHK planes as isometric view.

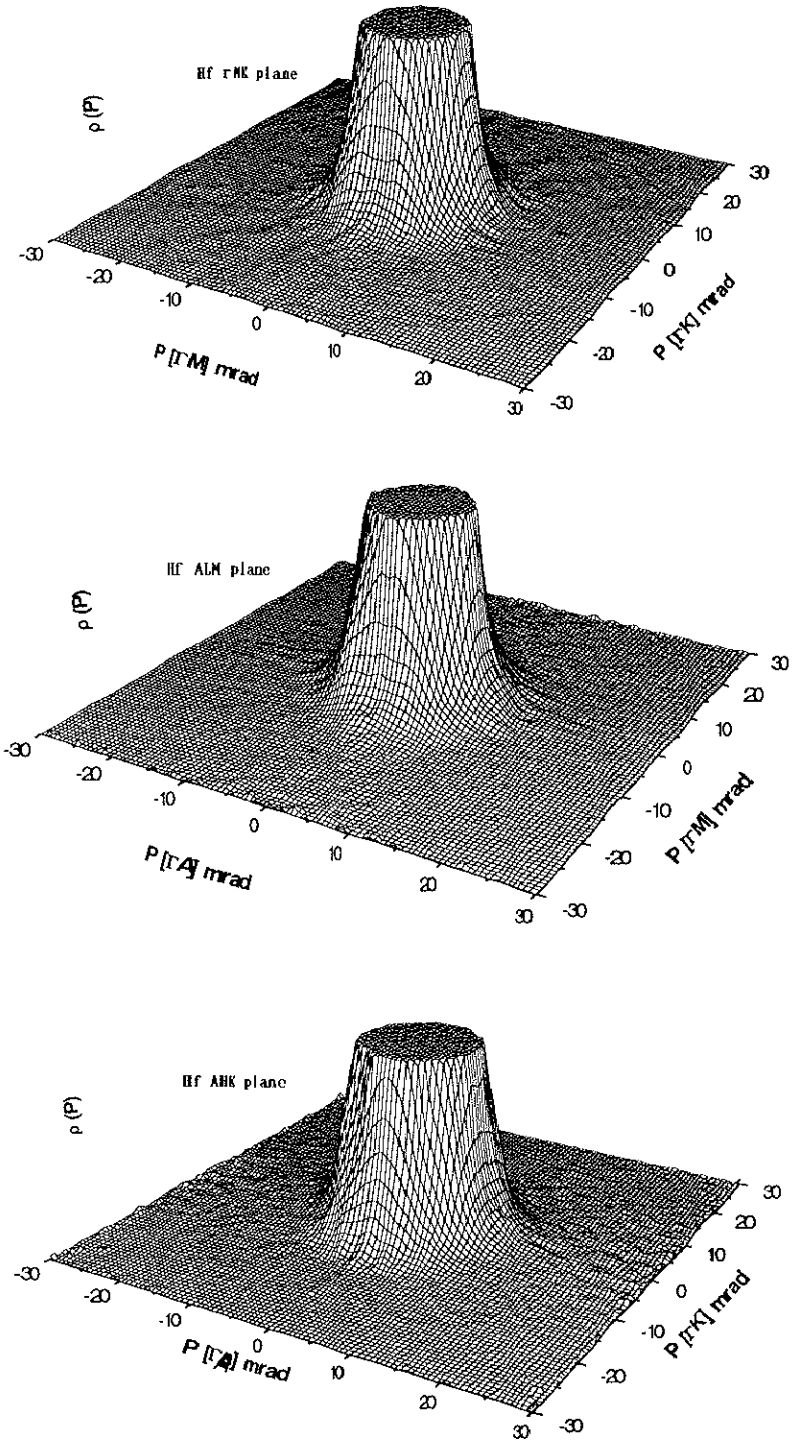


Figure 4.3.8. The enlarged ρ(P) of Hf up to 10% from the maximum in ΓMK, ALM and AHK planes as isometric view.

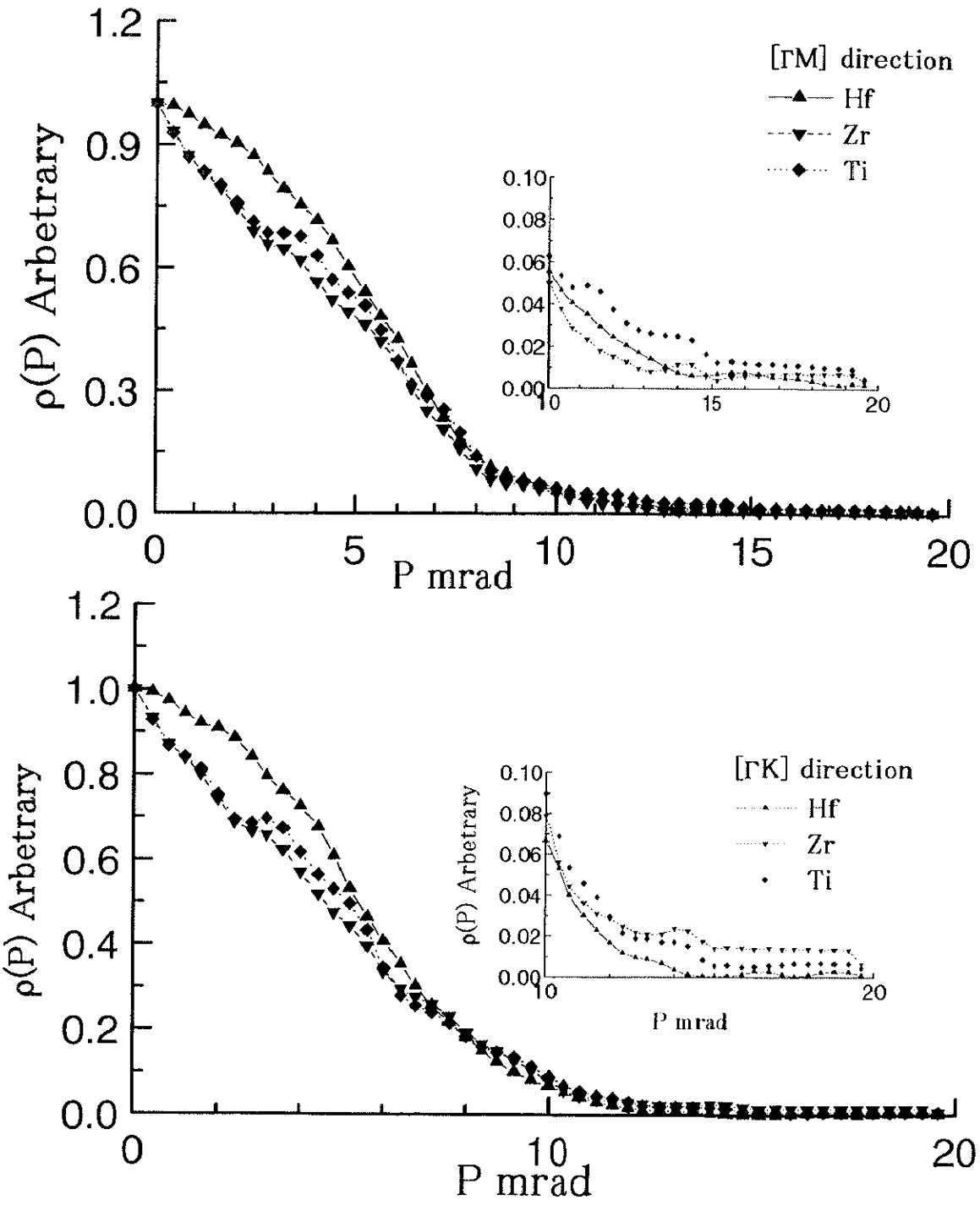


Figure 4.3.9 the electron momentum density of Ti, Zr and Hf in (a) ΓM and (b) ΓK directions.

Fermi surface boundaries are determined from the locus of $|\nabla\rho(P)|_{Max}$. Figure 4.3.10 shows the experimental Fermi radii for Ti, Zr and Hf along ΓMK and AHK planes normalized to the free electron Fermi radius of individual metals, respectively. The free electron Fermi radii of Ti (=7.300 mrad), Zr (=6.64 mrad) and Hf (=6.71 mrad) are taken as a unity. In ΓMK plane the angle is measured from ΓM direction, and in AHK plane it is measured from ΓK direction. In ΓMK plane the maximum deviations from the free electron Fermi radius for Ti, Zr and Hf are hesitating around ±25%, ±10% and –40%, respectively. In AHK plane the maximum deviations from the free electron Fermi radius for Ti is between ΓH and ΓA direction (about +10%), for Zr is near ΓH direction (about +25%) and for Hf is between ΓH and ΓA direction (about -25%). From these figures it can be noted that the free electron Fermi radii are very far from that obtained for Ti, Zr and Hf. In other words, their Fermi surfaces are strongly deviated from the free electron model.

### IV.3.2 Electron Momentum Density in the wave vector space n(k)

The electron density in wave vector space can be constructed using LCW folding procedure equation (2.4.1). Figures 4.3.11, 4.3.12 and 4.3.13 represent the contour maps of the cross sections of ΓMK up to AHK plane along c-axis. ΓMK is represented as plane number 1 and AHK is represented as plane number 5. These planes will be denoted as the sample's name and plane's number. The dark parts show the higher momentum density contributions. Figure 4.3.11 shows the contour map of the cross section of n(k) for Ti. Γ point shows a hole surface up to A point in Fig. Ti5. At H point two electron surfaces are observed. Figure 4.3.12 shows the contours of the cross sections of n(k) for Zr. In Fig. Zr1 a hole surface at Γ point is observed but its dimension is rather small than that of Ti. This hole surface doesn't change its behavior up to Fig. Zr5 at A point. Two electron surfaces are observed around H point in Fig Zr5. Figure 4.2.13 shows the contours of the cross section of n(k) for Hf. Figure Hf1 shows a hole surface at Γ point. It doesn't change its behavior to be an electron Hf5. Two electron surfaces at H point are shown in Fig.

Hf5. Figure 4.3.14 represents the electron density in the wave vector space in ΓAHK plane for Ti, Zr and Hf, respectively. A hole surface is running along Γ-A axis and two electron surfaces at H point are observed in Ti, Zr and Hf spectra.

The normalized n(k)% along the principal symmetry lines is obtained from equation (2.4.4). Figure 4.3.15 shows n(k)% from the present experiment of (a)Ti, (b) Zr and (c)Hf. The sharp lines represent the results obtained from a band structure calculation using APW method for Ti and Zr [4.3.8] and using the RAPW method for Hf [4.3.9]. The dotted lines show the results of band structure calculation using LCAO method for Ti, Zr and Hf [4.3.7]. The thickness of the bands are estimated by the statistical analysis using least square method (SALS). Table 4.3.2 shows the estimated values of the bands using least square method. The dimensions of Fermi sheets from APW and LCAO methods are used as input parameters. In Fig. 4.3.15a, for Ti, a hole surface around Γ-A axis in the 3$^{rd}$ and 4$^{th}$ bands and electron surfaces around H point at 5$^{th}$ and at 6$^{th}$ bands are observed. These results show agreement with APW method. For Zr, the hole surfaces around Γ-A axis at 3$^{rd}$ and 4$^{th}$ bands and the electron surfaces around H point in the 5$^{th}$ and 6$^{th}$ bands are observed. Similarly, the results of Zr show also an agreement with that obtained from APW method. For Hf, the main difference between the two band structure calculations is at A point. it shows an electron surface in LCAO method and hole surface in RAPW method. The present results show agreement with RAPW calculation at A point. Another difference, that H point shows two electron surfaces at 5$^{th}$ and 6$^{th}$ bands in RAPW method, while they are overlapped according to LCAO calculation. The present results show very closed two electron sheets around H point in HA direction at 5$^{th}$ and 6$^{th}$ band. In HL direction, there is an electron surface at 5$^{th}$ band, but it is stretched towards L point. As a result, we considered only the dimension's calculation of the 6$^{th}$ band electron surface. The calculation of the dimensions of the electron surface in the 5$^{th}$ and 6$^{th}$ bands will be affected because of that overlapping. The Fermi surface sheets can be calculated from the maximum of gradient of the momentum density n(k). Table 4.3.1 declares the calculated Fermi surface sheets' dimensions of Ti, Zr and Hf from the present work. The error estimation in determining the Fermi

surface using the reconstruction technique and LCW folding procedures exceeds ± 0.02 a.u. in all directions. The dimensions of the hole surface along Γ-A axis are found to be related to the lattice constants of Ti and Zr.

| Fermi surface | direction | Ti (a.u.) | Zr (a.u.) | Hf (a.u) |
|---|---|---|---|---|
| $(\Gamma\text{-}A)_3^-$ | ΓM | 0.15±0.02 | 0.13±0.02 | 0.155±0.02 |
| | ΓK | 0.16±0.02 | 0.135±0.02 | 0.185±0.02 |
| $(\Gamma\text{-}A)_4^-$ | ΓM | 0.16±0.02 | 0.13±0.02 | 0.145±0.02 |
| | ΓK | 0.165±0.02 | 0.14±0.02 | 0.165±0.02 |
| $H_5^+$ | HL | 0.17±0.02 | -- | -- |
| | HK | 0.13±0.02 | -- | -- |
| $H_6^+$ | HL | 0.18±0.02 | 0.165±0.02 | 0.165±0.02 |
| | HK | 0.14±0.02 | 0.145±0.02 | 0.145±0.02 |

Table 4.3.1 The experimental values of the Fermi surface dimensions in a.u. for Ti, Zr and Hf. The experimental error of determining the dimensions is 0.02 a.u..

The electron surface at 5$^{th}$ and 6$^{th}$ band are overlapped in both Zr and Hf, so that we considered only the dimensions of the 6$^{th}$ band. The electron surface at 5$^{th}$ band has large uncertainty in its dimension for Ti, Zr and Hf. This attributed to the experimental resolution in which, when two or more Fermi sheets are overlapped within the experimental resolution, their dimensions using the maximum in the gradient can not be determined accurately. From the above mentioned results it can be concluded that Ti, Zr and Hf have the same features of the Fermi surface sheets namely a hole surface around Γ-A axis in the 3$^{rd}$ and 4$^{th}$ bands, and two electron surfaces at 5$^{th}$ and 6$^{th}$ bands around H point.

| | Ti APW | Ti LCAO | Zr APW | Zr LCAO | Hf APW | HfLCAO |
|---|---|---|---|---|---|---|
| 3rd band $n_3$ | 97.7±4.33 | 95.5±4.8 | 96.99±1.7 | 98.6±1.18 | 93.1±1.6 | 93.6±2.74 |
| 4th band $n_4$ | 96.7±6.00 | 99.9±4.95 | 99.3±1.15 | 98.1±1.69 | 97.8±1.5 | 98.1±2.22 |
| 5th band $n_5$ | 101.8±9.4 | 100.6±1.0 | 102.5±3.3 | 100.7±3.5 | 101.4±1.4 | 101.6±2.6 |
| 6th band $n_6$ | 114.5±9.80 | 11.3±9.36 | 107.6±2.4 | 107±2.21 | 106.4±2.2 | 107.0±4.0 |

Table 4.3.2 the obtained fitting parameters using least square-fitting program for Ti, Zr and Hf. APW and LCAO represent the used input dimensions are from the bands from APW and LCAO methods, respectively. The values of the bands are represented with its uncertainty of calculation.

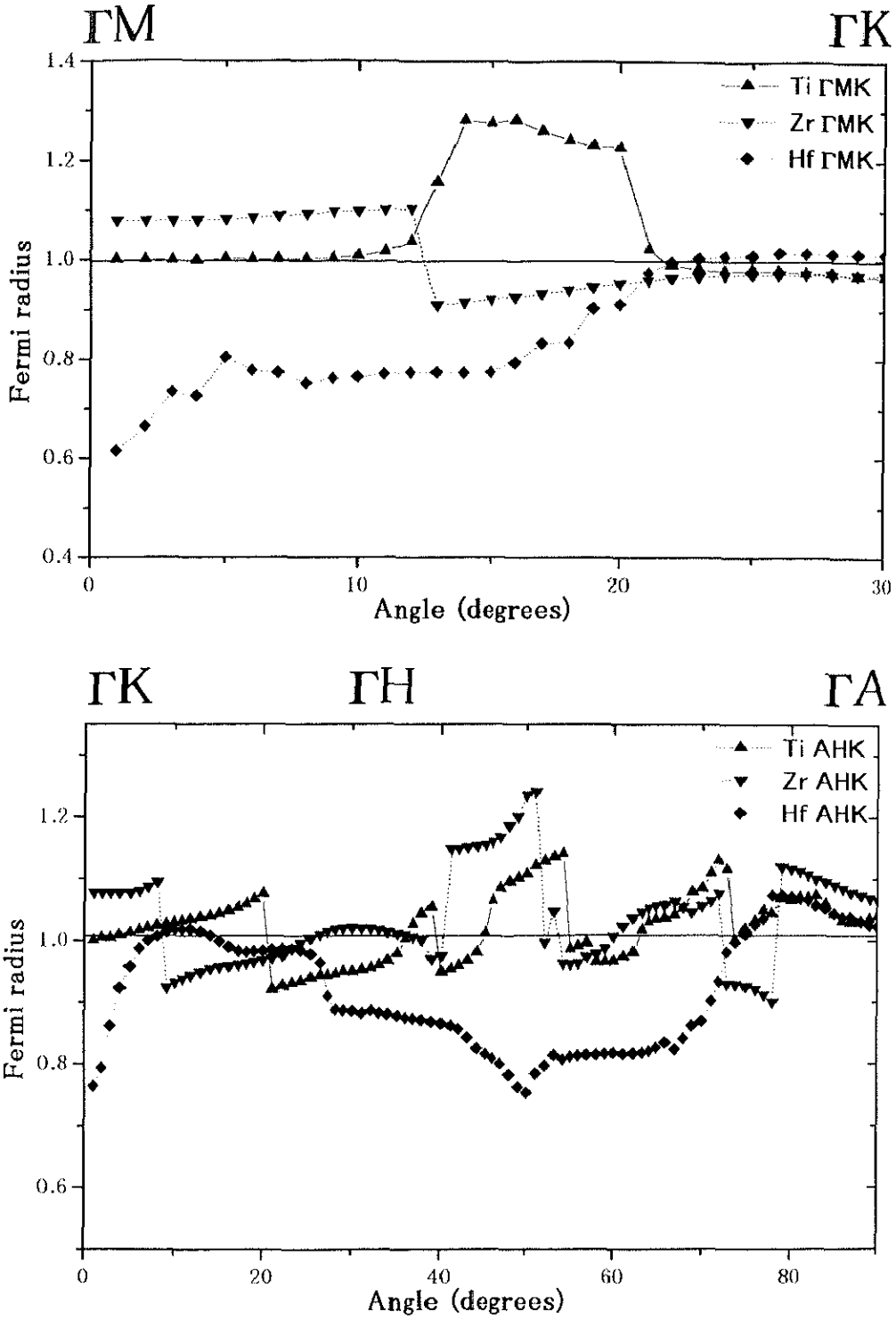


Figure 4.3.10 the normalized Fermi radius of Ti, Zr and Hf in ΓMK and AHK planes, respectively.

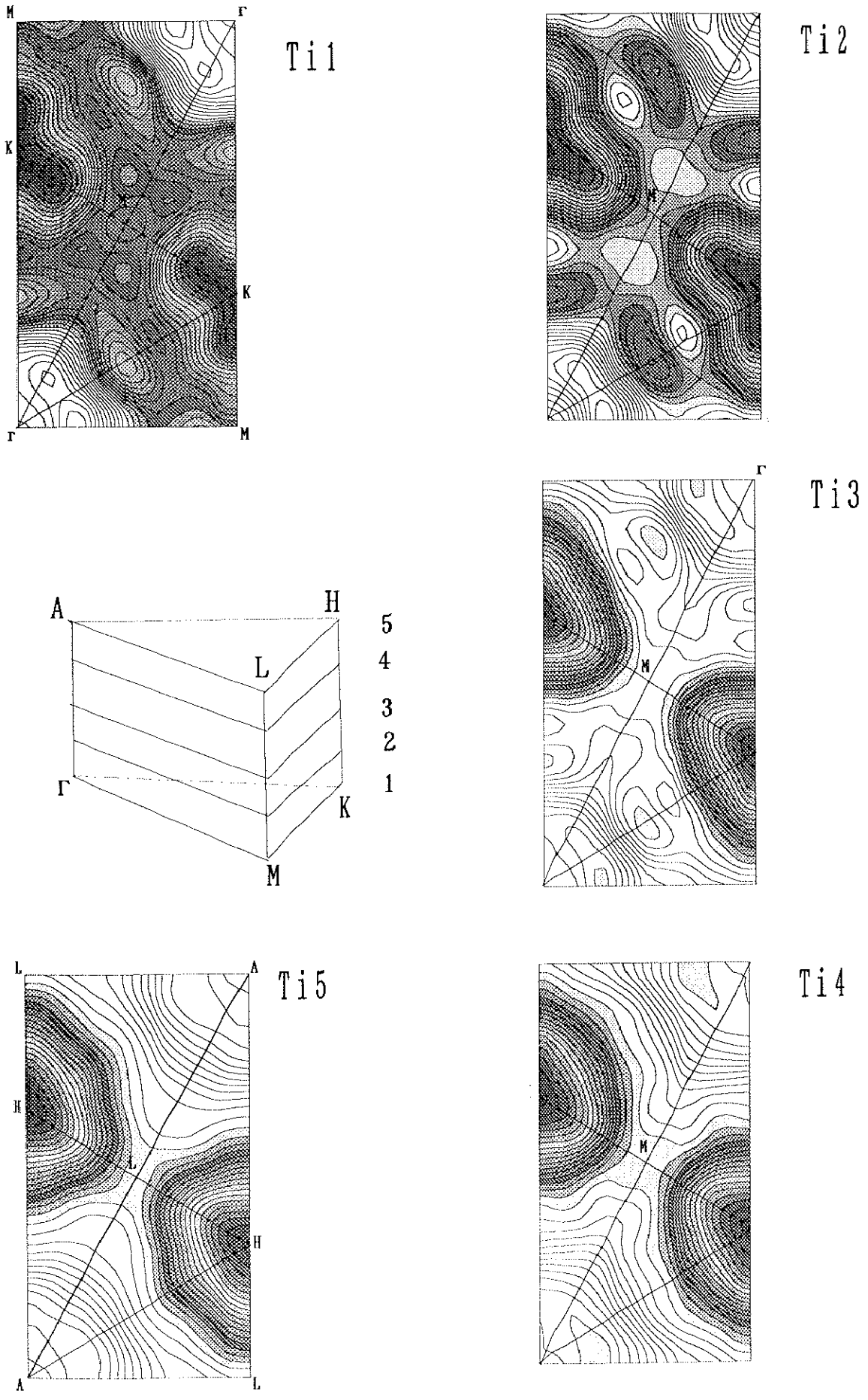


Figure 4.3.11 n(k) of Ti normal to c-direction in 5 cross sections from ΓMK to AHL planes, with the 1/24$^{th}$ part of the Brillouin zone of HCP structure.

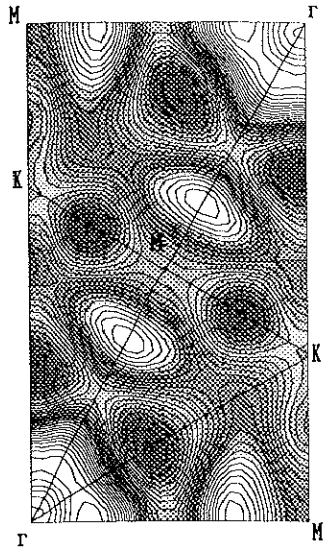


Zr1

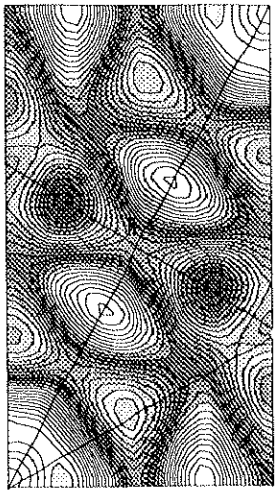

Zr2

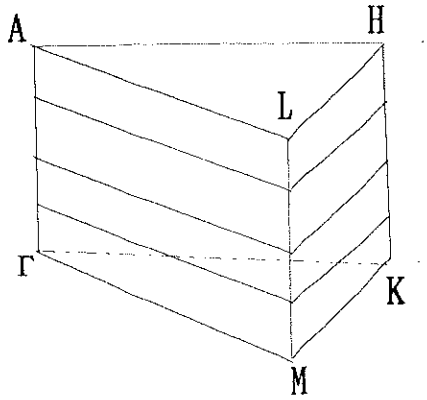


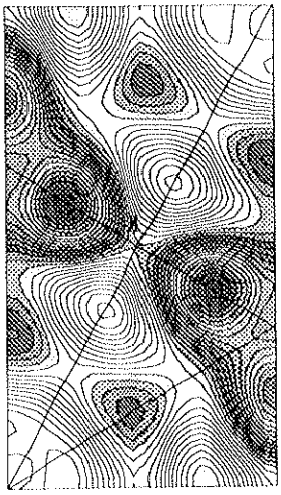

Zr3

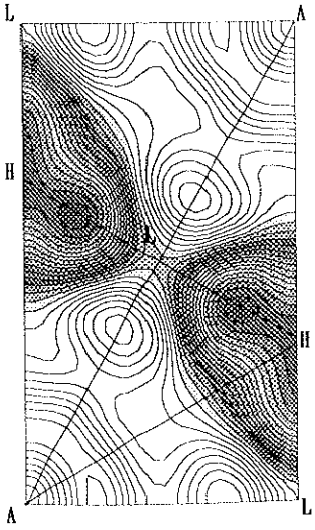


Zr5

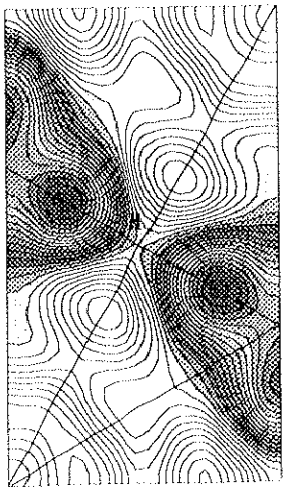

Zr4

Figure 4.3.12 n(k) of Zr normal to c-direction in 5 cross sections from ΓMK to AHL planes, with the 1/24$^{th}$ part of the Brillouin zone of HCP structure.

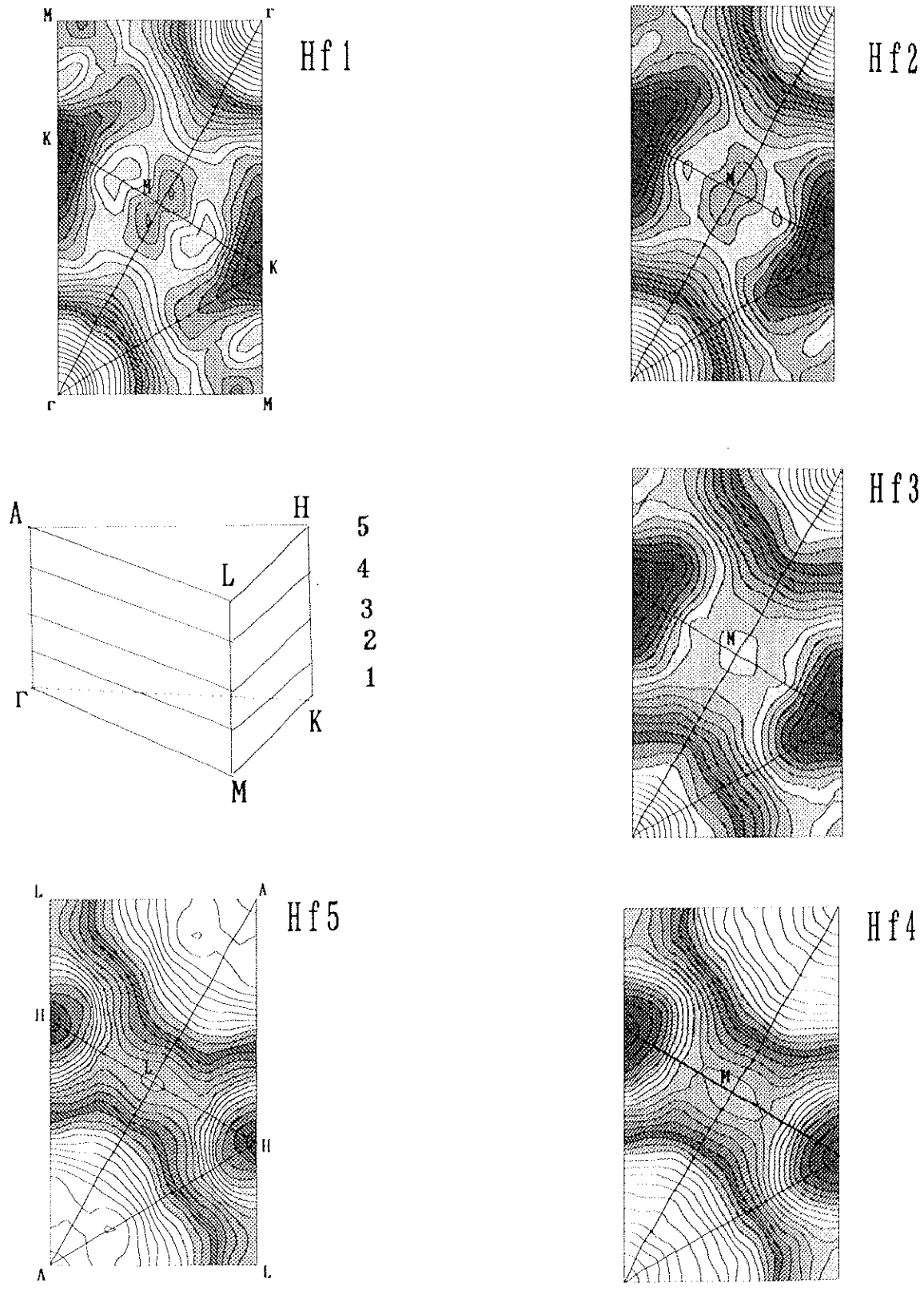


Figure 4.3.13 n(k) of Hf normal to c-direction in 5 cross sections from ΓMK to AHL planes, with the 1/24$^{th}$ part of the Brillouin zone of HCP structure.

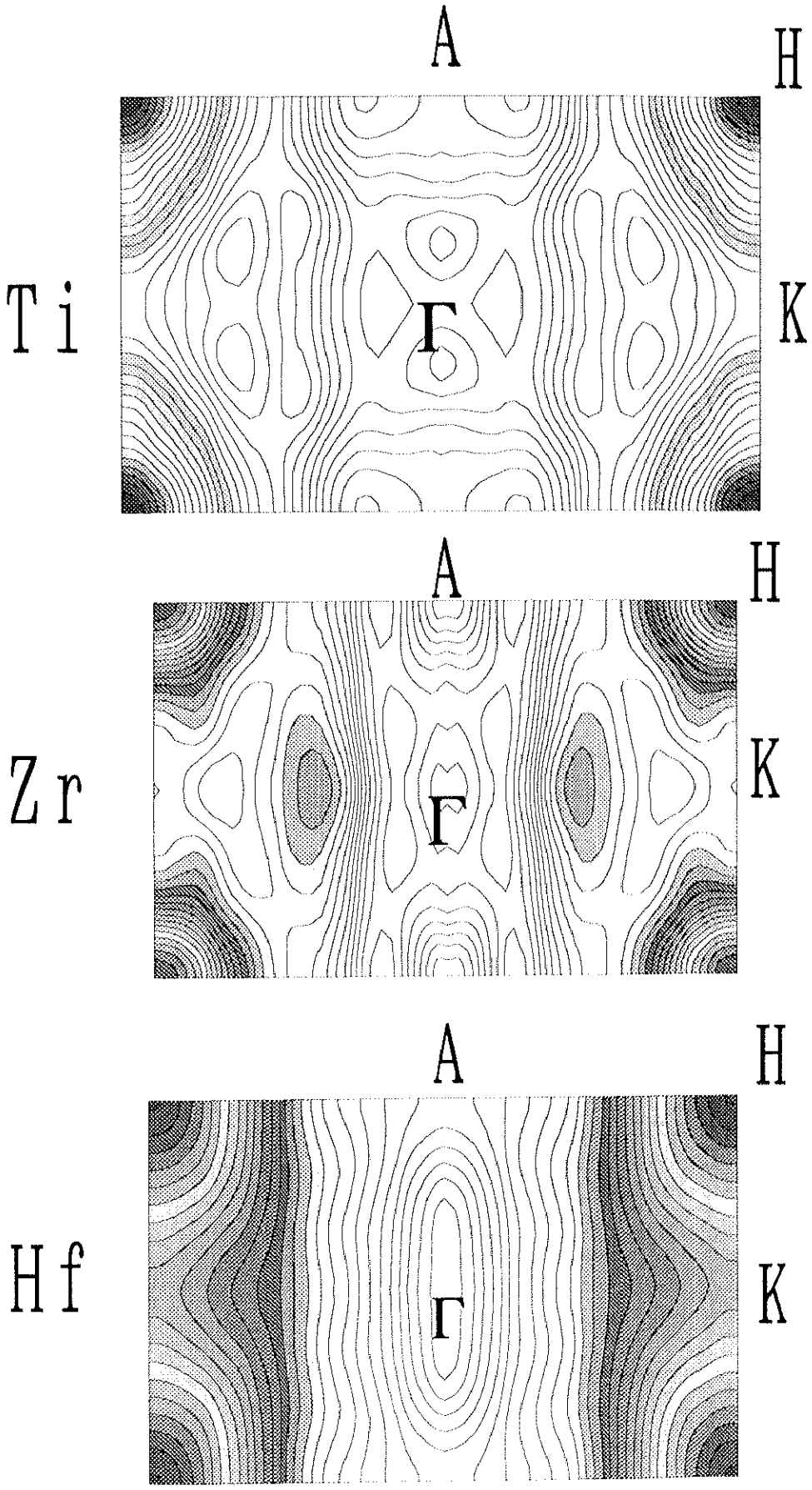


Figure 4.3.14 n(k) of Ti, Zr and Hf in ΓAHK plane. The dark parts show the higher electron density

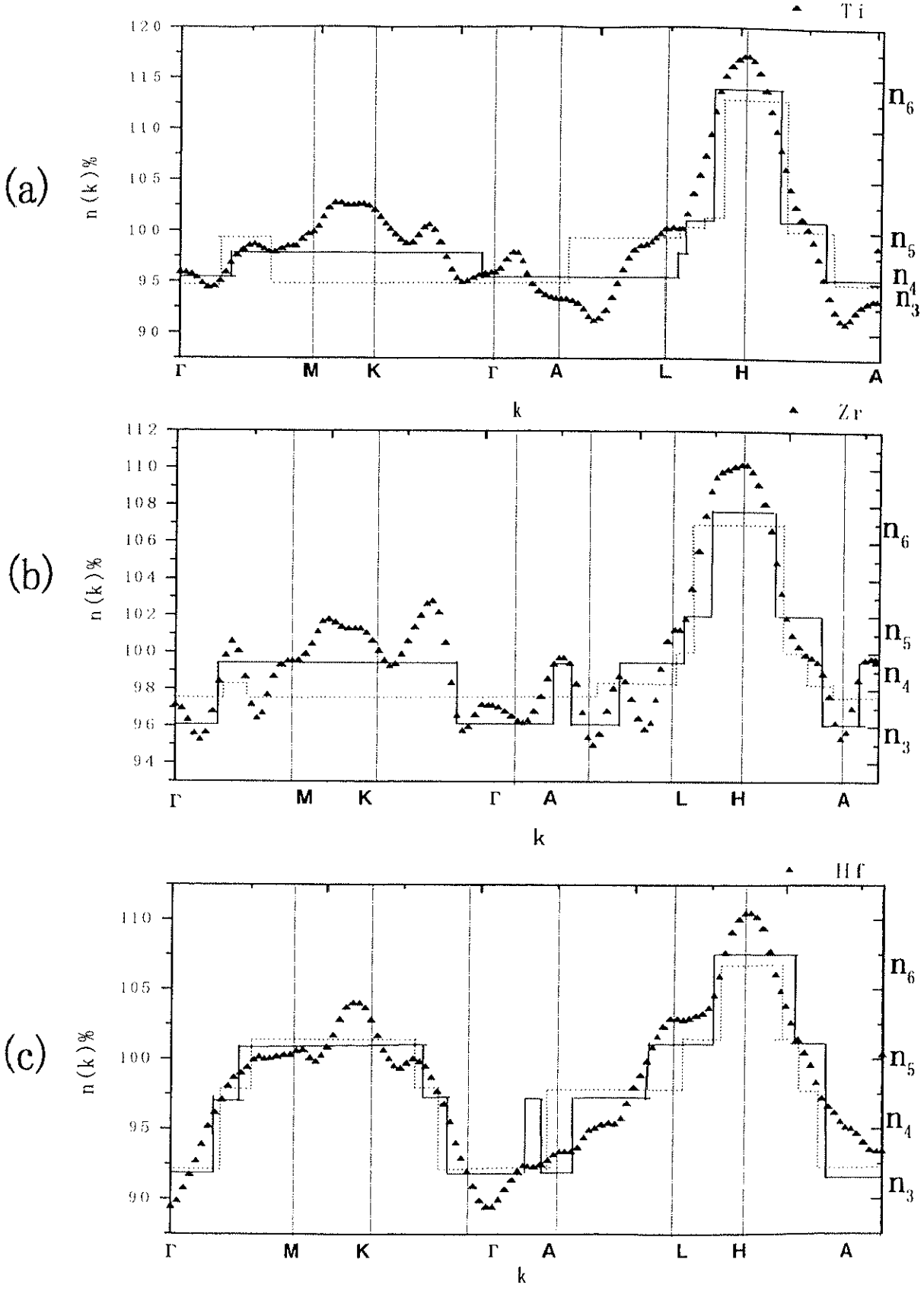


Figure 4.3.15 the normalized electron density in the wave vector space n(k)% for (a) Ti, (b) Zr and (c) Hf. The sharp and the dotted lines show the results of the band structure calculation using the APW and LCAO methods, respectively.

## IV.4 FCC structure metals of group VIII Rhodium Rh and Iridium Ir

The electronic properties of FCC transition metals Rh and Ir are dominated by their tightly bounded d-electrons [4.4.1]. In 1966, Coleridge [4.4.2] has performed Fermi surface of Rh using dH-vA measurements, then he proposed the Fermi surface of Rh by employing the rigid-band model [4.4.3] using the band structure of Ni. The Fermi surface of Rh calculated by this method would consist of two large closed electron surfaces at Γ point, two close hole surfaces at X point and one small closed hole surface at L point. Figure 4.4.1 represents the Fermi surface proposed by their model. Andersen and Mackintosh [4.4.4] have performed the RAPW band structure calculations of Rh and Ir. They have found that, the calculated Fermi surface of Rh has the same features that had been suggested by Coleridge [4.4.2]. For Ir, their calculation show that its Fermi surface consists of; two large electron surfaces around Γ point, and two close hole surfaces around X point.

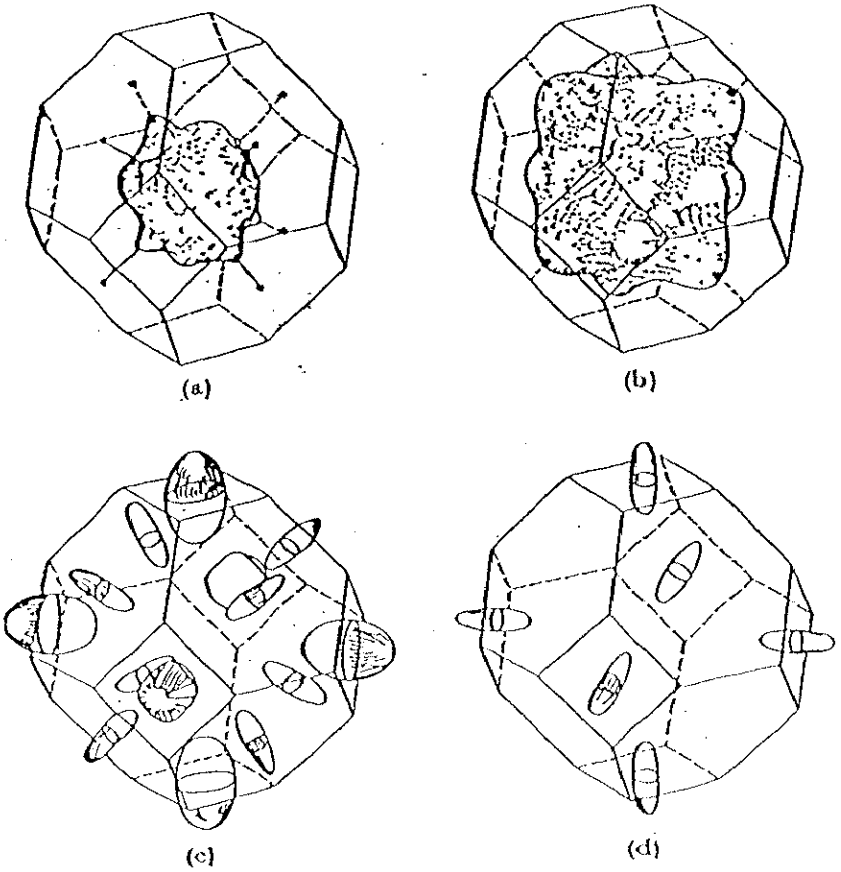


Figure 4.4.1 The Fermi surface of Rh proposed by Coleridge [4.4.2] showing (a) and (b) regions of electrons and (c) and (d) pockets of holes.

The difference between Rh and Ir from their RAPW calculations is that the small pocket of hole at L point has vanished in the Fermi surface of Ir. Following this calculations, two dH-vA measurements have been carried out by Grodski et al [4.4.5] and Hornfeldt [4.4.6]. They have measured the cross sections of the two pockets of holes around X point. Papaconstantopolous [4.4.7] has performed the band structure calculation of Rh and Ir using LCAO method. These results have agreed with that obtained by RAPW method [4.4.3], while the sheets dimensions are rather different. The motivation of studying both of Rh and Ir using the 2D-ACAR bases on the following two reasons. The first is to compare the Fermi surface of Rh and Ir with each other in one hand and with that obtained theoretically in the other. The second is to check the applicability of the present 2D-ACAR system in measuring the high-density materials Ir in which these material has a high absorption coefficient to γ-rays.

### IV.4.1 2D-ACAR specter and the electron density in the momentum space

The electron density in momentum space is carried out using a pair of 256 detectors 2D-ACAR set-up. Figure 4.4.2 shows 2D-ACAR spectra as an isometric view of (a) Rh and (b) Ir as two extreme deviation angles, $0^{\circ}$ and $45^{\circ}$, on the projection of [001] direction. The d-like character can be seen as a sharp peak in the center of the spectra. This sharpness observes in Rh spectra more than that of Ir. This is attributed to the high absorption of γ-rays of Ir. Since the density of Ir is greater than 25 gm/Cm$^3$, while the density of Rh is 12.42 gm/Cm$^3$. This leads to that, the obtained γ-rays from the annihilation process, in Ir, undergo attenuation with small angles and collected in the detectors from which the accidental coincidence events become higher than that expected. Consequently, in the Ir spectra, the pair photons collected at the detectors simultaneously with small angles (or with low momentum) in the sampled momentum density becomes lower than that expected. Furthermore, due to the high absorption of Ir to γ-rays spectra, the count rate become small, therefore, the background become larger than that of Rh see Fig. 4.4.3. Figure 4.4.4 represents the contour map of $\rho(\mathbf{P})$ for

(a) Rh and (b) Ir in (001), (110) and (111) planes respectively. This figure shows the same feature in the center of spectra, i.e., they are more brooded in Ir than that of Rh. This is attributed to the difference in the electronic structure of both Rh($4d^8s$) and Ir ($5d^9$-). Figure 4.4.5 shows the normalized $\rho(P)$ for Rh and Ir in one dimension as [110] and [001], respectively. This Figure shows that Ir spectra are much broader than Rh ones, and the contribution of the Ir spectra over the 15 mrad are larger than that of Rh. In view of HMC's, Figs 4.4.6 and 4.4.7 show the enlarged spectra up to 10% from their maximum in (001), (100), (110) and (111) planes for Rh and Ir, respectively. The nearest neighbor reciprocal lattice point is, $G_{111}$, at (6.1 mrad) for Rh and at (6.3 mrad) for Ir, these values are inside Fermi surface for Rh ($P_F$=10.38 mrad) and Ir($P_F$ =10.29 mrad), respectively. This result emphasizes that the Fermi surface of Rh and Ir are affected by a strong signal d-like, which occur in the higher Brillouin zones.

Fermi radii of Rh and Ir are determined from the locus of $|\nabla\rho(P)|_{Max}$. Figure 4.4.8 shows the experimental Fermi radii along (100) plane normalized to the free electron Fermi radius of Rh and Ir, respectively. The free electron Fermi radii of Rh and Ir are taken as a unity. As it apparent, the maximum deviations are hesitating from the free electron Fermi radius around ±10% and ±15% for Rh and Ir, respectively. It can be noted that, the Fermi radii of Rh and Ir are far from that obtained from the free electron ones. Consequently, the Fermi surfaces of both Rh and Ir are deviated from the free electron model.

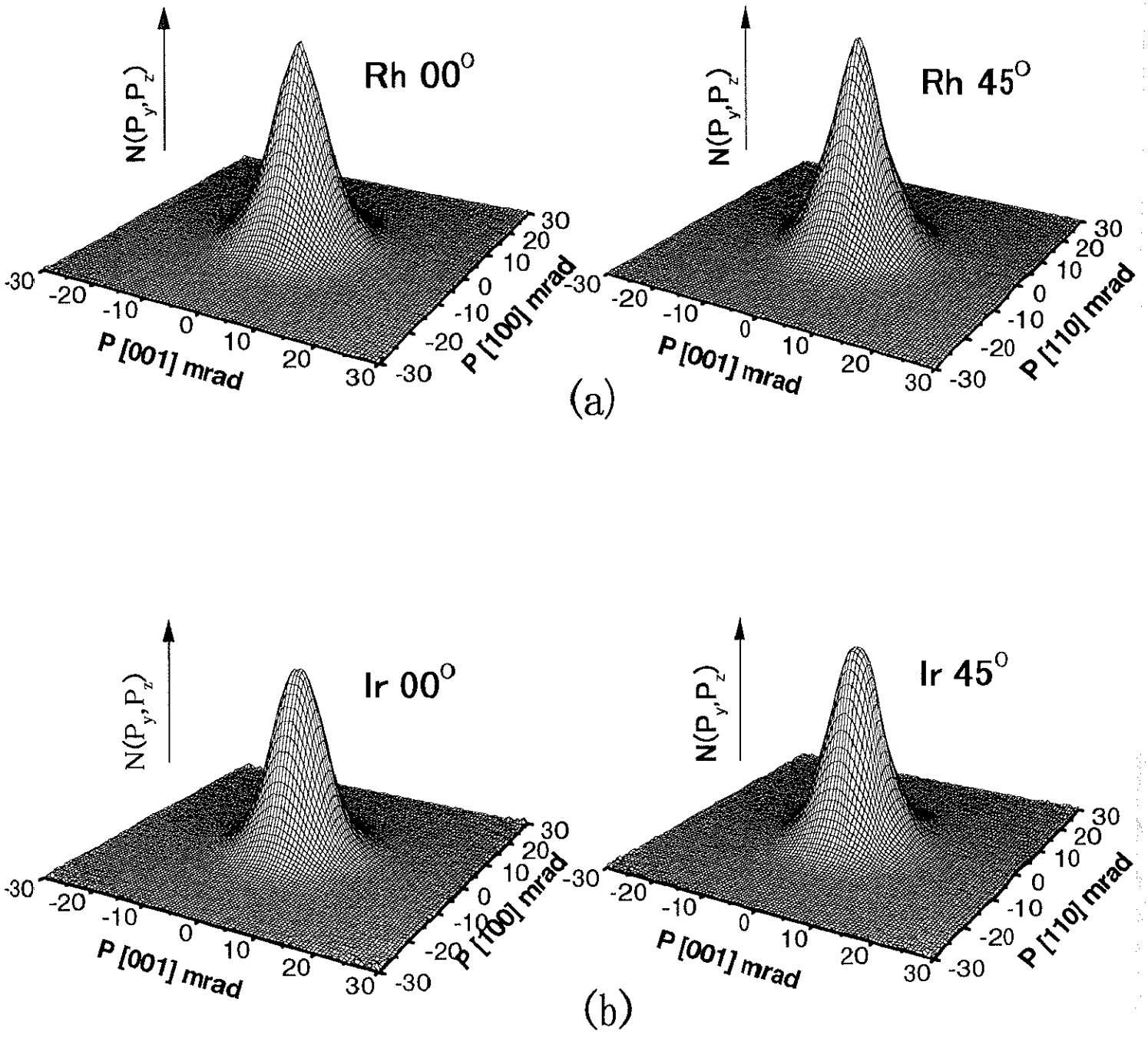


Figure 4.4.2 the 2D-ACAR spectra of (a)Rh and (b)Ir on two extreme angles 0° and 30°. The spectra represented as isometric view

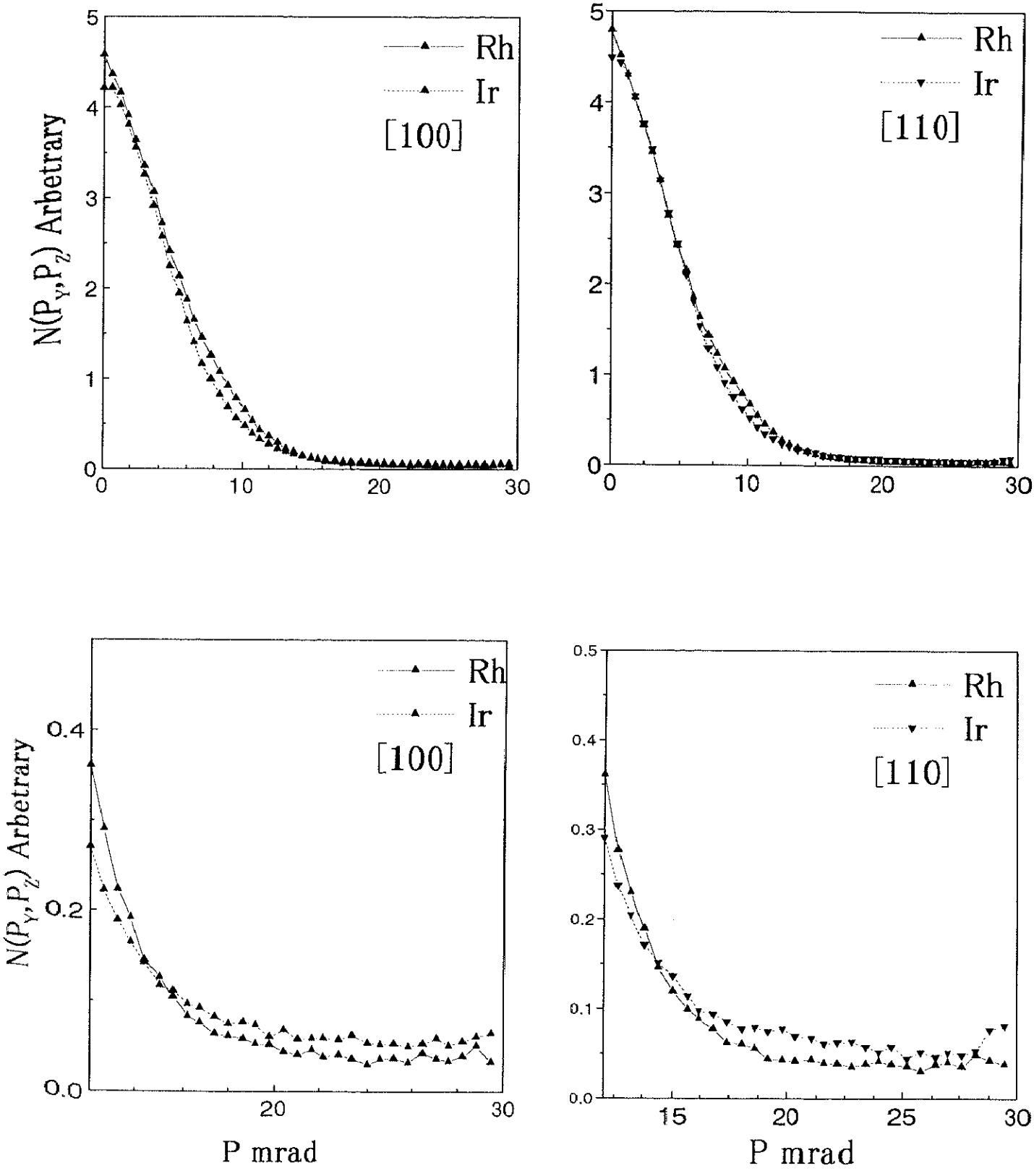


Figure 4.4.3 the spectra of Rh and Ir in [100] and [110] directions. The background of Ir spectra is much higher than that of Rh spectra.

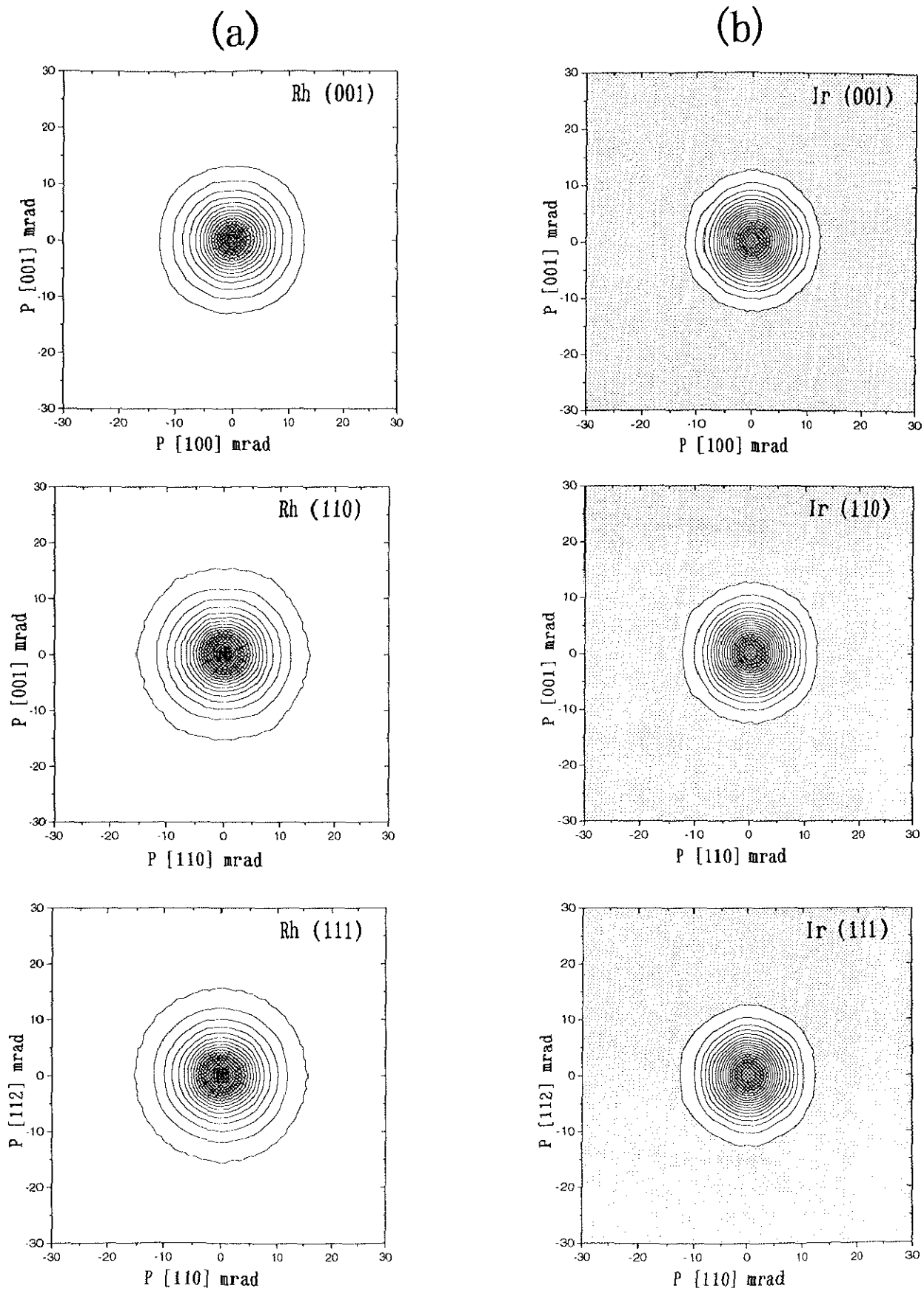


Figure 4.4.4 the electron density in the momentum space $\rho(p)$ of (a) Rh and (b) Ir in (001), (110) and (111) planes, respectively, as a contour map.

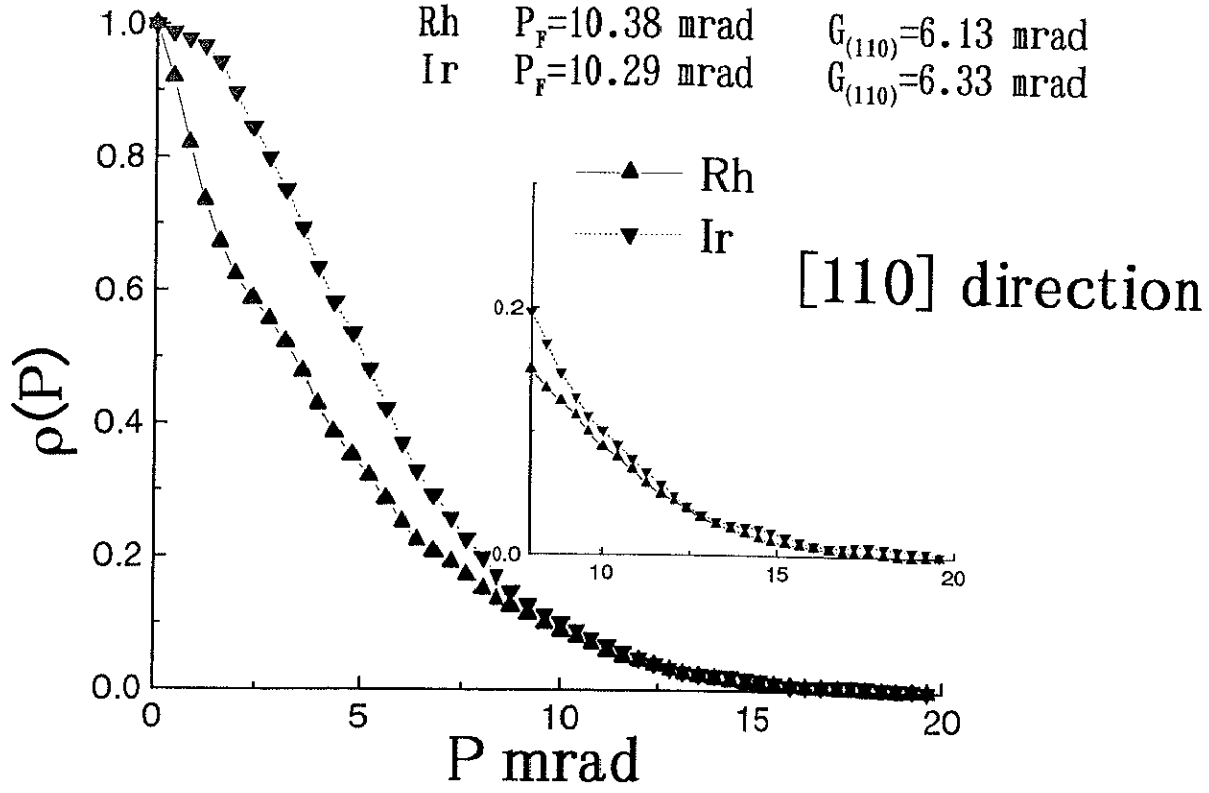


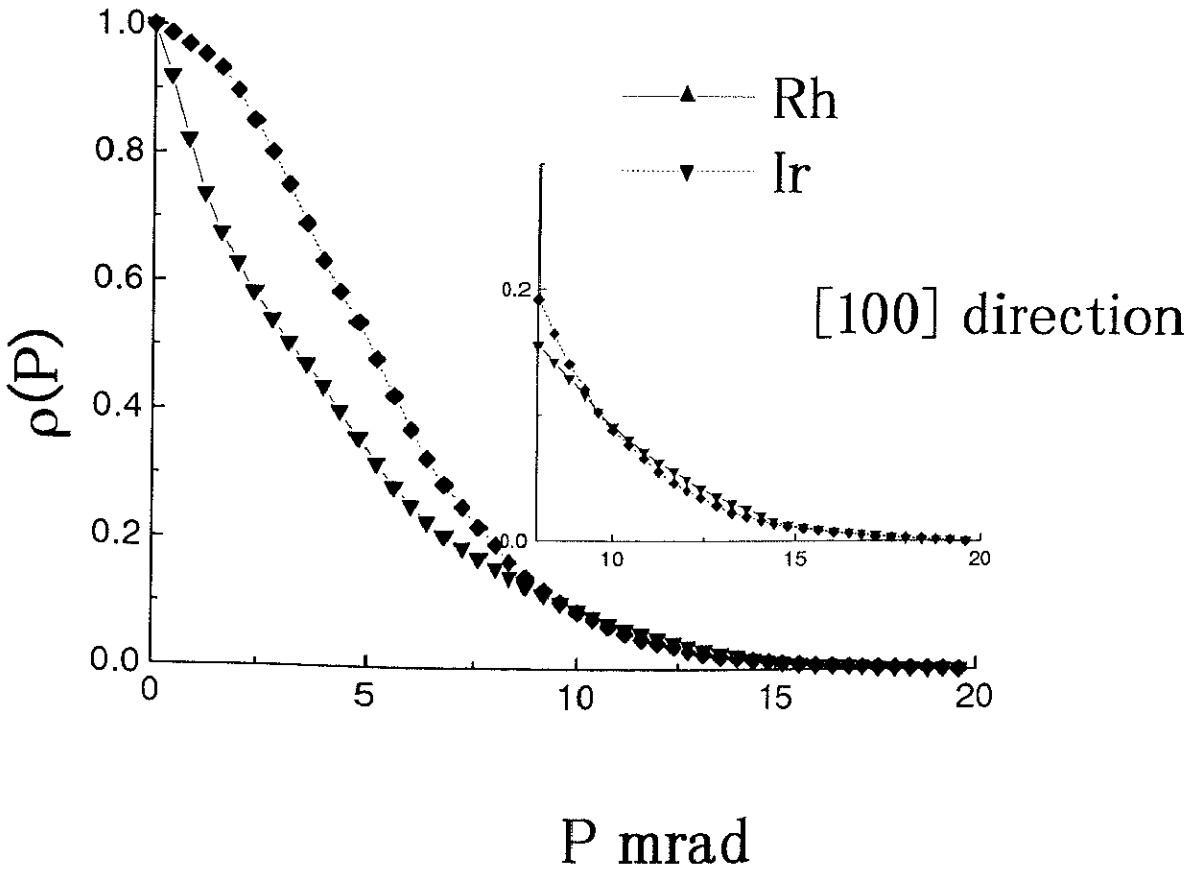


Figure 4.4.5 the electron density in the momentum space of Rh and Ir in [110] and [100] directions, respectively. Fermi momentum and the reciprocal lattice point in [110] direction of both Rh and Ir are represented in the same figure

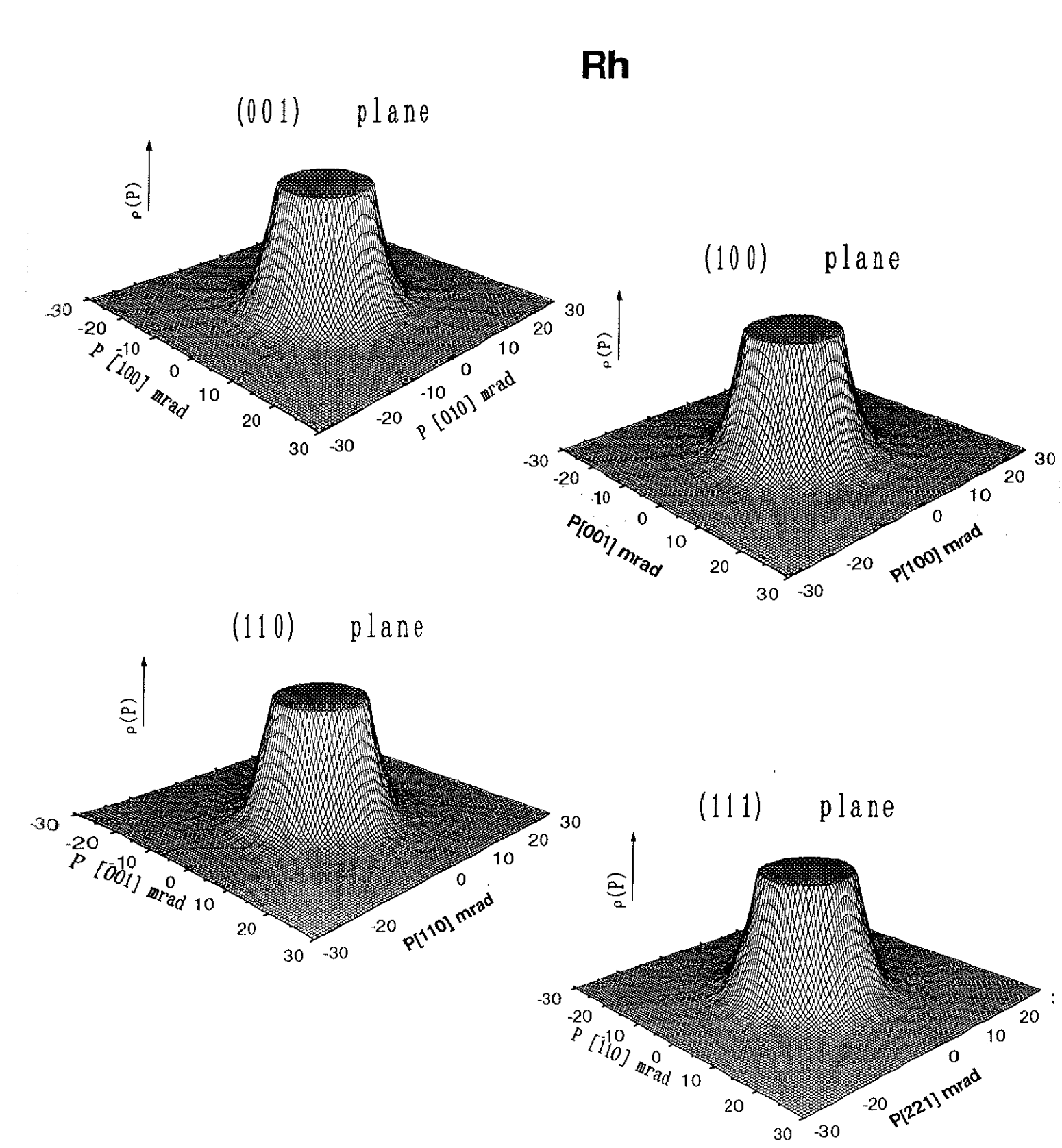


Figure 4.4.6 the enlarged ρ(P) spectra of Rh up to 10% from their maxima in (001), (100), (110) and (111) planes respectively.

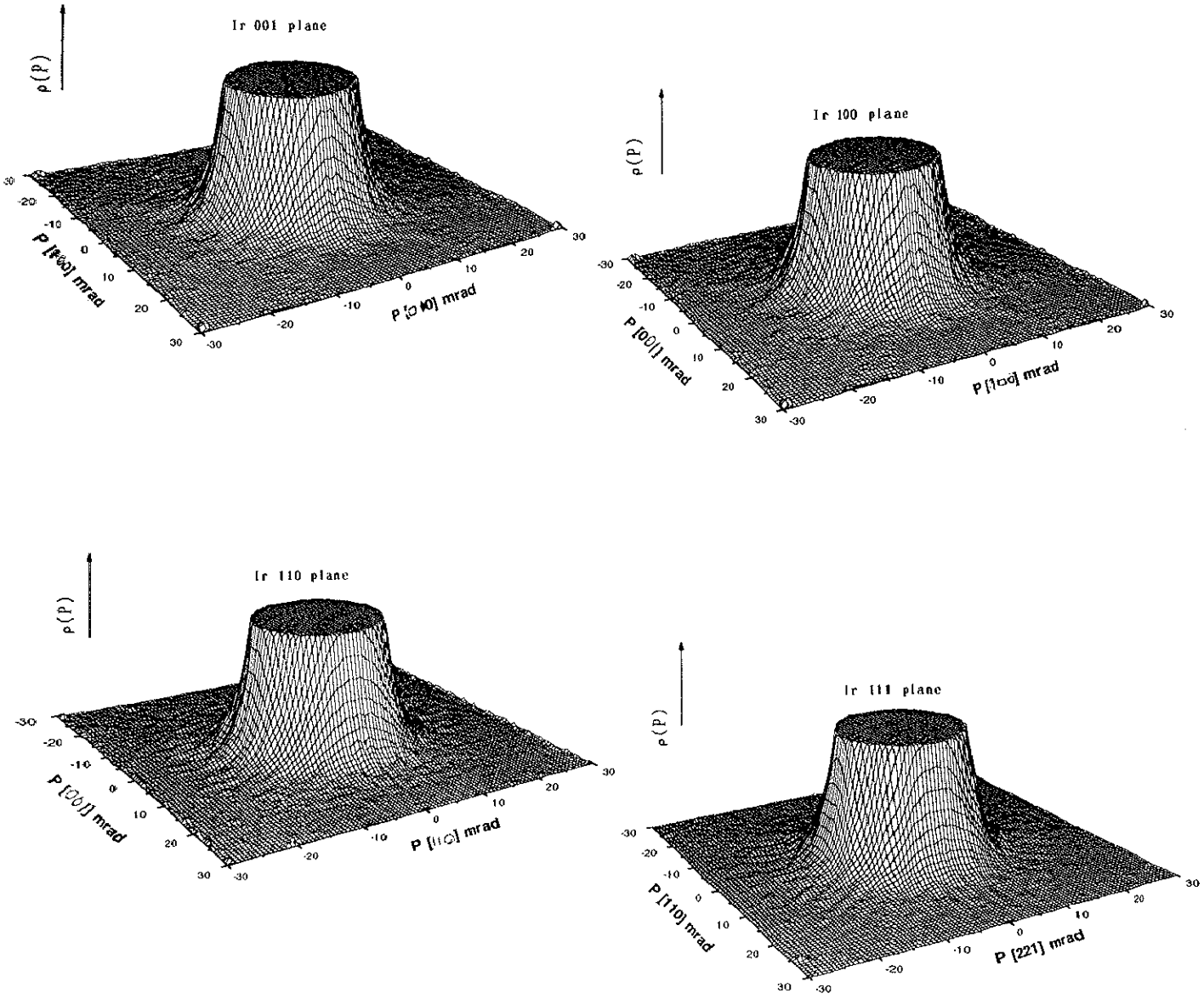


Figure 4.4.7 the enlarged ρ(P) spectra of Ir up to 10% from their maxima in (001), (100), (110) and (111) planes respectively.

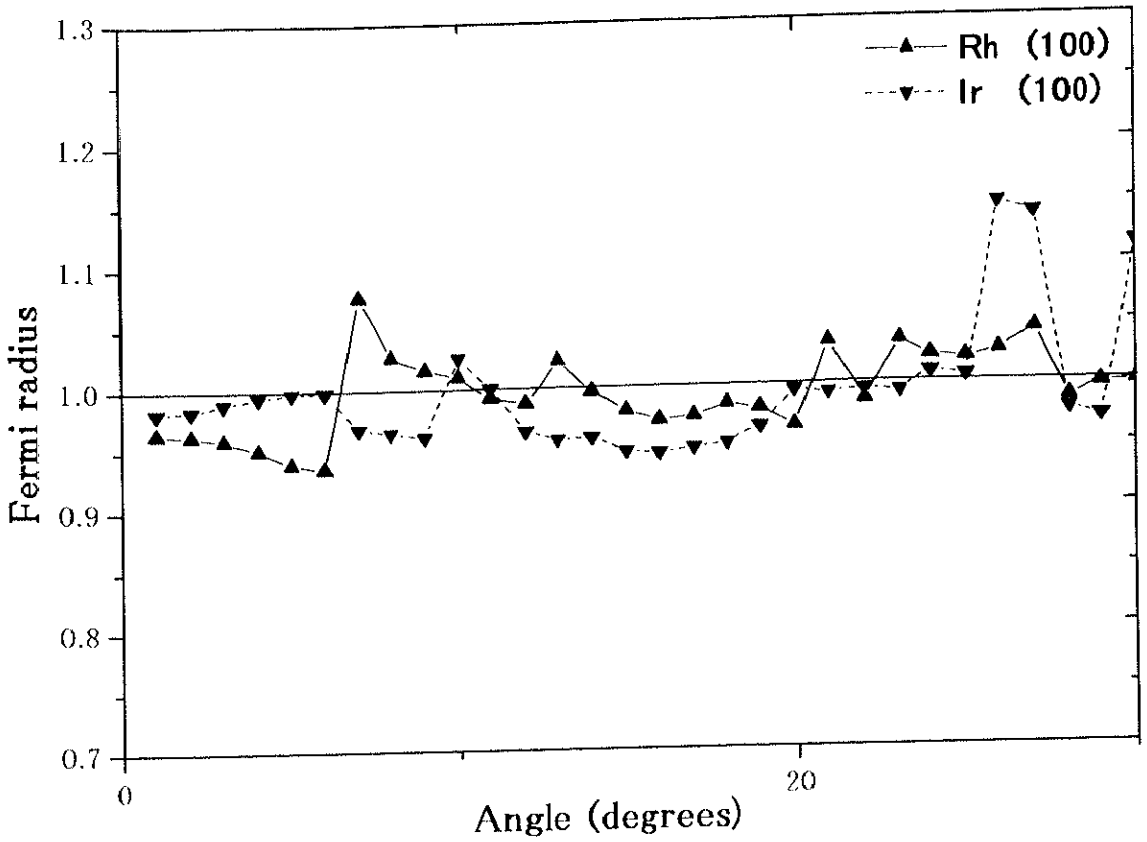


Figure 4.4.8 the normalized Fermi radius of Rh and Ir in (100) plane.

### IV.4.2 Electron density in the wave vector space n(k)

LCW folding procedure was used to reduce the electron density in a momentum space ρ(P) to the electron density in a wave vector space n(k), restricting Fermi surface features in the first Brillouin zone. Figures 4.4.9a and b show the obtained results of Rh and Ir, respectively, as divided into 3 planes parallel to the (001) plane. LCW01, LCW02 and LCW03 represent the (001) plane passing through Γ point, L point and X point, respectively. The dark parts show higher density region and the distribution are shown as a contour map in a step of 2.5% of the peak height. Figure RhLCW01 show high-density electron parts at Γ point and hole surface at X point. The high-density parts are crossing at Γ point, which indicate that there are two electron surfaces and they are partially overlapped. The same features as for Rh around Γ and X points are observed in Ir LCW01. The sizes of the two electron sheets and the hole surface are rather different in Rh and Ir. In Rh a hole surface is observed in Fig LCW02 around L point, while there is no Fermi surface feature at Ir LCW02 at the same point. In Fig Rh LCW03 and Ir LCW03 lower momentum density at X point appears comparing with its surrounding. This testifies the existence of closed two hole surfaces around X point. From the above mentioned results, we can conclude that Fermi surfaces of both Rh and Ir have the same feature at Γ point as two large closed electron surfaces and at X point as two closed hole surfaces. For Rh there is an additional hole surface at L point. This is due to the difference of the electronic structure of Rh and Ir. Figure 4.4.10a shows the obtained n(k)% for Rh (equation (2.4.4)) from the present experiment along different symmetry lines. The sharp and the dotted lines show the band structure calculation obtained using RAPW method [4.4.4] and LCAO method, respectively. The thickness of the bands are estimated by the statistical analysis using least square method (SALS). Using Least square method we could estimate the bands' occupation. The dimensions of Fermi sheets from APW and LCAO methods are used as input parameters. Table 4.4.1 shows the estimated values of the bands using least square method. In Fig. 4.4.10a two electron surfaces at Γ point in $4^{th}$ and $5^{th}$ bands, two hole surfaces at X point in $2^{nd}$ and $3^{rd}$ bands and one small hole surface at L point is observed. The present results, of Rh, show qualitative

**agreement with that obtained from the RAPW method. Figure 4.4.10b shows n(k)% for Ir from the present measurement along different symmetry lines. The sharp and the dotted lines show the results of the band structure calculations using RAPW method [4.4.4], and LCAO method. These figure shows two electron surfaces at Γ point in 4th and 5th bands and two hole surfaces at X point in 2nd and 3rd bands. The difference between Fermi surfaces of Rh and Ir is that the hole surface at L point in the 2nd band is vanished in Ir spectra.**

| | Rh APW | Rh LCAO | Ir APW | Ir LCAO |
|---|---|---|---|---|
| 2nd band $n_2$ | 96.2±2.8 | 95.5±3.6 | 99.5±3.6 | 99.8±2.7 |
| 3rd band $n_3$ | 97.3±3.0 | 97.6±3.6 | 99.90±2.8 | 100.2±3.4 |
| 4th band $n_4$ | 103.7±3.37 | 102.4±2.3 | 101.4±2.3 | 101.2±2.4 |
| 5th band $n_5$ | 113.7±3.48 | 111.2±4.32 | 102.36±2.6 | 102.0±2.3 |

Table 4.4.1 the obtained fitting parameters using least square-fitting program, for Rh and Ir. APW and LCAO represent the used input dimensions are from the bands from APW and LCAO methods, respectively. The values of the bands are represented with its uncertainty of calculation.

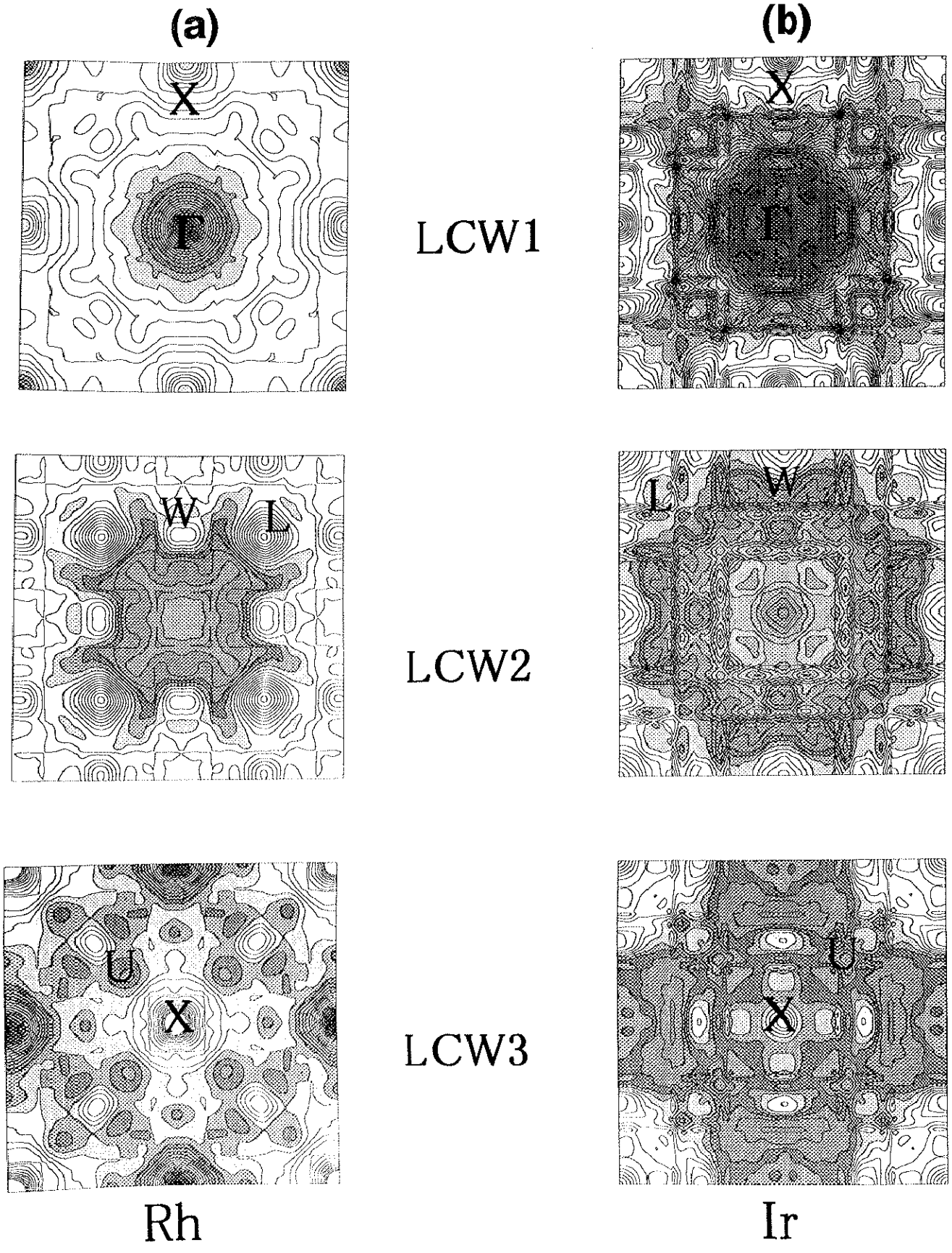


Figure 4.4.9 the contours of the electron density in the wave vector space of Rh and Ir normal to the c-direction and pssing through Γ, L, and X points, respectively. The dark parts show the higher electron density

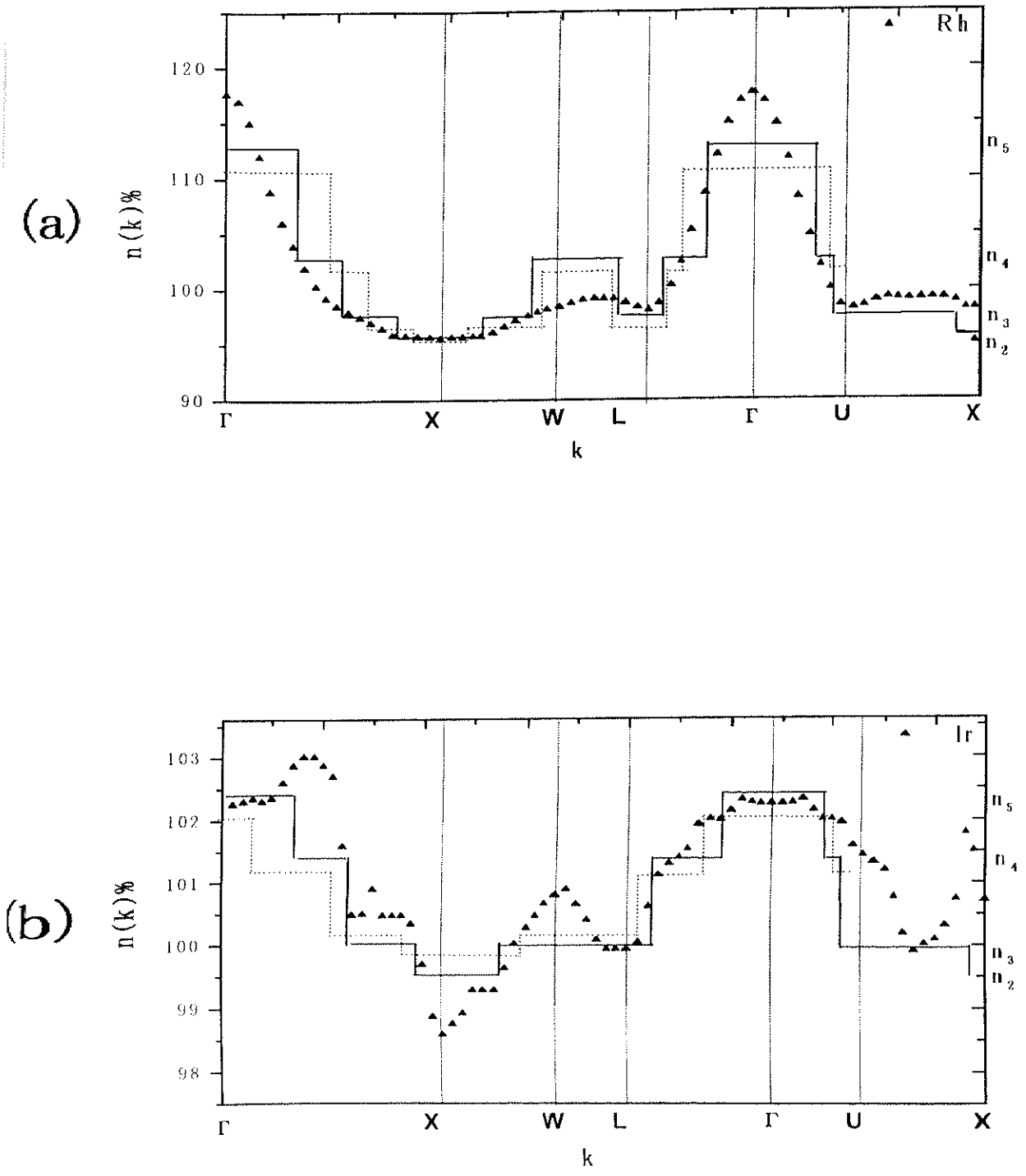


Figure 4.4.10 the normalized electron density in the wave vector space n(k)% for (a) Rh and (b) Ir.The sharp and the dotted lines show the results of the band structure calculation using the RAPW and LCAO methods, respectively

## IV.5 The non-cuprate layered perovskite superconductor $Sr_2RuO_4$

The non-cuprate layered perovskite compound $Sr_2RuO_4$ has been discovered by Maeno et al [4.5.1], and it was found to be super-conducting below Tc ~ 1K. Following this discovery, several workers [4.5.2- 4.5.6] have studied different characteristics and proprieties of $Sr_2RuO_4$. It became well known that, the crystal structure of $Sr_2RuO_4$ is $K_2NiF_4$ type with I4/mmm space group and its lattice constants are, a=b=3.8609 Å and c=12.729 Å, at 100K[4.5.2]. Figure 4.5.1 represents (a) schematic crystal structure of $Sr_2RuO_4$, and (b) the directions of the tetragonal principal axes. In 1995, T. Oguchi [4.5.7] has calculated the band structure of $Sr_2RuO_4$ using the LDA to density fractional theory. The calculated Fermi surface using this model shows three sheets; two of them are electron cylinders around Λ line and the remaining one is hole cylinder centered on X point. As well, he has concluded that there is a large hybridization between Ru d-state and O p-state. However, this new discovery has motivated us to study the momentum densities and the Fermi surface of $Sr_2RuO_4$.

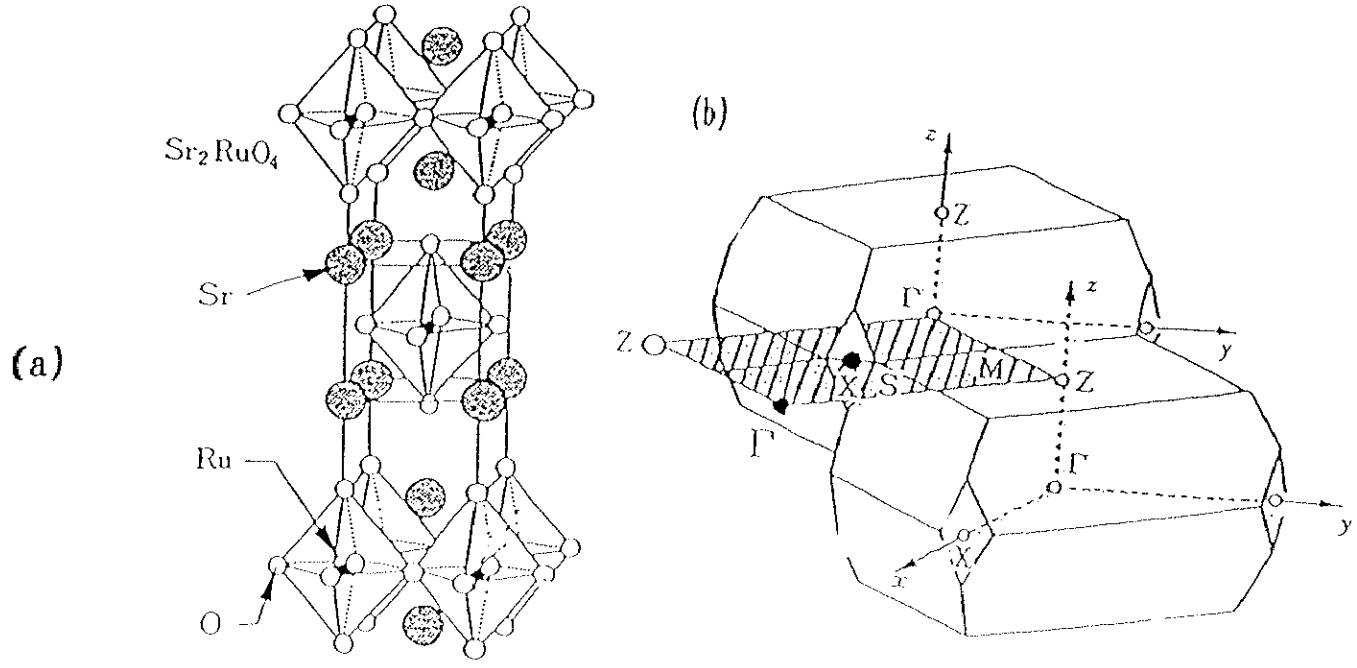


Figure 4.5.1 schematic representation of the $Sr_2RuO_4$, and (b) the directions of the tetragonal principal axis.

In the present work, 30 mrad x 30 mrad 2D-ACAR spectra of $Sr_2RuO_4$ are measured for 10 inclination angles on the projection of [001] direction from $0^\circ$ to $45^\circ$ as a step of $5^\circ$. Figure 4.5.2 shows the 2D-ACAR spectra of $Sr_2RuO_4$ for two different inclinations of the [001] projection direction at $0^o$ and at $45^o$ as (a) isometric view and (b) contour map. The angles above the spectra represent the inclination angle. The spectra show the d-like character due to Ru d-like state.

The full three-dimensional momentum density $\rho(P)$ has been obtained using the reconstruction technique based on Fourier transformation. Figures 4.5.3 represent $\rho(P)$ in (001), (100), (110) and (111) planes as contour map. The represented spectra show the d-character due to the existence of Ru ($4d^7$ 5s). From another point of view, the nearest neighbor reciprocal lattice point, $G_{111}$ in $\Delta$, $\sum$ and $\Delta_Z$ directions are at 6.2 mrad, 6.2 mrad and 2 mrad respectively. Accordingly, the Fermi surface of $Sr_2RuO_4$ expected to be affected by the strong signal of d- like state which occur in the higher Brillouin zones. Figure 4.5.4a compare the measured curves for many different cross sections. The spectra in this figure are normalized, and lines passing through $\Gamma$ , X and Z points and in the higher Brilloiun zones are considered. Anisotropies are quite evident by inspecting the spectra, i.e., by comparing $\Gamma$-X and $\Gamma$-Z directions. The anisotropies in a form of differences from $\Gamma$X minus $\Gamma$Z are considered in Fig. 4.5.4b. In this way isotropic contributions are subtracted and the Fermi surface features are enhanced. It is worth to mention that the normalization of the spectra shows a maximum at $\Gamma$ point, this leads to that $\Gamma$ point always have value of zero. A rapid variation is shown in 2 mrad. This shows the electron surface around $\Gamma$-Z direction. The reciprocal lattice points are shown around 4 and 8 mrad as breaks. The same feature as a rapid variation is noted in small momentum. At the first reciprocal lattice point (around 6.2 mrad) the breaks is observe. The second reciprocal lattice point is shown at around 12.5 mrad. In conclusion, Figure 4.5.4 shows Fermi surface signatures in the spectra as hole surface around X point and electron surface in $\Gamma$-Z direction.

In view of Fermi surface, Fig 4.5.5 represents the contours of the reduced zone momentum density n(k) (using LCW method) along c-direction. The schematic Brillouin zone of the tetragonal structure is represented in the same figure. Figure denoted as LCW1 shows a hole surface at X point and electron surface at Γ point. The formation of the electron surface is attributed to the fact that the hole is predominantly situated in the dε(xy)-Pπ band because of the antiponding Ru(4d) dε(xy)- O(2P) pπ on Γ point [4.5.7]. Going up to Fig. LCW2, the center of the plane in the electron surface still observed. That is attributed to the existence of the hole in the antiponding state vertical to $RuO_6$. Figure LCW3 represents the cross section along P point. This figure also shows an electron surface along $\Delta_Z$-direction. Figure LCW5 represents (001) plane through Z point. It shows an electron surface around Z point. From this figure it is clearly obvious that there are only three kinds of Fermi surface sheets in $Sr_2RuO_4$. Two electron surfaces are running along Γ-Z axis, and one hole surface around X point.

Furthermore, $Sr_2RuO_4$ undergoes phase transition. This energetically favorable phase transition lead to shift in the ionic distribution of the positive charges. Therefore, the size of the Brillouin zone changes to be occupied by the entire Fermi surface. In order to examine this phenomena in $Sr_2RuO_4$ , we reduce the electron density in wave vector space n(k) to cover the half of the calculated lattice parameter of its Brillouin zone. Then the electron sheets suppose to nest in the hole sheets. Figure 4.5.6 show n(k) normal to c-direction passing through Γ point for $Sr_2RuO_4$ (a) with real lattice parameter and (b) with half of the lattice parameters. This figure shows the Fermi surface nesting effect as flatness in the spectra.

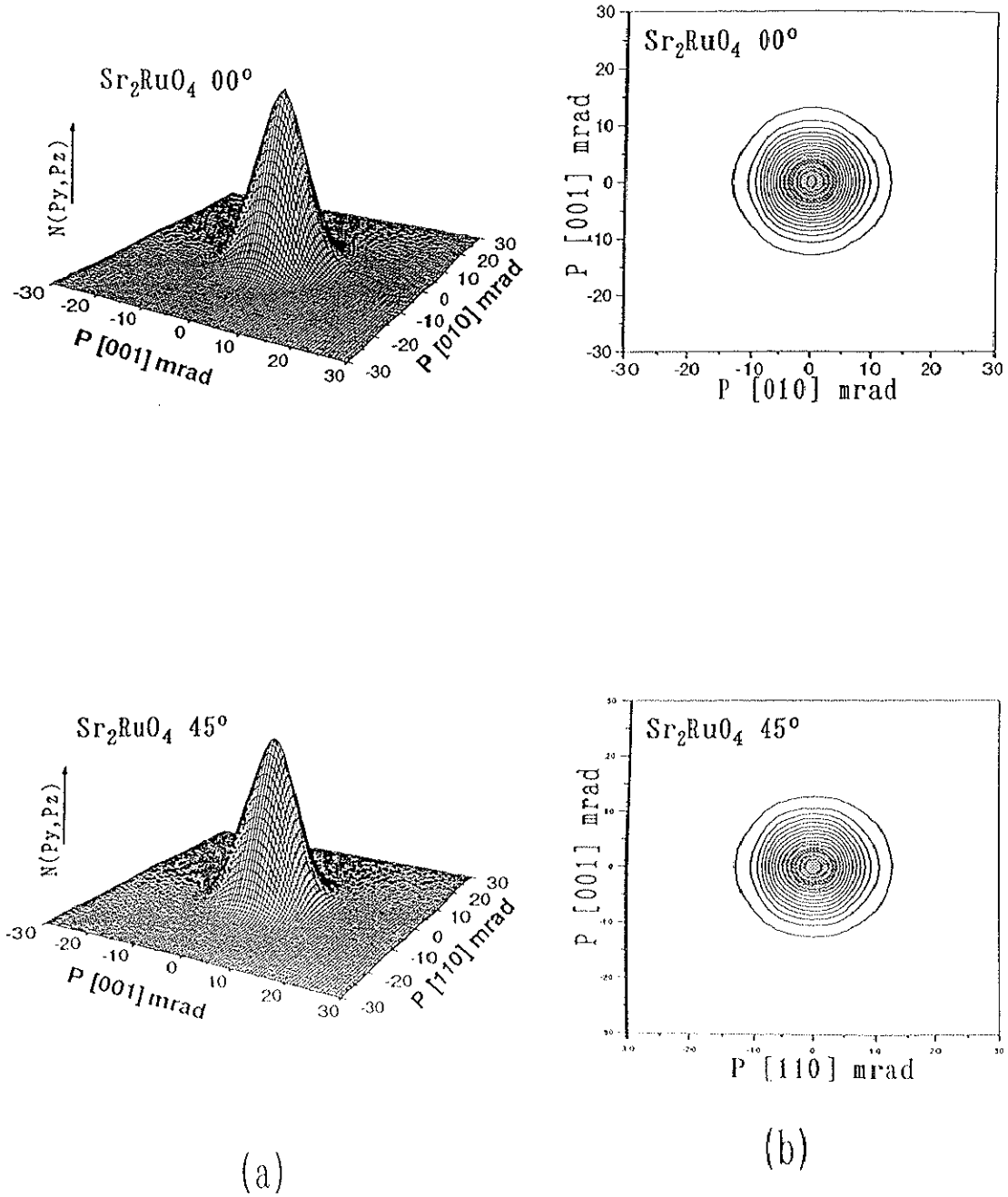


Figure 4.5.2 the 2D-ACAR spectra of $Sr_2RuO_4$ in two extreme angles 0° and 45°. The spectra represented as contour map.

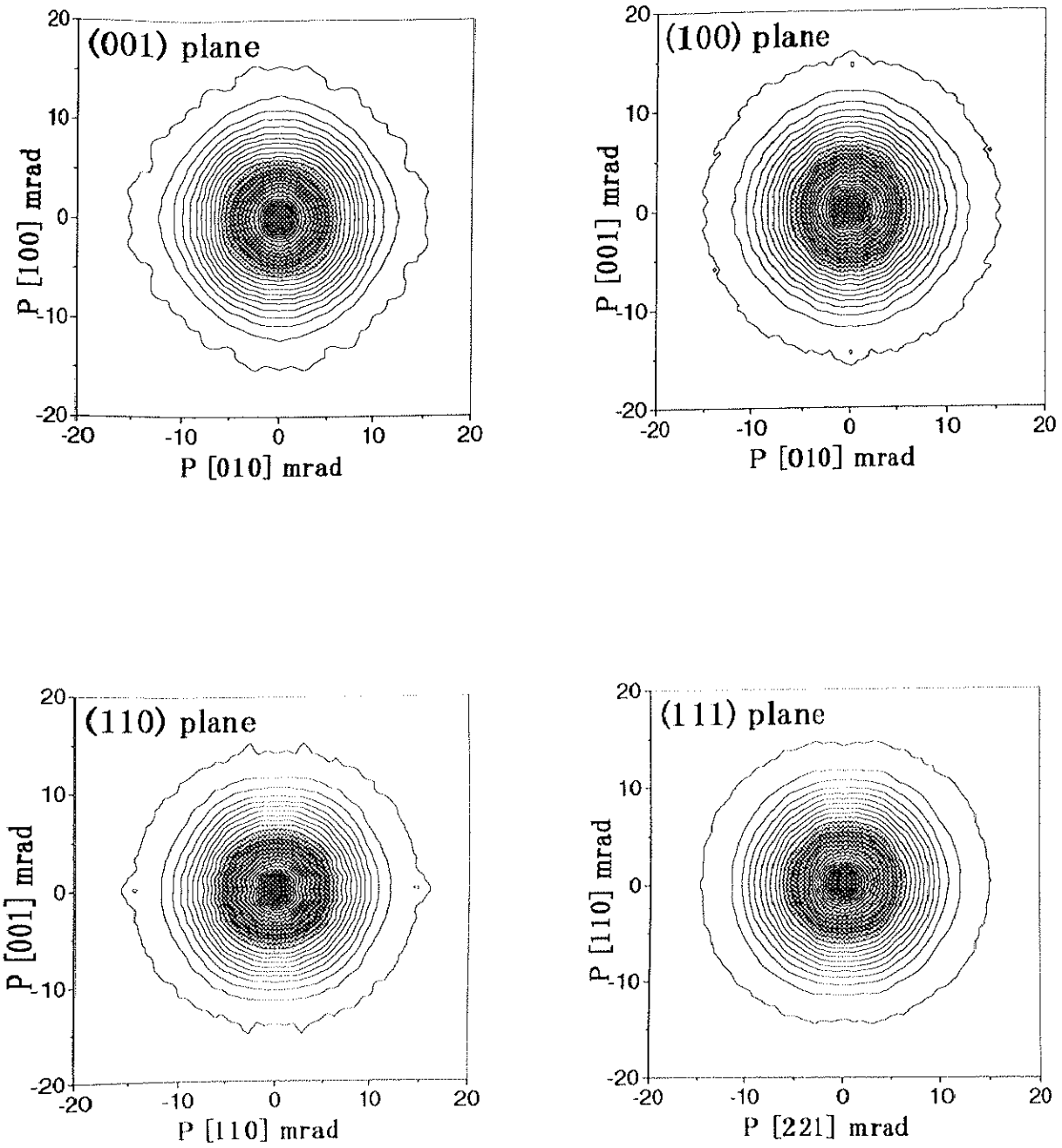


Figure 4.5.3 the three dimensional electron momentum density ρ(P) of $Sr_2RuO_4$ in (001), (100),(110) and (111)as a countour map.

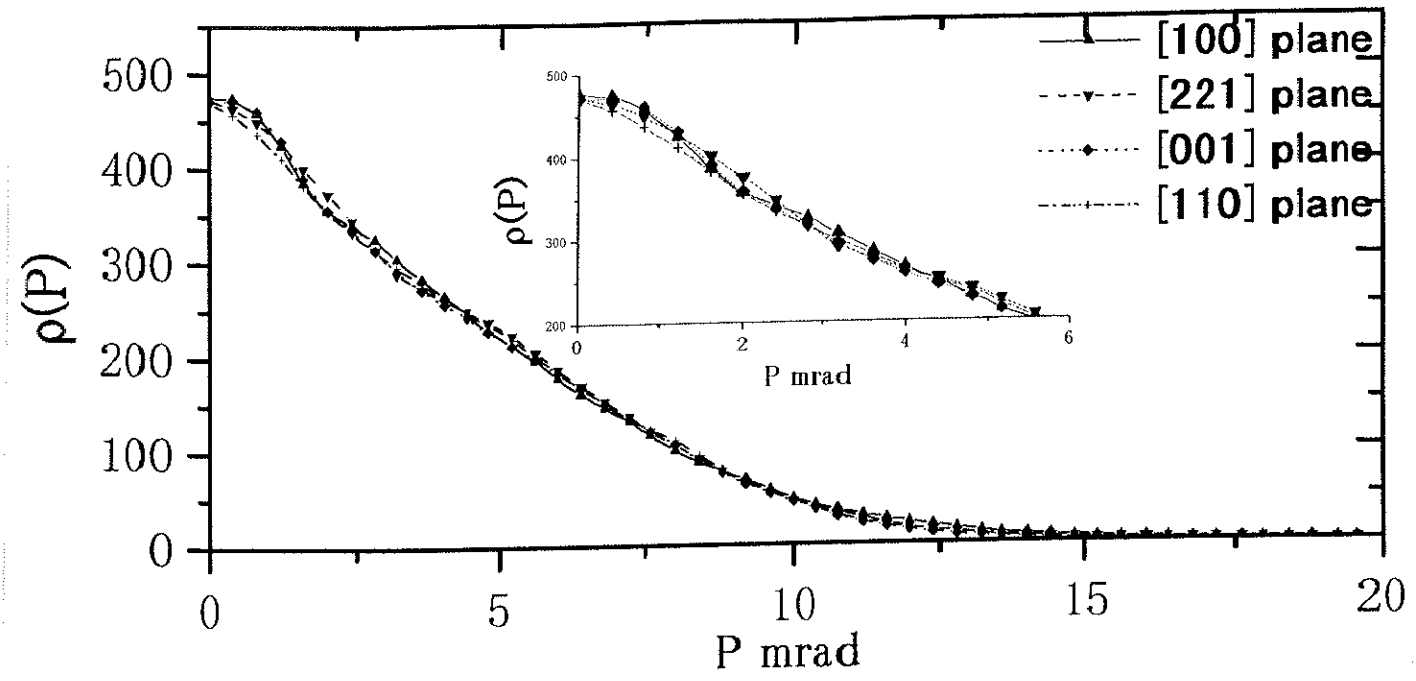


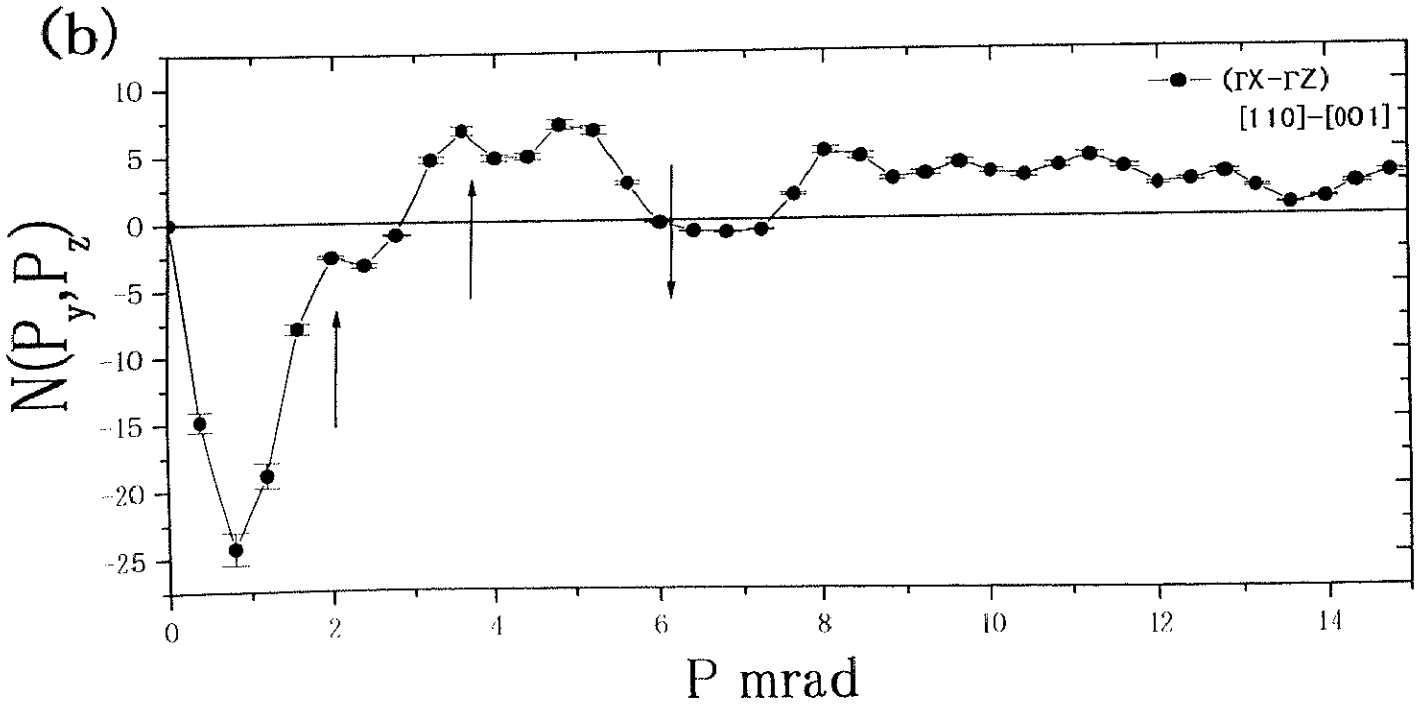


Figure 4.5.4 the electron density in one dimension
(a) shows (100), (221), (001) and (110) directions,
(b) the anisotropy due to subtraction of the [110]direction minus [001] direction,

# $Sr_2RuO_4$

LCW1

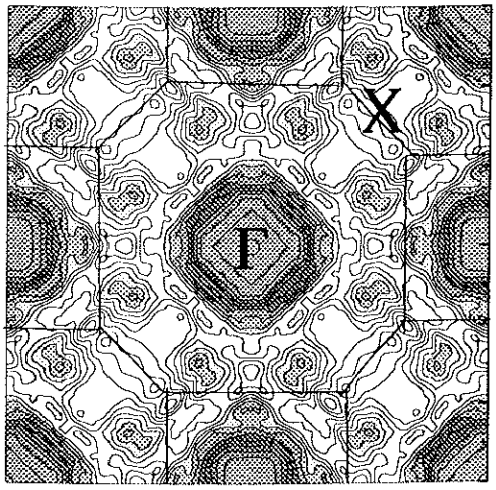


LCW2

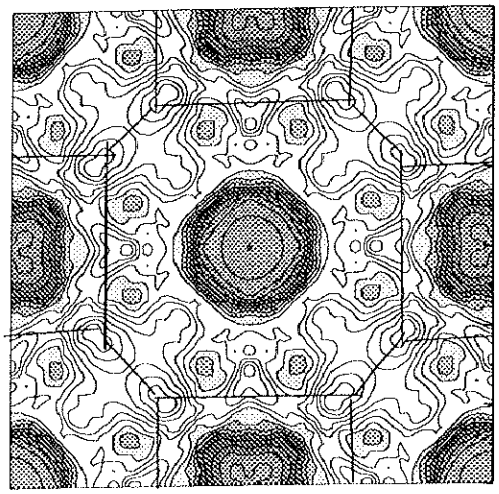

LCW3

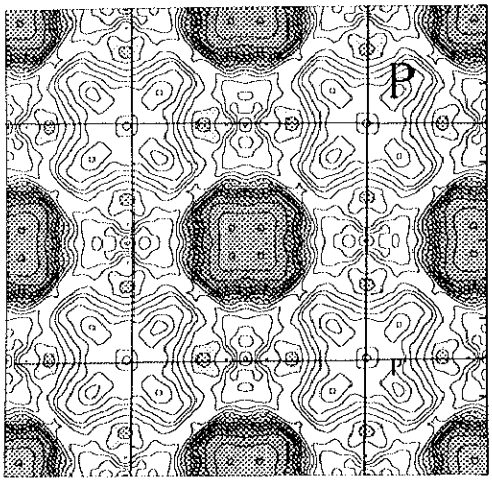


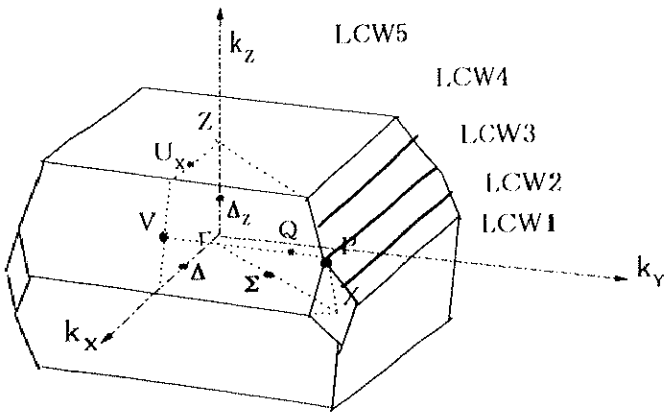


LCW5

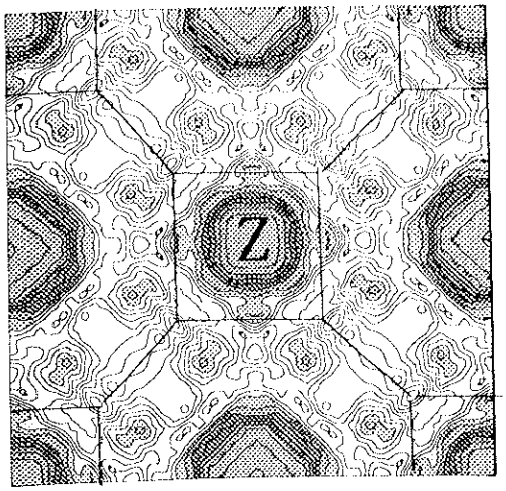


LCW4

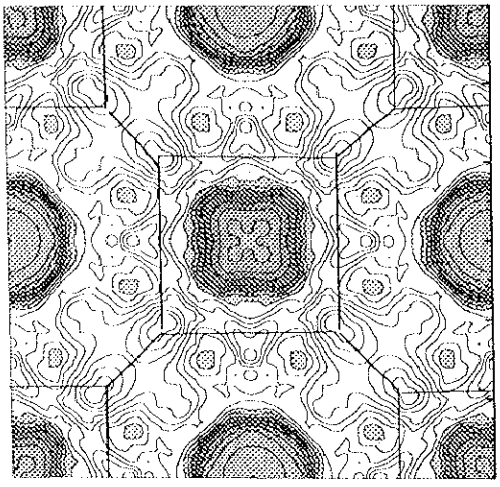

Figure 4.5.5 The contours of the Fermi surface cross sections for $Sr_2RuO_4$, normal to C-direction. The middle right figure shows a schematic representation of the body centered tetragonal BCT structure.

The normalization of the electron density in the wave vector space n(k)% is calculated to see the band number of the above mentioned sheets. Figure 4.5.7 represents the reduced zone momentum density n(k) of $Sr_2RuO_4$ along various symmetric lines. The sharp lines show the band structure using the LDA method [4.5.7]. The thickness of the bands are estimated by the statistical analysis using the least square method (SALS). Table 4.5.1 shows the estimated values of the bands using least square method. The dimensions of Fermi sheets from LDA method are used as input parameters. This figure shows that the interacted bands with Fermi surface are only three bands. They are two electron surfaces are running along Γ-Z axis at 2nd and 3rd bands, and a hole surface around X point at 1st band. In conclusion, the present experimental results show good agreement with the band structure calculations obtained from LDA to density fractional theory [4.5.7].

| | $Sr_2RuO_4$ LDA |
|---|---|
| 1st band $n_1$ | 100.2±1.4 |
| 2nd band $n_2$ | 102.1±1.5 |
| 3rd band $n_3$ | 103.3±1.2 |

Table 4.5.1 the obtained fitting parameters using least square-fitting program for $Sr_2RuO_4$. LDA represents the used input dimensions are from the bands from LDA methods, respectively. The values of the bands are represented with its uncertainty of calculation.

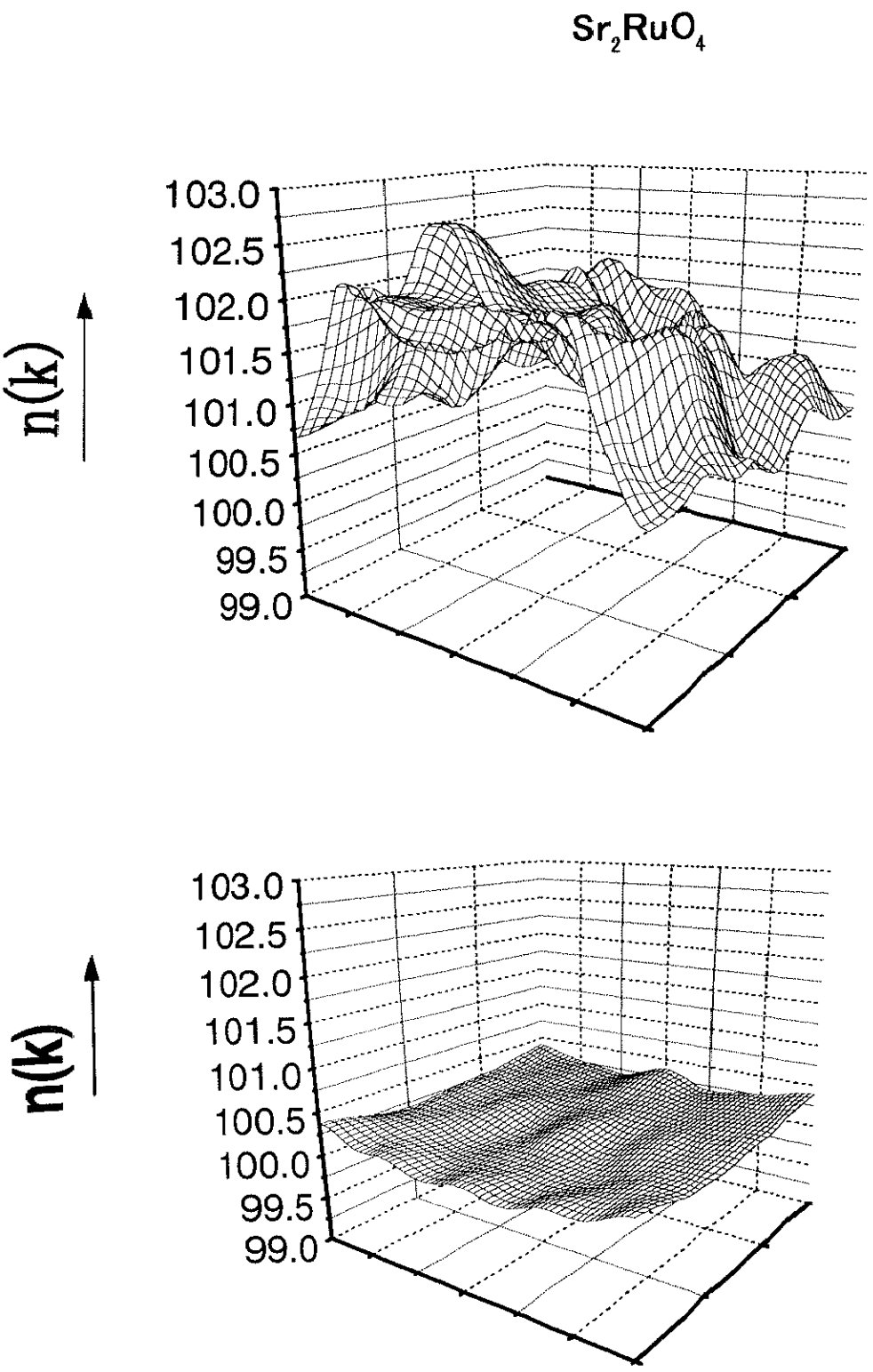


Figure 4.5.6 show n(k) normal to c-direction passing through Γ point for $Sr_2RuO_4$ (a) with real lattice parameter and (b) with half of the lattice parameters

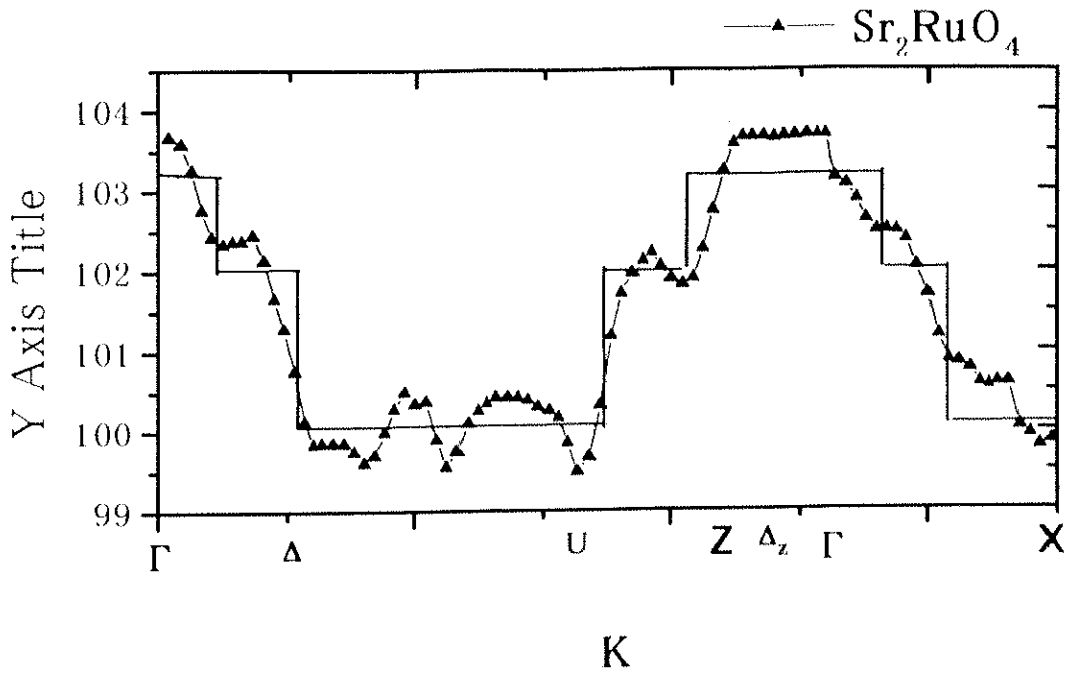


**Figure 4.5.7 the normalized electron density in the wave vector space n(k)% for $Sr_2RuO_4$. The sharp lines show the results of the band structure calculation using the LDA method.**

## IV.6 The layered dichalcogenides of group VB $NbSe_2$

The layered dichalcogenides of group IVB, VB and VIB transition metals have been extensively studied theoretically [4.6.1-4.6.3] and experimentally [4.6.4,4.6.5]. 2H-$NbSe_2$ has received less attention than the others, because it is difficult to make

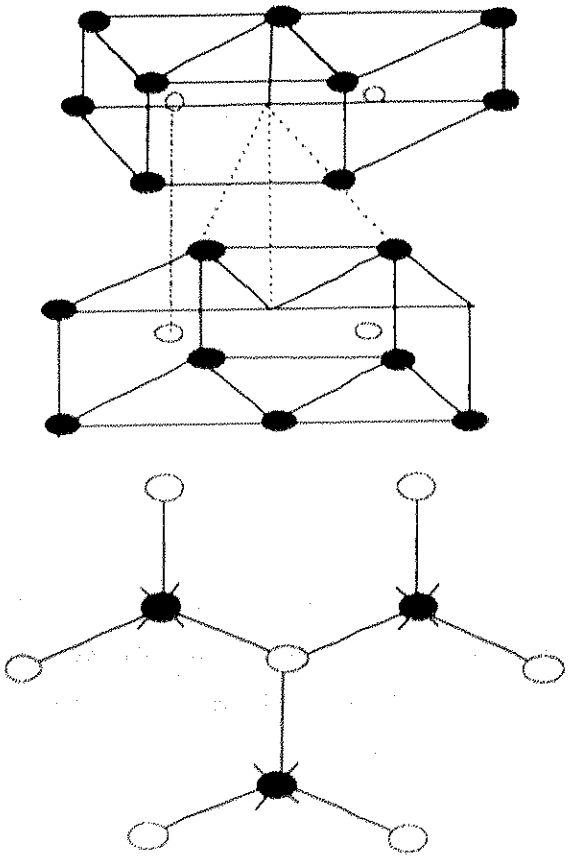

Figure 4.6.1 (a) schematic crystal structure of $NbS_2$ and (b) 2H structure; open circles represent the metal atom; full circles represents the chalcogen atoms in the plane above; and crosses represents the chalcogen atoms in the plane below.

good specimen. 2H- $NbSe_2$ forms layer compounds in which a layer of metal atoms is sandwiched between layers of chalcogens, with relatively weak Van der Waals forces. Figure 4.6.1 shows a schematic representation of 2H-$NbSe_2$-bond structure, it shows that each metal atom coordinates by six chalcogens in trigonal prismatic arrangements of covalent bonds [4.6.6].

The electronic structure of this compound consists of six broad bonds of bonding and anti-bonding orbital from the metal and chalcogen valence orbital, with three non-bonding bonds coming mainly from the metal d orbital in between [4.6.7]. This compound is considered to be conductor because of the extra electron, over the bonded four electrons (in group VB), which goes into the non-bonding bond. The band calculation [4.6.8] investigated that Fermi surface of $NbSe_2$ consists of two kinds of cylindrical hole surfaces. One is an open cylindrical hole surface with axis along ΓA and the other is with axis along KH. The dH-vA measurements effect [4.6.9] shows that the Fermi surface of 2H- $NbSe_2$ was a small shape of a flat ellipsoid centered at Γ point, which resembles pancake. Ramasamy et al [4.6.5] have performed the positron annihilation measurements in $NbSe_2$ and concluded that its Fermi surface has a two dimensional nature. The main interest of this compound is that it shows phase transition and it undergoes charge density wave (CDW) transition below 32K [4.6.7]. Also it changes to super-conducting state at 7.2K. The electronic structure of the above mentioned non-bonding electron plays an important rule in the CDW phase transition [4.6.10]. DiSalvo et al [4.6.2] have mentioned that the CDW which screens the periodic lattice distortion has been emphasized, rather than the atomic displacements themselves. From another point of view, Inglesfield [4.6.6] has emphasized the displacements, the electrons responding to set up incipient chemical bonds between the metal atoms.

In the present work 2D-ACAR spectra of 2H-$NbSe_2$ have been measured through 256 detectors system. Figure 4.6.2 shows the isometric view of the 2D-ACAR spectra of 2H- $NbSe_2$. The deviation angles from the projection of [0001] direction are written above the spectra. Figures 4.6.3a and b represent the electron momentum density ρ(P) in ΓMK, ALM and AHK planes as an isometric view and a contour map respectively. This Figures show some anisotropy in the lower part of the spectra which attributed to the high momentum components (HMC's).

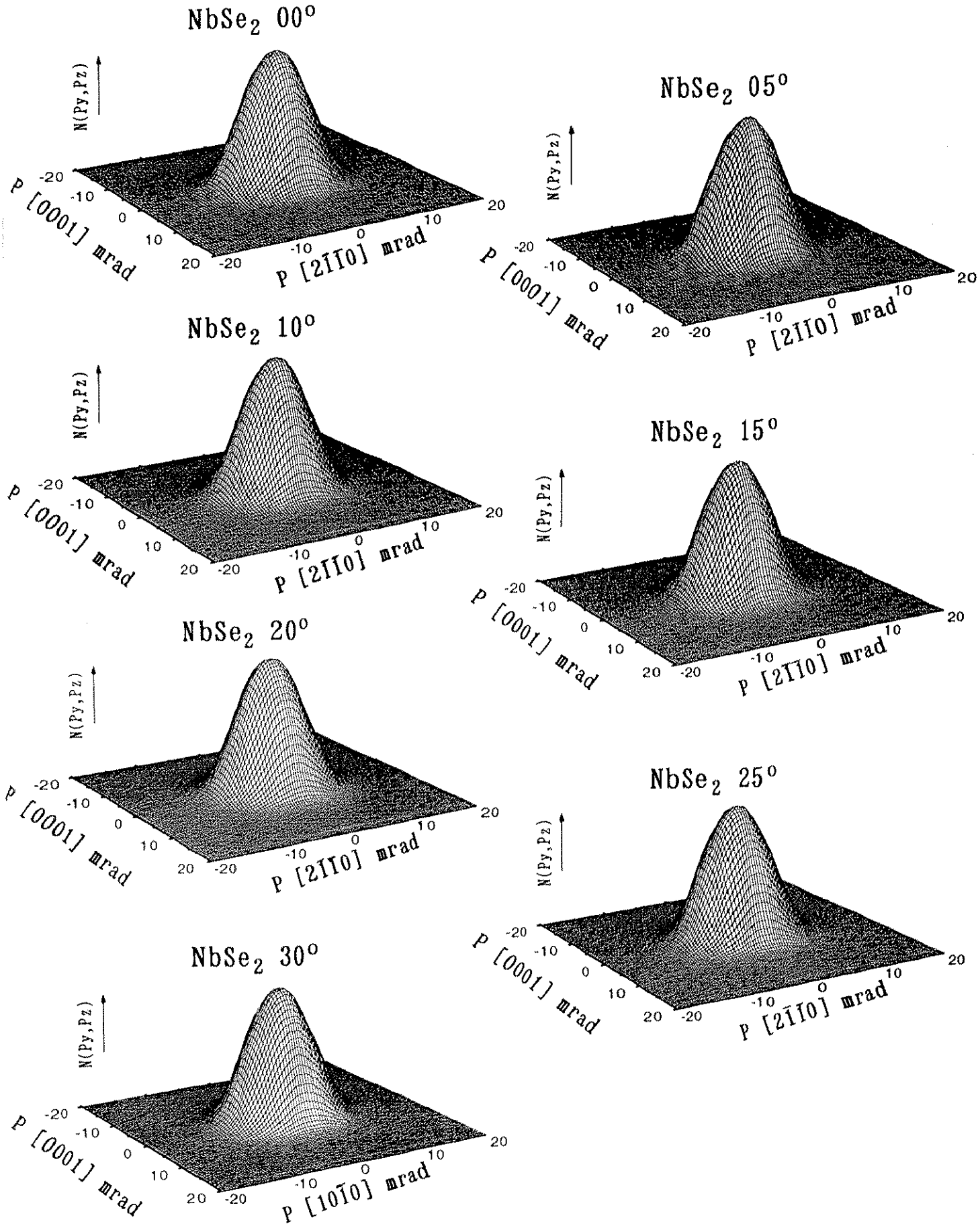


Figure 4.6.2 the 2D-ACAR spctra of $NbSe_2$ in seven inclinations on the [0001] projection direction

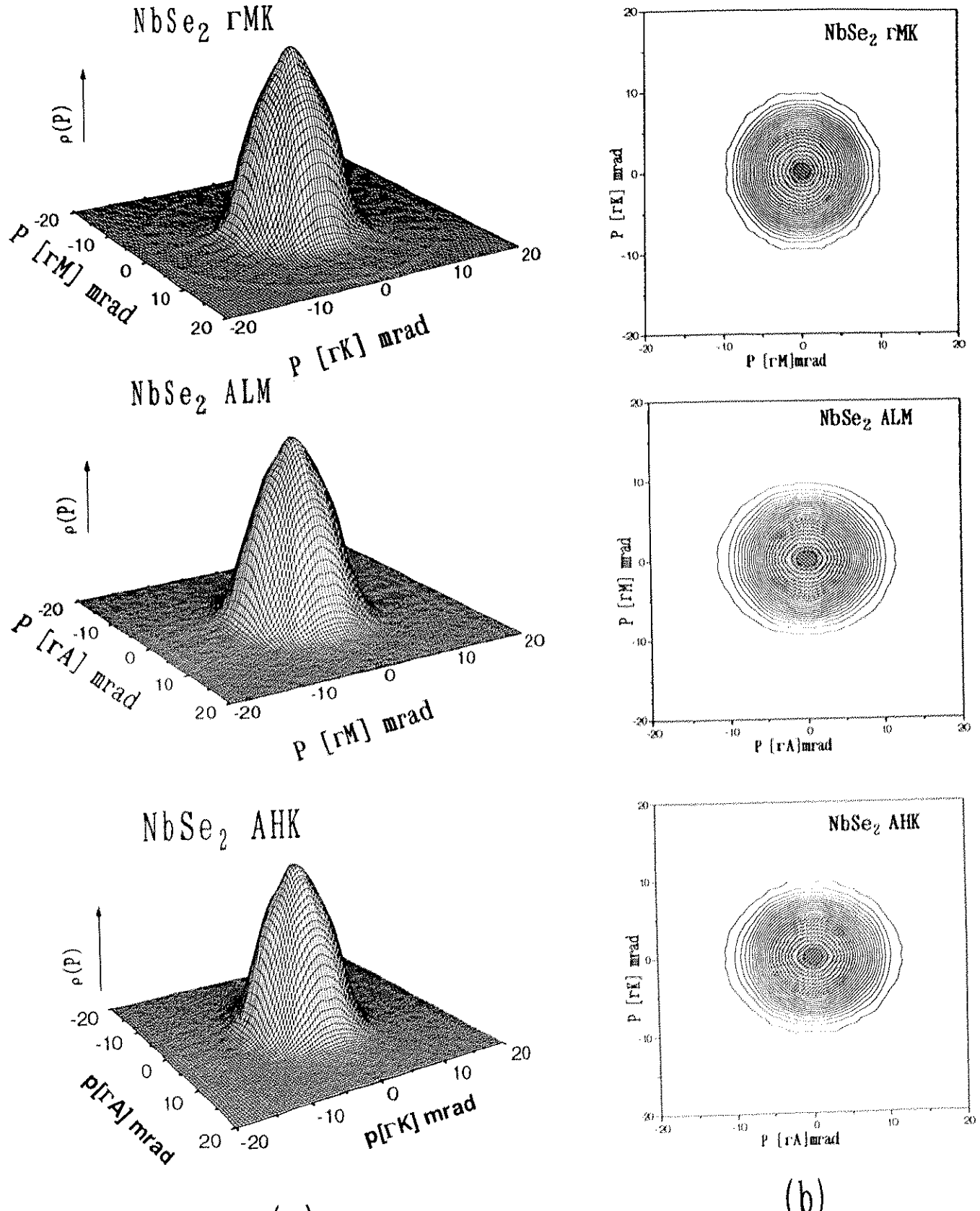


Figure 4.6.3 the electron density in the momentum space $\rho(P)$ for $NbSe_2$ in ΓMK, ALM and AHK planes, respectively.

**The reciprocal lattice points $G_{HI}$ are $P_{\Gamma M}$= 7 mrad, $P_{\Gamma K}$= 8 mrad and $P_{\Gamma A}$= 2 mrad. In Nb atom, which is tightly bounded electron (d-electron), the Fermi surface occurs in the higher Brillouin zones because of the strong signal of d-like.**

**The electron density in the wave vector space n(k) has been obtained using LCW folding procedure. Figure 4.6.4 shows the Fermi surface in different planes of symmetry as (a) the present results and (b) Fermi surface along different symmetry planes using the KKR method [4.6.3]. The hole surface which is running along ΓA axis is observed in the two figures. While the present results contradicts that obtained from Ref. [4.6.3] in the absence of the cylindrical hole surface along KH.**

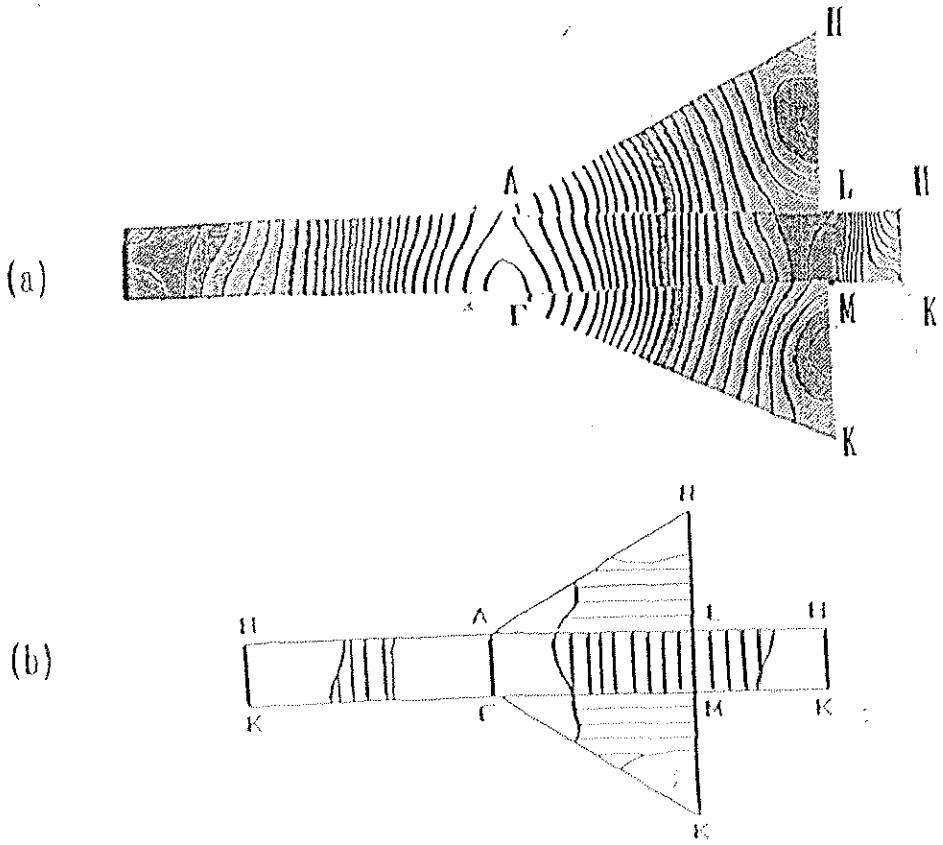


Figure 4.6.4 the Fermi surface of $NbSe_2$ along different plane of symmetry, (b) the fermi surface obtained using KKR method [4.6.3].

Figure 4.6.5 shows the normalized value of n(k)% along the principal symmetry lines. This corresponds to the assumption that the wave function of the positron is uniform in the whole region. The sharp lines represents the band structure calculation obtained from Ref.[4.6.8]. This figure shows clearly that the hole surface around Γ-A axis is equivalent to that obtained by the theory while K and H points contradict that obtained from it. The dimensions of the Fermi surface are obtained using $|\nabla n(k)|_{Max}$. Table 4.6.1 declares the dimensions of the cylindrical hole surface with the Γ-A axis, From the present results and from the theoretical one obtained by Matthesis[4.6.8]. It can be noted that the experimental value of the hole surface is larger than that predicted by the theory.

| Fermi surface (direction) | 2D-ACAR results | Ref.[4.6.8] |
|---|---|---|
| ΓM | 0.27±0.02 | 0.247 |
| ΓK | 0.26±0.02 | 0.188 |
| AL | 0.27±0.02 | 0.255 |
| AH | 0.26±0.02 | 0.184 |

Table 4.6.1 Fermi surface dimensions of the open cylindrical hole surface along ΓA axis in a.u.. The theoretical values are that obtained from reference[4.6.8]

This differences is attributed to the non uniformity of positron wave function or the electron positron calculations, and because of the absence of the hole surface along KH direction which make the theoretical value smaller than the experimental one.

As mentioned above that 2H-$NbSe_2$ undergoes phase transition. This energetically favorable phase transition lead to shift in the ionic distribution of the positive charges. Therefore the size of the Brillouin zone changes to be occupied by the entire Fermi surface, and the Fermi surface nesting effect appears to be flat. In order to examine the nesting effect, we reduced the momentum space density n (k) to be contained in the half of the actual lattice parameter of the Brillouin zone.

**Then the constructed Brillouin zone, due to the phase transition, will be occupied by the Fermi surface of the compound. Figure 4.6.6 shows the isometric view of reduced n(k) using (a) the actual lattice parameters and (b) the half of the lattice parameters along c-direction. This figure shows clearly the nearly perfect Fermi surface nesting effect as flatness in the spectra.**

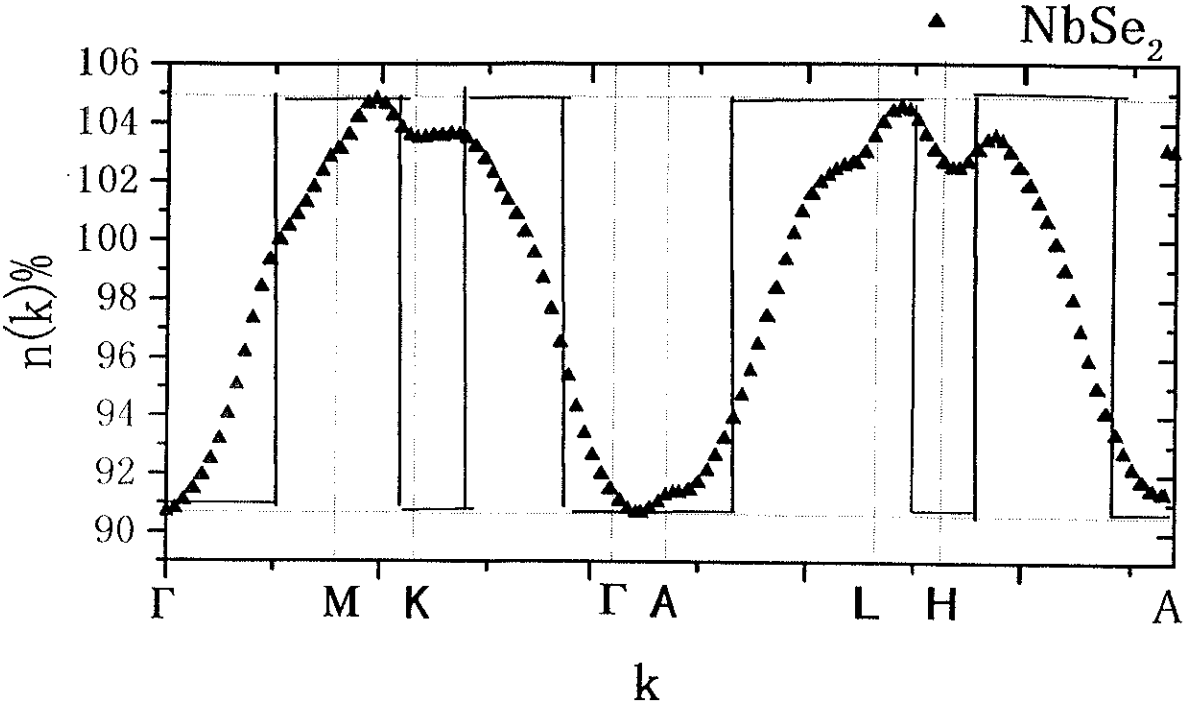


Figure 4.6.5 the normalized electron density in the wave vector space n(k)% for $NbSe_2$. The sharp lines show the results of the band structure calculation using the APW method.

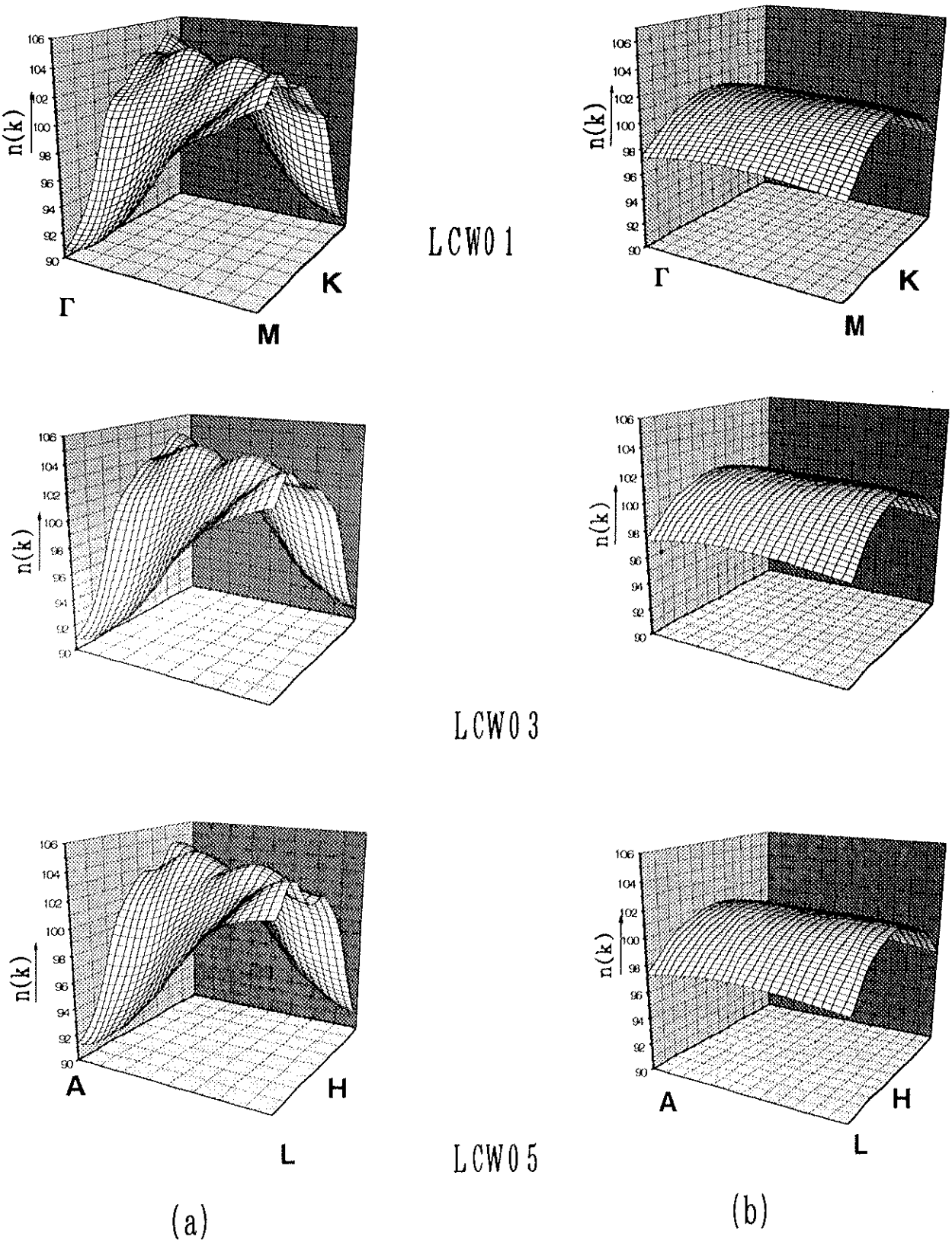


Figure 4.6.6 shows the isometric view of reduced n(k) using (a) the real lattice parameters and (b) the half of the lattice parameters along c-direction.

# Conclusions

The measurements of 2D-ACAR spectra were performed, using two experimental set ups, for the following materials; the divalent HCP metal (Mg, Zn and Cd), the HCP structure metals of group IIIA (Sc and Y), the HCP structure metals of group VIA (Ti, Zr and Hf), the FCC structure metal of group VIII (Rh and Ir), the non cuprate proviskite superconductor $Sr_2RuO_4$; and the layered dichalcoginide of group VB $NbSe_2$. From the obtained results $\rho(p)$ was reconstructed using the reconstruction technique based on Fourier transformation. Then, the electron momentum density, of the metals under investigation, in the main cross sections were obtained and discussed. Furthermore, Fermi surface topology was constructed in reduced zone scheme using LCW folding procedure.

The reconstructed $\rho(P)$ of Mg, Zn and Cd shows distortions on the upper part of $\rho(P)$ spectra, and it was attributed to the Brillouin zone interaction. $\rho(P)$ of those metals shows some important features; the contribution due to the interaction of the positron with the core state; the contributions of the high momentum components (HMC's); and distortions in the upper parts of the spectra due to Kahana-like enhancement factor. It was observed that the main contribution to the Fermi surface comes from $G_{00}$, and the first Brillouin zone is the strongest and the Fermi surface in the higher zone is weak. In terms of the enhancement effect, it is obvious that the gradient of the enhancement increases as the atomic number of the used element increases. This shows that Mg is very closed to the free electron model, while the enhanced contribution increases as going from Zn to Cd. In view of Fermi radius of those metals. It shows a small deviation from that obtained by the free electron model for Mg. Other wise, this deviation increases as the atomic number of the used metals increases, i.e., Zn then Cd. The present results have been compared with the Fermi surface of the free electron model. Fermi surface of Mg is found to be consisting of, $2^{nd}$ band hole surface (monster), $3^{rd}$ band electron surface centered on $\Gamma$ (lens), $3^{rd}$ band electron surface centered on L point (butterfly), and $4^{th}$ band electron surface centered on L point (cigar). The $1^{st}$ band hole surface centered on H point (cap) and the electron surface centered on K point (needles) are not seen in the present results of Mg. Fermi surface of Zn is consisting of, $1^{st}$ band hole surface at H point (cap), $2^{nd}$ band hole surface

(monster), 3rd band electron surface at Γ point (lens), 3rd band electron at L point (butterfly), and 4th band electron surface at L point (cigar). Fermi surface of Cd is consisting of; 1st band hole crossed to Fermi level near the point H (cap), 2nd band hole (monster), 3rd band zone electron centered on Γ point (lens), 3rd band electron surface centered on L point (butterfly) and 4th band electron surface at L point (cigar). the 3rd band electron surface centered at K point (needles) doesn't observe neither in the present experiment nor in the free electron model.

The measured 2D-ACAR spectra of Sc and Y show some breaks in their upper part. They are attributed to the fact that they contain 3 valence electrons. The momentum density displays a discontinuity at the Fermi momentum $k_F$ in the first Brillouin zone and at momenta $k_F \pm G$ in the higher zones. However, these breaks are superimposed on the continuous contribution from full valence band. The high momentum components are also observed in the spectra of Sc and Y, which are attributed to Umklapp process. Concerning Fermi radii of Sc and Y, they show deviation from the free electron Fermi radius. As a result, these metals are deviated from the free electron model. In terms of Fermi surface, we concluded that the present results of Fermi surface of Sc consists of Two categories; the first is, hole surfaces at Γ and L points in 4th band and a hole surface at A point in 2nd band. The second is, electron surfaces at M and K points in 4th band and electron surface around H point in 3rd band. This result agrees to the band structure calculation using the APW method, except at Γ point. The present results of the Fermi surface of Y consists of two categories; the first is, hole surfaces at Γ and A points in 2nd band and the hole surface at L point in 3rd band. The second is, electron surfaces at M and K points in 4th band and electron surface around H point in 4th band. This result shows agreement with that obtained from the band structure calculation using the APW method.

2D-ACAR measurements have been performed for Ti, Zr and Hf. The spectra show breaks in their upper parts. They are attributed to the same reason as for Sc and Y. Since Ti, Zr and Hf contain 4 valence electrons, the momentum density displays a discontinuity at the Fermi momentum $k_F$ in the first Brillouin zone and at momenta $k_F \pm G$ in higher zones. The HMC's due to the Umklapp process were

observed in the spectra. As a result, It was found that Fermi surface of Ti , Zr and Hf are found to be affected by a strong signal d-like character which occurs in their higher Brillouin zones. As a comparison with the free electron Fermi radius, the present results show large deviation from it. Therefore, Fermi surfaces of them are considered to be deviated strongly from the free electron model. The observed Fermi surface in the present results have the same features as obtained from the band structure calculations using the APW method for Ti, Zr and Hf and as observed using the RAPW method for Hf. It has the same features for Ti and Zr, namely, the hole surfaces at 3$^{rd}$ and 4$^{th}$ bands along the Γ-A axis and the electron surfaces at 5$^{th}$ and 6$^{th}$ bands around H point. The electron surface at 5$^{th}$ and 6$^{th}$ bands, of both Zr and Hf, are overlapped and they need higher experimental resolution to distinguish between them. This attributes to the experimental resolution in which if the Fermi surface sheet or if there are two sheets have dimensions comparable to the experimental resolution, then the determination of their dimensions became very difficult.

The 2D-ACAR spectra have been obtained for Rh and Ir. From the obtained data the full three dimensional electron density in the momentum space are determined. The background in Ir spectra is observed higher than that of Rh spectra. This is attributed to its high absorption of γ-rays. Consequently, the obtained γ-rays from the annihilation process undergoes attenuation with small angles and collected as accidental coincidence events. In view of the HMC's, the nearest neighbor reciprocal lattice points $G_{111}$ is obtained and it was found that for Rh is at (6.1 mrad) and for Ir is at (6.3 mrad). Taking into consideration the comparison of Fermi radii of Rh and Ir with the free electron Fermi radius. They show large deviation from the free electron ones. Consequently, departing from the free electron Fermi surface is considered. The Fermi surface of Rh was found to consist of two large closed electron surfaces at Γ point in the 4$^{th}$ and 5$^{th}$ bands, two closed hole surfaces at X point in the 2$^{nd}$ and 3$^{rd}$ bands and one small closed hole surface at L point in the 3$^{rd}$ band. For Ir, Fermi surface consists of two large electron surfaces around Γ point in the 4$^{th}$ and 5$^{th}$ bands, and two closed hole surfaces around X point in the 2$^{nd}$ and 3$^{rd}$ bands. The difference between Rh and

Ir is that the small pocket of holes at L point has vanished in Fermi surface of Ir. This was attributed to the difference between Rh and Ir in their electronic structure. The Fermi surfaces of Rh and Ir show good agreement with that obtained using the RAPW method.

The non-cuprate layered perovskite compound $Sr_2RuO_4$ has been measure through the 2D-ACAR experimental set up. Fermi surface features are observed from the anisotropy on the spectra. Furthermore, the present results of Fermi surface show good agreement with that obtained by the band structure calculation using the LDA method. It consists of 1$^{st}$ band hole surface around X point and 2$^{nd}$ and 3$^{rd}$ band electron surfaces which are running along Γ- Z direction. Generally, good agreement is obtained with the LDA method. Fermi surface nesting effect is observed in $Sr_2RuO_4$ as a flatness in n(k) spectra.

The layered dichalcogenides of group VB 2H-$NbSe_2$ forms layer compounds in which a layer of metal atom is sandwiched between layers of chalcogens with relatively weak Van der Waals forces. ρ(P) was reconstructed from the 2D-ACAR data of 2H-$NbSe_2$. Fermi surface of 2H-$NbSe_2$ was obtained and it consists of, a cylindrical hole surface running along ΓA axis. Its dimensions were calculated and they were found to be larger than the theoretically calculated. The difference of the Fermi surface sheets' dimensions was attributed to the non uniformity of positron wave function or the electron positron calculations, and because of the absence of the hole surface along KH direction which makes the theoretical values smaller than the experimental ones. Using the half of the lattice parameters, Fermi surface nesting effect is observed in $Sr_2RuO_4$ as a flatness in n(k) spectra.

In conclusion the present results of Mg, Zn and Cd showed good agreement with the free electron model. The other elements in the present study are departed from it. The Fermi surfaces of Sc, Y, Ti and Zr show agreement with the APW method. On the other hand the Fermi surface of Hf, Rh and Ir show good agreement with the RAPW method.

# References

[1.1.1] For brief reviews of the early history of positron physics, see papers by S. DeBeneditti and A. T. Stewart, in " positron annihilation, edited by A. Stewart and L.O. Roellig (New York, 1967)"

[1.1.2] R. Beringer and C.G. Montgomery, Phys. Rev., 61, 222 (1942)

[1.1.3] S. Berko and J. S. Plaskett, Phys. Rev., 112, 1877 (1958)

[1.1.4] S. Berko, M. Haghgooie and J. J. Mader, Phys. Lett. A, 63, 335 (1977)

[1.1.5] A. A. Manual, S. Samoilov, O. Fischer and M. Peter, Helv. Phys. Acta, 52, 255 (1979).

[1.1.6] R. N. West, J. Mayers and P. A. Walters, J. Phys. E, 14, 478 (1981).

[1.1.7] J. Friedel in " The physics of metals" edited by J. M. Ziman (Combrige university, Combrige (1969)).

[1.2.1] H. Jones, "Brillouin zone and electronic states in crystals", North-Holland , Amsterdam (1962).

[1.2.2] J. M. Ziman, "The T matrix, the K matrix, d bands and l-dependent Psedu-potentials in the theory of metals, " Pro. Phys. Soc. (London), 86, 337 (1965).

[1.2.3] J. Callaway, "Energy band theory", Academic press, New York (1964).

[1.2.4] J. C. Slater "Quantum theory of molecules and solids" Vol. 2, McGraw Hill, New York (1965).

[1.2.5] W. A. Harrison "Psedu-potentials in the theory of metals" Benjamin, New York (1966).

[1.2.6] T. L. Loucks " Augmented plane wave method", W. A. Banjamin, Inc. New York, Amsterdam (1967).

[1.2.7] D. A. Papaconstantopoulos " hand book of the band structure of elemental solids, Plenum Press, New York (1986).

[1.2.8] J. H. Terrell "the Fermi surface of Beryllium" Phys. Letters, 8,149 (1964).

[2.1.1] P. E. Mijnarends and A. Bansil, international school of physics <<ENRICO FERMI>> positron spetroscopy of solids (1995).

[2.2.1] Chang Lee: Z. Expt. theor.,33, 356 (1957); translation in soviet Phys. JETP, 6, 281 (1958).

[2.2.2] R. Suzuki and M.Osawa, S. Tanigawa, M. Matsumoto, and N. Shiotani, J. Phys. Soc. Jap, vol. 58, pp. 3251, (1989).

[2.4.1] D. G. Lock, V. H. C. Crisp, and R. N. West, J. Phys, F3, 561 (1973).

[2.5.1] S. Kahana, Phys. Rev. 129, 1622 (1963).

[4.1.1] S.Daniuk, T.Jarlborg, G.K-Sznajd, J.Majsnerowski, and H.Stachowiak, J.Phys.Condens. Matter 1, 8397 (1989)

[4.1.2] W.A.Harrison, Phys. Rev, 126, 2, 497 (1962).

[4.1.3] R.W.Stark, and L.M.Falicov, Phys.Rev.Letters, 19, 14, 795 (1967).

[4.1.4] S.Chatterjee, and P. Sinha, J.Phys.F:mat.Phys.,5,2089 (1975),

[4.1.5] R.Asokamani, K.Lyakutti, R.S.Rao, and V. Devanathan ,J.Phys . F : Mat.Phys,8, 2323 (1979)

[4.1.6] R. W. Stark, Phys.Rev, 162, 589 (1967),

[4.1.7] J.P. Katterson and R.W. Stark, Phys. Rev, 156, 748 (1967).

[4.1.8] J.C. Kimball,R.W. Stark, F.M. Muller, Phys. Rev,162,600 (1967).

[4.1.9] H.Nakashima, T.Kubota, H.Kondo, Y.Murakami, and S.Tanigawa, Phys.Stat. Sol, 170,171 (1992).

[4.1.10] O.L.Steenhut and R.G.Goodrich ,Phys.Rev.B, 1, 12, 4511(1970)

[4.1.11] J.P.Van Dyke, J.W.McClure,and J.F.Doar, Phys. Rev. B, 1,6, 2511 (1969).

[4.1.12] W.A.Reed, and G.F.Bennert, Phys.Rev. 130, 2, 565(1963).

[4.1.13] A.S.Jopson, W.L.Gordon, Phys.Rev. 126,489 (1962)

[4.1.14] Shin-ichi Katsuki,and Mikio tsuji, J.Phys.Soc.Jap.,20,7,1136 (1965).

[4.1.15] R.C.Jones, R.G.Goodrich, L.M.Falicove, Phys.Rev, 174, 672 (1968).

[4.1.16] M.R.Danial, and L.Mackinnon, Pill.Mag,8,837 (1963).

[4.1.17] P.Sinha and S.Chatterjee, J.Phys. F7, 1 (1977).

[4.1.18] J.Trivisonno, and R.W.Stark, J.low,Temp.Phys,32 ,725 (1978).

[4.1.19] D.F.Gibbones and L.M.Falicov, Phli.Mag,.8, 177 (1963).

[4.2.1] M. F. Mott Adv. Phys. 13, 325 (1964).

[4.2.2] Yn. A. Bogod and V. V. Eremenko Phys. status. solidi, 11, K51 (1965).

[4.2.3] R. W. Williams and A.R. Mackintosh Phys. Rev. 168, 3(1967)

[4.2.4] W. A. Harrison Phys. Rev 118, 1190(1960) .

[4.2.5] S. L. Altmann and C. J. Bradley Proc. Phys. Soc. 92, 764(1967) .

[4.2.6] G. S. Fleming and T. L. Loucks Phys. Rev. 173, 685 (1968).

[4.2.7] T. L. Loucks ( Phys. Rev 144, 504 (1966).

[4.2.8] A.S.Abdul Hamid and S.Tanigawa To be published in the Phys status solidi.

[4.3.1] A.S. Abdul Hamid and S. Tanigawa, submitted to J. Phys. condens. Matter

[4.3.2] A.C. Thorsen and A.S. Joseph. Phys. Rev, 131, 2078 (1963)

[4.3.3] S.L.Altmann and C.J. Bradley, Phys. Rev, 135, a1257 (1964)

[4.3.4] L.F. Mattheiss, Phys. Rev. 143, 506 (1966)

[4.3.5] S.L.Altmann and C.J. Bradley, Proc. Phys. Soc., 92, 764 (1967)

[4.3.6] E. H. Hygh and R. M. Welch, Phys. Rev. B 1, 2424 (1970)

[4.3.7] D.A. Papaconstantopoulos, Handbook of the band structure of elemental solids, 1986 Plenum Press, New York, 171.

[4.3.8] T.L. Loucks, Phys. Rev, 159, 544 (1967)

[4.3.9] O.Jepsen, O.K.Andersen and A.R. Machintosh, Phys.Rev.B, 12, 8, 3084 (1975).

[4.4.1] P.T.Coleridge, Phys. Lett., 15, 223 (1965)

[4.4.2] P.T.Coleridge, Proc. R. Soc. A,295, 458 (1966)

[4.4.3] S. Wakoh and J. Yamashita, J. Phys. Soc. Japan, 19, 1342 (1964)

[4.4.4] O.K. Andersen and A.R. Machintosh, Solid. Stat. Commu., 6, 285 (1968)

[4.4.5] J.J. Grodski, A.E.Dixon, Solid. St. Commu., 7. 735 (1969)

[4.4.6] S. Hornfeldt, Solid. Stat. Commu., 8, 673 (1970)

[4.4.7] D.A. Papaconstantopoulos, Handbook of the band structure of elemental solids, 1986 Plenum Press, New York, 171.

[4.5.1] Y. Maeno, H. Hashimoto, K. Yoshida, S. Nishizaki, T. Fujita, J. G. Bednorz and F. Lichtenberg, Nature 372, 532 (1994)

[4.5.2] F. Lichtenberg, A. Catana, A. Mannhart and D. G. Schlom, Appl. Phys. Lett. 60, 1138 (1992)

[4.5.3] David J. Singh, Phys. Rev B, 52, 2, (1995)

[4.5.4] N. Shirakawa, K. Murata, Y. Nishihara, S. Nishizaki, Y. Maeno, T. Fujita, J. G. Bednorz, F. Lichtenberg and N. Hamada J. Phys. Soc. Jpn, 64, 4, 1072 (1995)

[4.5.5] T. Vogt and D. J. Buttrey, Phys. Rev b, 52, 14, R9843 (1995)

[4.5.6] S. Nishizaki, Y Maeno and T Fujita, J. Phys. Soc. Jpn, 65, 6, 1876 (1996)

[4.5.7] T. Oguchi, Phys Rev B, 51, 2, 1385 (1995)

[4.6.1] G. Waxler and A.M. Woolley J.Phys.C solid sttat. Phys. 9, 1185 (1979)

[4.6.2] F. J Di Salvo and T.M.Rice Phys. Today, 32, 32(1979)

[4.6.3] S.P. Hind and P. M. Lee J phys. C; Solid st. Phys., 13m 349(1980)

[4.6.4] A.J. Arko, G.W.Crabtree and Z. Fish; Conf on suppersonductivity in d- and f- bands metal la Jolla, Acadimic press p121(1979).

[4.6.5] S. Ramasamy, T. Nagaran, C.S. Sunandana and G.V. Subba Rao, Physica, 100b, 202(1980)

[4.6.6] J.E.Inglesfield, J.Phys.C: Solid st. Phys. 18, 193(1986)

[4.6.7] J. A. Wilson and A. D Yoffe ,Adv. Phys. 18, 193(1969)

[4.6.8] L. F. Matthesis Phys. Rev. B8 3719(1973)

[4.6.9] J. E. Graebner and M. Robbins Phys. Rev. Lett. 36, 422 (1976).

[4.6.10] J. A. Wilson, F. J Di Salvo and S. Mahajan Adv. Phys. 24, 117(1975).

本学関係